NON-HERMITIAN ASPECTS OF COHERENTLY COUPLED VERTICAL CAVITY LASER ARRAYS

BY

ZIHE GAO

DISSERTATION

Submitted in partial fulfillment of the requirements
for the degree of Doctor of Philosophy in Electrical and Computer Engineering
in the Graduate College of the
University of Illinois at Urbana-Champaign, 2018

Urbana, Illinois

Doctoral Committee:

Professor Kent D. Choquette, Chair
Professor Weng Cho Chew
Professor Lynford L. Goddard
Assistant Professor Kejie Fang

ABSTRACT

Two by one (2 × 1) optically coupled electrically isolated vertical cavity surface emitting laser (VCSEL) arrays have been studied both theoretically and experimentally. Because of the tunable gain/loss profile in the array, the coupled laser system is non-Hermitian in analogy with non-Hermitian quantum mechanics. The experimentally observed optical mode tuning and beam steering are inherently connected to the non-Hermiticity of the system. Theoretical investigation of the mode tuning mechanism is conducted first by coupled mode analysis, and then in a more comprehensive coupled rate equation analysis. The theoretical analysis reveals the unique mode tuning mechanism in coupled VCSEL arrays and is shown to be in excellent agreement with experimental characterization. Experimentally, 2 × 1 optically coupled electrically isolated VCSEL arrays have been designed, fabricated, and characterized. We perform two-dimensional characterizations by varying the two independently controlled injection currents into each array and recording the laser output power, spectra, near-field intensity profile, and far-field intensity profile. Two-dimensional maps of the output optical power, interference visibility, and beam steering angles versus the two injection currents are plotted as concise representations of the mode tuning behavior controlled by the current tuning. Arrays with built-in asymmetry between the two lasers demonstrate that the mode tuning behavior can also be engineered by the degree of asymmetry. The coupling coefficient is extracted from the characterizations. The theoretical and experimental investigations presented in this work reveal the unique mode tuning mechanism in weakly coupled diode laser arrays and will guide the future pursuit of improved functionalities in coupled VCSEL arrays.

To my parents,

Yongfeng Yu and Lianxing Gao

ACKNOWLEDGMENTS

I would first like to thank my advisor, Kent Choquette, for his guidance and friendship throughout my graduate studies, for his insightful discussions regarding and beyond this dissertation project, and for spreading his enthusiasm for science, technology, and running. I am indebted for his constant support.

Thanks to all the members of the Photonic Device Research Group, current and former, who have interacted with me. Many critical aspects of this dissertation project are based on the research of previous group members and the help from current group members. I would like to thank Maj. Matthew T. Johnson and Dr. Dominic F. Siriani for the help that I received early in my research career. Special thanks to Bradley J. Thompson, Dr. Stewart "Tom" T. M. Fryslie, and Harshil Dave for their direct contribution to this work. Bradley has also helped with numerous other aspects of life, from how to build a computer to how to iron a shirt gracefully, for which I am very grateful. Working with Gautham Ragunathan, Janice Blane, Katie Lakomy, and Pawel Strzebonski has also been an enjoyable experience.

I am also fortunate to be surrounded by the great people in the ECE department. I would especially like to thank Prof. P. Scott Carney for his inspiring discussions and constant encouragement. I would also like to acknowledge my PhD committee members, Prof. Weng Cho Chew, Lynford L. Goddard, and Kejie Fang for their helpful feedback.

Thanks to my friends in the Physics department. They always feel like family to me. Special thanks to Prof. S. Lance Cooper for his continued support.

Finally, I am immensely grateful for the unconditional support from my parents. Their optimism and encouragement are the reason that I could travel light without worry in all the journeys I took.

TABLE OF CONTENTS

CHAPTER 1: INTRODUCTION

Coherently coupled semiconductor laser arrays have been studied experimentally and theoretically for more than four decades [1-11]. In addition to efforts towards achieving higher brightness and larger two-dimensional (2D) coherent arrays [12-16], another direction of recent research is focused on understanding and engineering of the interaction between two lasers under controlled nonuniformity between them [4, 17-31], which is the main theme of this dissertation. Through the mutual coupling and interaction between two semiconductor lasers, intriguing functionalities that are unique and often superior to those available from single lasers have been demonstrated. Examples include electronic control of emission angle steering [9, 17, 18, 20, 32], enhancements of modulation bandwidth [33-37], superior side-mode suppression [26, 38], and enhanced sensing sensitivities [39, 40]. However, to further improve the observed functionalities in a controlled, scalable and uniform manner, we face challenges on both theoretical considerations and experimental implementation, both of which motivate the work here.

Among the numerous reports exploring the interaction between two semiconductor lasers, a recent focus of research is the recognition of and emphasis on the tunable gain/loss profile in the coupled system [26, 30, 41-45]. Previously, coupled mode analysis mostly focused on the frequency detuning between resonators without emphasizing gain/loss contrast between them [46-49] with a rare exception [50]. In the past decade, the effects of gain/loss contrast between resonators have been extensively explored in the context of parity-time (PT) symmetry and non-Hermiticity in analogy to non-Hermitian quantum mechanics [26, 51-53]. Throughout this dissertation, we will repeatedly represent the gain/loss contrast between two coupled vertical cavity surface emitting lasers (VCSELs) in the form of non-Hermitian coupling matrix. In Chapter 2, we identify the gain/loss contrast between coupled VCSELs as the origin of beam steering (relative phase tuning) and analyze coupled diode laser arrays in the context of non-Hermitian photonics and PT symmetry [30, 54-56]. We discuss non-Hermiticity induced by the gain/loss contrast between two cavities, and also report non-Hermitian coupling induced by complex coupling coefficients [57].

In addition to recognizing the presence of gain/loss profile in coupled diode laser arrays, we present the first detailed analysis on the origin of gain/loss profile in coupled diode laser arrays [31]. For weakly coupled diode laser arrays, defined as the strength of optical coupling between cavities being weaker than the cavity loss rate (i.e., $|\kappa| < 1/\tau_p$), we demonstrate that gain/loss contrast between the two cavities originates from the cavity frequency detuning between them. This counterintuitive conclusion is the result of the interaction between photons and injected carriers that is unique in coupled semiconductor diode lasers. This unique mode tuning mechanism is inherently nonlinear, due to the presence of lasing threshold, gain pinning, and amplitude-phase coupling in diode lasers [58]. Because of the limitations of linear coupled mode theory, we present coupled rate equations analysis as the foundation for modeling these mode tuning mechanisms in Chapter 3 [31]. Note that the origin of relative phase tuning and beam steering in coupled lasers in the past has had two seemingly contradictory explanations. One opinion is that the phase tuning originates from the difference in modal gain of lasers [18], while the other opinion is that it originates from the resonant frequency detuning between cavities [25]. In Chapter 3 we show that the two theories do not conflict and can be unified in coupled rate equation analysis [31].

Besides analyzing the steady-state mode tuning and mode engineering in coupled diode lasers, the coupled rate equation analysis is also capable of analyzing the small-signal dynamics of the coupled laser array, including stability of the steady-state modes and high-speed modulation response, outlined in Chapter 4.

On the experimental side, the work described in this dissertation builds upon previous research on optically coupled electrically isolated VCSEL arrays [27, 32, 36, 59-61]. At the University of Illinois, 2 × 1 coherently coupled VCSEL arrays emitting at nominally 850 and 980 nm have been studied both experimentally and theoretically for more than a decade [8-10, 22, 23, 25, 27, 30, 35, 36, 60, 62, 63]. The device designs discussed in this dissertation employ photonic crystal (PhC) patterns for transverse mode confinement and stacked ion-implantation for carrier confinement and electrical isolation between individual lasers. Prior research on individual ion-implanted PhC VCSELs has shown that with proper design of the PhC pattern and ion-implantation apertures size, the individual VCSELs emit single-mode radiation over a large injection current range [64-67]. The VCSEL device designs in this dissertation utilized the designs from the prior research, which have been optimized for single-fundamental mode emission in each VCSEL as well as strong optical coupling between the two VCSEL elements of the array [8-10, 35, 36, 60, 62].

Electrical isolation between devices enables individual control of the carrier injection into each cavity. Previous research has shown that we can tune the array from two independent lasers into coherent phase-locking operation (phase synchronization between lasers) with the formation of a coherent supermode across both array elements by controlling the frequency detuning between the VCSELs through tuning the injection currents [27, 60]. Thus, when the VCSELs are phase-locked, they are also mutually coherent, as evident in the interference patterns in the far-field intensity profile [22, 23, 63]. When the VCSELs are phase-locked, we can also tune the relative phase between them by varying the injection currents, which leads to beam steering in the far field [23, 32, 68, 69].

The mode tuning described above for 2 element arrays has previously been characterized mostly when one of the injection currents is fixed and the other is varied. In Chapter 5, we present 2-dimensional (2D) characterizations of coherence and phase tuning when both injection currents are swept continuously. Previously undocumented phenomena have been revealed: for example the decrease of the coupling region and the increase of beam steering sensitivity with increasing bias, and the different mode tuning behavior near threshold versus above threshold. We have also observed a decrease in threshold current and an increase in output power due to optical coupling, which suggests non-Hermitian (active) coupling. We demonstrate that the mode tuning behavior can be engineered by intentionally introducing built-in symmetry between the two coupled lasers [56, 70]. Finally, by combining the theoretical analysis and experimental characterizations, we extract the coupling coefficient from the characterizations of the arrays, and is also included in Chapter 5.

The work presented in this dissertation is an advancement in the understanding and engineering of the interaction between two diode lasers. Chapters 2, 3 and 4 present theoretical methods in the modeling of coupled laser arrays, from the simple non-Hermitian coupled mode theory, to the coupled rate equations. Chapter 5 presents experimental progress on characterizations of the array operation and engineering the array operation through built-in asymmetries. The summary of this Dissertation and possible future research directions are included in Chapter 6.

1.1 References

[1] J. E. Ripper and T. L. Paoli, "Optical coupling of adjacent stripe-geometry junction lasers," *Applied Physics Letters,* vol. 17, no. 9, pp. 371-373, 1970.

[2] M. B. Spencer and W. E. Lamb, "Theory of two coupled lasers," *Physical Review A,* vol. 5, no. 2, pp. 893-898, 1972.

[3] D. R. Scifres, R. D. Burnham, and W. Streifer, "Phase-locked semiconductor-laser array," *Applied Physics Letters,* vol. 33, no. 12, pp. 1015-1017, 1978.

[4] E. Kapon, J. Katz, C. Lindsey, S. Margalit, and A. Yariv, "Control of mutual phase locking of monolithically integrated semiconductor lasers," *Applied Physics Letters,* vol. 43, no. 5, pp. 421-423, 1983.

[5] W. W. Chow, "Frequency locking in an index-guided semiconductor-laser array," *Journal of the Optical Society of America B-Optical Physics,* vol. 3, no. 6, pp. 833-836, 1986.

[6] S. S. Wang and H. G. Winful, "Dynamics of phase-locked semiconductor laser arrays," *Applied Physics Letters,* vol. 52, no. 21, pp. 1774-1776, 1988.

[7] D. Botez, “Monolithic phase-locked semiconductor laser arrays,” in *Diode Laser Arrays*, D. Botez and D. R. Scifres, Ed. New York: Cambridge University Press, 1994, pp. 1-72.

[8] A. J. Danner, J. C. Lee, J. J. Raftery, N. Yokouchi, and K. D. Choquette, "Coupled-defect photonic crystal vertical cavity surface emitting lasers," *Electronics Letters,* vol. 39, no. 18, pp. 1323-1324, 2003.

[9] A. C. Lehman, J. J. Raftery, A. J. Danner, P. O. Leisher, and K. D. Choquette, "Relative phase tuning of coupled defects in photonic crystal vertical-cavity surface-emitting lasers," *Applied Physics Letters,* vol. 88, no. 2, p. 021102, 2006.

[10] D. F. Siriani and K. D. Choquette, "Implant defined anti-guided vertical-cavity surface-emitting laser arrays," *IEEE Journal of Quantum Electronics,* vol. 47, no. 2, pp. 160-164, 2011.

[11] D. F. Siriani and K. D. Choquette, "Coherent coupling of vertical-cavity surface-emitting laser arrays," in *Advances in Semiconductor Lasers*, vol. 861, ed.: Elsevier Inc., 2012, pp. 227-267.

[12] L. J. Mawst *et al.*, "Resonant self-aligned-stripe antiguided diode-laser array," *Applied Physics Letters,* vol. 60, no. 6, pp. 668-670, 1992.

[13] L. Bao *et al.*, "Near-diffraction-limited coherent emission from large aperture antiguided vertical-cavity surface-emitting laser arrays," *Applied Physics Letters,* vol. 84, no. 3, pp. 320-322, 2004.

[14] D. F. Siriani and K. D. Choquette, "In-phase coherent photonic crystal vertical-cavity surface-emitting laser arrays with low divergence," *Electronics Letters,* vol. 46, no. 10, pp. 712-713, 2010.

[15] M.-M. Mao *et al.*, "Implant-defined 3 x 3 in-phase coherently coupled vertical cavity surface emitting lasers array," *IEEE Photonics Journal,* vol. 5, no. 6, p. 1502606, 2013.

[16] Z. Gao, B. J. Thompson, G. Ragunathan, M. T. Johnson, B. Rout, and K. D. Choquette, "Bottom-emitting coherently coupled vertical cavity laser arrays," *IEEE Photonics Technology Letters,* vol. 28, no. 4, pp. 513-515, 2016.

[17] D. R. Scifres, W. Streifer, and R. D. Burnham, "Beam scanning with twin-stripe injection-lasers," *Applied Physics Letters,* vol. 33, no. 8, pp. 702-704, 1978.

[18] E. Kapon, Z. Rav-Noy, L. T. Lu, M. Yi, S. Margalit, and A. Yariv, "Phase-locking characteristics of coupled ridge-waveguide InP/InGaAsP diode lasers," *Applied Physics Letters*, vol. 45, no. 11, pp. 1159-1161, 1984.

[19] J. Katz, E. Kapon, C. Lindsey, S. Margalit, and A. Yariv, "Coupling coefficient of gain-guided lasers," *Applied Optics*, vol. 23, no. 14, pp. 2231-2233, 1984.

[20] L. D. A. Lundeberg and E. Kapon, "Mode switching and beam steering in photonic crystal heterostructures implemented with vertical-cavity surface-emitting lasers," *Applied Physics Letters*, vol. 90, no. 24, pp. 2005-2008, 2007.

[21] K. A. Atlasov, K. F. Karlsson, A. Rudra, B. Dwir, and E. Kapon, "Wavelength and loss splitting in directly coupled photonic-crystal defect microcavities," *Optics Express*, vol. 16, no. 20, pp. 16255-16264, 2008.

[22] D. F. Siriani, P. S. Carney, and K. D. Choquette, "Coherence of leaky-mode vertical-cavity surface-emitting laser arrays," *IEEE Journal of Quantum Electronics*, vol. 47, no. 5, pp. 672-675, 2011.

[23] M. T. Johnson, D. F. Siriani, J. D. Sulkin, and K. D. Choquette, "Phase and coherence extraction from a phased vertical cavity laser array," *Applied Physics Letters*, vol. 101, no. 3, p. 031116, 2012.

[24] M. Liertzer, L. Ge, A. Cerjan, A. D. Stone, H. E. Tureci, and S. Rotter, "Pump-induced exceptional points in lasers," *Phys Rev Lett*, vol. 108, no. 17, p. 173901, 2012.

[25] M. T. Johnson, D. F. Siriani, M. P. Tan, and K. D. Choquette, "Beam steering via resonance detuning in coherently coupled vertical cavity laser arrays," *Applied Physics Letters*, vol. 103, no. 20, p. 201115, 2013.

[26] H. Hodaei, M. A. Miri, M. Heinrich, D. N. Christodoulides, and M. Khajavikhan, "Parity-time-symmetric microring lasers," *Science*, vol. 346, no. 6212, pp. 975-978, 2014.

[27] S. T. M. Fryslie, M. T. Johnson, and K. D. Choquette, "Coherence tuning in optically coupled phased vertical cavity laser arrays," *IEEE Journal of Quantum Electronics*, vol. 51, no. 11, pp. 1-6, 2015.

[28] M. J. Adams, N. Li, B. R. Cemlyn, H. Susanto, and I. D. Henning, "Effects of detuning, gain-guiding, and index antiguiding on the dynamics of two laterally coupled semiconductor lasers," *Physical Review A*, vol. 95, no. 5, p. 053869, 2017.

[29] Y. Kominis, V. Kovanis, and T. Bountis, "Controllable asymmetric phase-locked states of the fundamental active photonic dimer," *Physical Review A*, vol. 96, no. 4, p. 043836, 2017.

[30] Z. Gao, S. T. Fryslie, B. J. Thompson, P. S. Carney, and K. D. Choquette, "Parity-time symmetry in coherently coupled vertical cavity laser arrays," *Optica*, vol. 4, no. 3, pp. 323-329, 2017.

[31] Z. Gao, M. T. Johnson, and K. D. Choquette, "Rate equation analysis and non-Hermiticity in coupled semiconductor laser arrays," *Journal of Applied Physics*, vol. 123, no. 17, p. 173102, 2018.

[32] M. T. Johnson, D. F. Siriani, M. P. Tan, and K. D. Choquette, "High-speed beam steering with phased vertical cavity laser arrays," *IEEE Journal of Selected Topics in Quantum Electronics*, vol. 19, no. 4, p. 1701006, 2013.

[33] H. Dalir and F. Koyama, "29 GHz directly modulated 980 nm vertical-cavity surface emitting lasers with bow-tie shape transverse coupled cavity," *Applied Physics Letters*, vol. 103, no. 9, p. 091109, 2013.

[34] S. T. Hu, M. Ahmed, A. Bakry, and F. Koyama, "Low chirp and high-speed operation of transverse coupled cavity VCSEL," *Japanese Journal of Applied Physics,* vol. 54, no. 9, p. 090304, 2015.
[35] S. T. M. Fryslie, M. P. Tan, D. F. Siriani, M. T. Johnson, and K. D. Choquette, "37-GHz modulation via resonance tuning in Single-Mode Coherent Vertical-Cavity Laser Arrays," *IEEE Photonics Technology Letters,* vol. 27, no. 4, pp. 415-418, 2015.
[36] S. T. M. Fryslie *et al.*, "Modulation of coherently coupled phased photonic crystal vertical cavity laser arrays," *IEEE Journal of Selected Topics in Quantum Electronics,* vol. 23, no. 6, pp. 1-9, 2017.
[37] Z. X. Xiao, Y. Z. Huang, Y. D. Yang, M. Tang, and J. L. Xiao, "Modulation bandwidth enhancement for coupled twin-square microcavity lasers," *Opt Lett,* vol. 42, no. 16, pp. 3173-3176, 2017.
[38] H. Hodaei *et al.*, "Design considerations for single-mode microring lasers using parity–time symmetry," *IEEE Journal of Selected Topics in Quantum Electronics,* vol. 22, no. 5, pp. 1-7, 2016.
[39] W. Chen, S. Kaya Ozdemir, G. Zhao, J. Wiersig, and L. Yang, "Exceptional points enhance sensing in an optical microcavity," *Nature,* vol. 548, no. 7666, pp. 192-196, 2017.
[40] H. Hodaei *et al.*, "Enhanced sensitivity at higher-order exceptional points," *Nature,* vol. 548, no. 7666, pp. 187-191, 2017.
[41] A. Guo *et al.*, "Observation of PT-symmetry breaking in complex optical potentials," *Phys Rev Lett,* vol. 103, no. 9, p. 093902, 2009.
[42] H. Benisty *et al.*, "Implementation of PT symmetric devices using plasmonics: principle and applications," *Opt Express,* vol. 19, no. 19, pp. 18004-19, 2011.
[43] R. El-Ganainy, M. Khajavikhan, and L. Ge, "Exceptional points and lasing self-termination in photonic molecules," *Physical Review A,* vol. 90, no. 1, pp. 013802-013802, 2014.
[44] B. Peng *et al.*, "Parity–time-symmetric whispering-gallery microcavities," *Nature Physics,* vol. 10, no. 5, pp. 394-398, 2014.
[45] L. Chang *et al.*, "Parity–time symmetry and variable optical isolation in active–passive-coupled microresonators," *Nature Photonics,* vol. 8, no. 7, pp. 524-529, 2014.
[46] D. Marcuse, "The coupling of degenerate modes in two parallel dielectric waveguides," *Bell System Technical Journal,* vol. 50, no. 6, pp. 1791-1816, 1971.
[47] A. Yariv, "Coupled-Mode Theory for Guided-Wave Optics," *IEEE Journal of Quantum Electronics,* vol. Qe 9, no. 9, pp. 919-933, 1973.
[48] H. Haus, W. Huang, S. Kawakami, and N. Whitaker, "Coupled-mode theory of optical waveguides," *Journal of Lightwave Technology,* vol. 5, no. 1, pp. 16-23, 1987.
[49] S. L. Chuang, *Physics of Photonic Devices,* 2nd ed. (Wiley series in pure and applied optics). Hoboken, N.J.: John Wiley & Sons, 2009.
[50] G. H. B. Thompson, "Analysis of optical directional-couplers that include gain or loss and their application to semiconductor slab dielectric guides," *Journal of Lightwave Technology,* vol. 4, no. 11, pp. 1678-1693, 1986.
[51] C. M. Bender and S. Boettcher, "Real spectra in non-Hermitian Hamiltonians having PT symmetry," *Physical Review Letters,* vol. 80, no. 24, pp. 5243-5246, 1998.
[52] R. El-Ganainy, K. G. Makris, D. N. Christodoulides, and Z. H. Musslimani, "Theory of coupled optical PT-symmetric structures," *Opt Lett,* vol. 32, no. 17, pp. 2632-4, 2007.

[53] L. Feng, R. El-Ganainy, and L. Ge, "Non-Hermitian photonics based on parity–time symmetry," *Nature Photonics,* vol. 11, no. 12, pp. 752-762, 2017.

[54] Z. Gao, S. Fryslie, B. J. Thompson, P. S. Carney, and K. D. Choquette, "Coherently coupled vertical cavity laser arrays with frequency detuning and asymmetric gain distribution," in *CLEO: Science and Innovations,* 2016, p. SF1L. 3: Optical Society of America.

[55] Z. Gao, S. T. Fryslie, B. J. Thompson, M. T. Johnson, and K. D. Choquette, "Parity-time symmetry analogs in coherently coupled vertical cavity laser arrays," in *IEEE Photonics Conference (IPC),* 2016, pp. 329-330

[56] Z. Gao *et al.*, "Non-Hermitian aspects of coherently coupled vertical cavity laser arrays," in *CLEO: Science and Innovations*, 2017, p. SW1C. 4: Optical Society of America.

[57] S. Longhi and L. Feng, "Non-Hermitian laser phase locking," *arXiv preprint arXiv:1802.05439,* 2018.

[58] C. H. Henry, "Theory of the linewidth of semiconductor-lasers," *IEEE Journal of Quantum Electronics*, vol. 18, no. 2, pp. 259-264, 1982.

[59] B. Thompson, D. F. Siriani, and K. D. Choquette, "Coherent operation of 2×2 vertical cavity laser array by resonance tuning," in *2015 IEEE Photonics Conference (IPC)* vol. 3, ed: IEEE, 2015, pp. 589-590.

[60] B. J. Thompson, Z. Gao, S. T. Fryslie, M. T. Johnson, D. F. Siriani, and K. D. Choquette, "Coherence in multielement-phased vertical-cavity surface-emitting laser arrays using resonance tuning," *IEEE Photonics Journal,* vol. 9, no. 5, pp. 1-8, 2017.

[61] B. J. Thompson, Z. Gao, H. Dave, S. T. Fryslie, K. Lakomy, and K. D. Choquette, "Classification of coherent supermodes in photonic crystal vertical cavity laser arrays," in *IEEE Photonics Conference (IPC)*, 2017, pp. 529-530

[62] J. J. Raftery, A. C. Lehman, A. J. Danner, P. O. Leisher, A. V. Giannopoulos, and K. D. Choquette, "In-phase evanescent coupling of two-dimensional arrays of defect cavities in photonic crystal vertical cavity surface emitting lasers," *Applied Physics Letters,* vol. 89, no. 8, pp. 081119-081119, 2006.

[63] D. F. Siriani, K. D. Choquette, and P. S. Carney, "Stochastic coupled mode theory for partially coherent laser arrays," *J Opt Soc Am A,* vol. 27, no. 3, pp. 501-508, 2010.

[64] N. Yokouchi, A. J. Danner, and K. D. Choquette, "Two-dimensional photonic crystal confined vertical-cavity surface-emitting lasers," *IEEE Journal of Selected Topics in Quantum Electronics,* vol. 9, no. 5, pp. 1439-1445, 2003.

[65] P. O. Leisher, J. D. Sulkin, and K. D. Choquette, "Parametric study of proton-implanted photonic crystal vertical-cavity surface-emitting lasers," *IEEE Journal of Selected Topics in Quantum Electronics,* vol. 13, no. 5, pp. 1290-1294, 2007.

[66] D. F. Siriani, P. O. Leisher, and K. D. Choquette, "Loss-induced confinement in photonic crystal vertical-cavity surface-emitting lasers," *IEEE Journal of Quantum Electronics,* vol. 45, no. 7, pp. 762-768, 2009.

[67] M. P. Tan, A. M. Kasten, J. D. Sulkin, and K. D. Choquette, "Planar photonic crystal vertical-cavity surface-emitting lasers," *IEEE Journal of Selected Topics in Quantum Electronics,* vol. 19, no. 4, p. 4900107, 2013.

[68] A. C. Lehman, D. F. Siriani, and K. D. Choquette, "Two-dimensional electronic beam-steering with implant-defined coherent VCSEL arrays," *Electronics Letters,* vol. 43, no. 22, pp. 1202-1203, 2007.

[69] D. Siriani and K. Choquette, "Electronically controlled two-dimensional steering of in-phase coherently coupled vertical-cavity laser arrays," *Photonics Technology Letters, IEEE,* vol. 23, pp. 167-169, 2011.

[70] Z. Gao, B. J. Thompson, H. Dave, S. T. Fryslie, and K. D. Choquette, "Harnessing the asymmetry in coherently coupled 2×1 VCSEL arrays," in *IEEE Photonics Conference (IPC)*, 2017, pp. 535-536

CHAPTER 2: COUPLED MODE THEORY AND NON-HERMITICITY

Coupled mode theory (CMT) is an essential tool in the study of coupled waveguides or resonators [1-4]. It has been used to investigate coupled laser arrays including coupled VCSEL arrays [5-8]. In this chapter, I will show that CMT offers a simple explanation of the origin of phase and intensity tuning that we experimentally observe in coupled laser arrays [7, 9-11]. Notions of parity-time (PT) symmetry and non-Hermiticity can be defined in CMT, in analogy to the non-Hermitian Hamiltonian in quantum mechanics [12-17]. This analogy has not only made photonics an experimentally accessible system to emulate non-Hermitian quantum mechanics, but it has also inspired numerous novel device designs and functionalities in photonics [15, 18-21]. However, it will be shown that CMT requires gain/loss contrast and frequency detuning as input parameters, both of which are challenging to measure or control in experiments. This issue will be addressed in Chapter 3 by incorporating the coupled rate equations, an approach that is based on CMT yet also takes carrier dynamics into consideration.

In this chapter, we first introduce the coupled mode theory in a side-by-side coupled laser system with a brief statement of definitions and assumptions. The detailed derivation of CMT from Maxwell's equations can be found in Appendix A. We then introduce the concept of non-Hermiticity, PT symmetry, and exceptional points in the context of CMT. The dependence of coupled mode on the frequency detuning and gain contrast between two resonators will be illustrated. Non-Hermiticity as the origin of beam steering will be shown. After establishing the language of CMT and non-Hermiticity, we will look into different systems for which CMT can be used, which includes coupled resonators without gain/loss profile (Section 2.3), coupled lasers with gain/loss profile (Section 2.4), and passive index-antiguided coupling (Section 2.5). We categorize the coupled system with the Hermiticity/non-Hermiticity of the coupling matrix, and show different kinds of non-Hermiticity. In addition to the non-Hermiticity induced by gain/loss contrast between two lasers, we also show the situations when the coupling coefficient induces non-Hermiticity, due to the gain splitting between normal modes.

Herein we emphasize that the coupling coefficient may not always be real and positive, as is the case for passive evanescent coupling. The coupling coefficient is real-valued when the gain/loss in the array is uniform, or can be approximated as uniform within each cavity (for example in index-guided lasers where gain-guiding is negligible). In general, the coupling coefficients are complex numbers and should be interpreted as the splitting between complex frequencies of the two coupled modes (normal modes of the composite system). Any gain/loss mechanism that favors the in-phase mode (suppresses the out-of-phase mode) would introduce a negative imaginary part in the coupling coefficient, while any gain/loss mechanism that favors the out-of-phase mode would introduce a positive imaginary part. Also, the real part of the coupling coefficient may be negative, which we discuss in the index-antiguided coupling case.

2.1 Temporal coupled mode theory

Coupled mode theory was originally introduced in evanescently coupled index-guided waveguides [1, 2]. Although it has been shown to work well for gain-guided laser and even index-antiguided lasers as well [7, 22], here we introduce the concept in the context of two evanescently coupled index-guided lasers. Although edge-emitting semiconductor lasers have significant device structure differences with VCSELs, these differences are irrelevant for the construction of a simple model for laterally coupled VCSELs. Later in this chapter, we will discuss the generalization of coupled mode theory in index-antiguided lasers and in systems with nonuniform gain/loss profile.

In a system of two index-guided lasers that are laterally coupled (i.e. the coupling occurs perpendicular to the direction of light propagation), we can approximate this system with a 2D model in the spirit of the effective index method [23]. The effective index profile $\epsilon_C(x,z)$ is sketched in Figure 2.1(a). The two coupled lasers are modeled as two index-guided stripe waveguides coupled in the x-direction and propagating in the z-direction, with high-reflectivity mirrors terminating the waveguides at $z = 0$ and $z = -L$. In other words, the longitudinal modes are in the z-direction and transverse modes are in the x-direction.

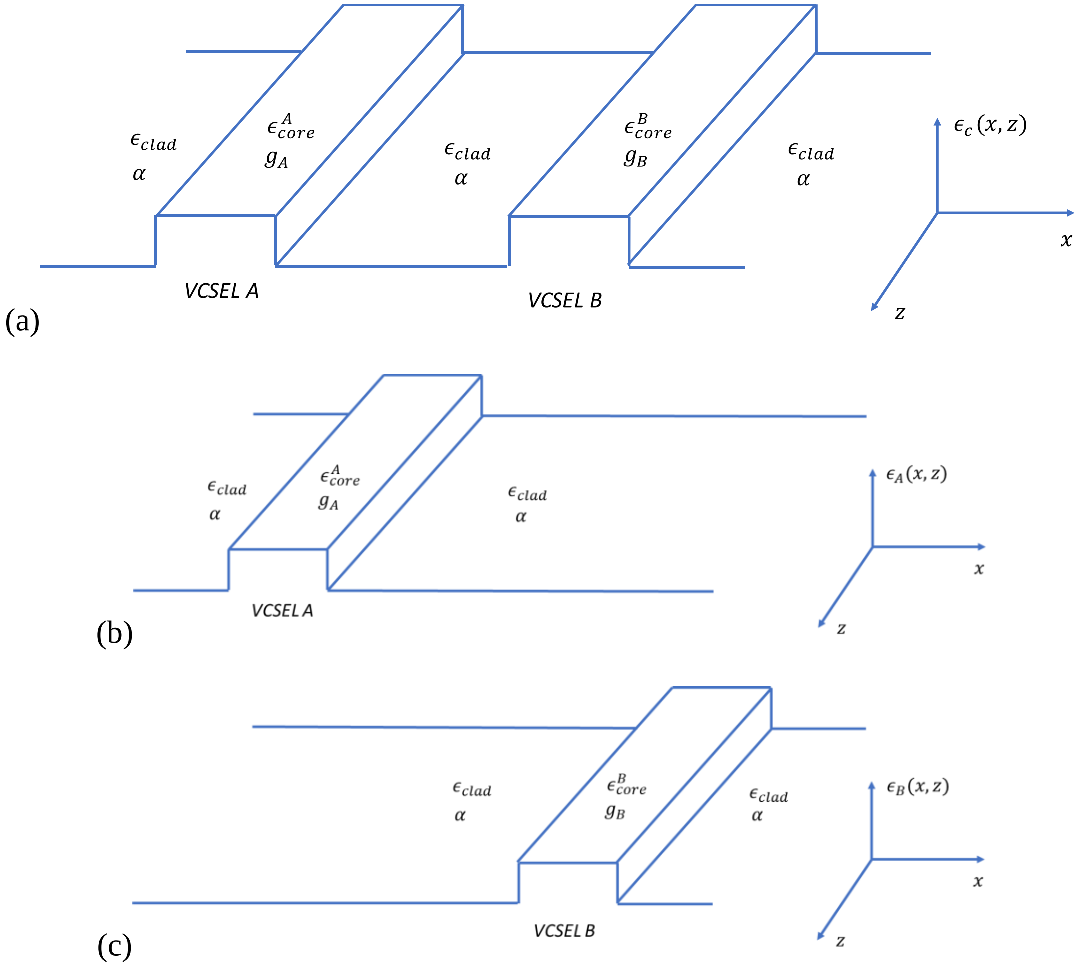

Figure 2.1: (a) Permittivity profile for the coupled laser array in a two-dimensional model, i.e., $\epsilon_C(x,z)$. (b) Permittivity profile when cavity B is absent, i.e., $\epsilon_A(x,z)$. (c) Permittivity profile when cavity A is absent, i.e., $\epsilon_B(x,z)$.

With this index profile, we further simplify the problem by assuming that each laser only has emission in a single optical mode. Then the total electric field in the array can be expanded using the individual laser modes as the basis functions:

$$\mathcal{E}_{tot}(x,z,t) = u_A(x,z)\mathcal{E}_A(t) + u_B(x,z)\mathcal{E}_B(t) \tag{2.1}$$

where $u_A(x,z)$ and $u_B(x,z)$ are the basis functions (i.e., spatial mode profiles when Laser A and B are isolated), and $\mathcal{E}_{A,B}(t)$ are the complex field amplitudes that describe the temporal variation. [$\mathcal{E}_{A,B}(t)$ can be further identified as $\mathcal{E}_{A,B}(t) = E_{A,B}(t)e^{-i\omega t} = \left|E_{A,B}(t)\right|e^{-i\phi_{A,B}(t)}e^{-i\omega t}$, where we can factor out the slowly varying envelope $E_{A,B}(t)$ from the fast oscillating $e^{-i\omega t}$ term.] The terms $\mathcal{E}_{A,B}(t)$ are the unknown variables describing the coupled modes and their temporal evolution that we want to solve using the coupled mode theory. The $\mathcal{E}_{A,B}(t)$ are governed by the coupled mode equations:

$$\dot{\mathcal{E}}_A = -i\omega_A\mathcal{E}_A + \gamma_A\mathcal{E}_A + i\kappa_{AB}\mathcal{E}_B \tag{2.2}$$

$$\dot{\mathcal{E}}_B = -i\omega_B\mathcal{E}_B + \gamma_B\mathcal{E}_B + i\kappa_{BA}\mathcal{E}_A \tag{2.3}$$

where $\omega_{A,B}$ are the local resonant frequencies of cavity A and B, $\gamma_{A,B}$ are the local modal gain/loss in cavities A and B (positive represents gain, negative represents loss), and $\kappa_{AB,BA}$ are the coupling coefficients. Equations (2.2) and (2.3) can also be derived from Maxwell's equations, the details of which are given in Appendix A.

For evanescent coupling, arising for example from the index profile shown in Figure 2.1(a), we have

$$\kappa_{AB} = \frac{\omega}{2}\frac{\int_{-\infty}^{\infty} u_A^*(\epsilon_C - \epsilon_B)u_B dx}{\int_{-\infty}^{\infty} u_A^*\epsilon_A u_A dx} \equiv \frac{\omega}{2}\frac{\langle u_A|\epsilon_C - \epsilon_B|u_B\rangle}{\langle u_A|\epsilon_A|u_A\rangle} \tag{2.4}$$

$$\kappa_{BA} = \frac{\omega}{2}\frac{\int_{-\infty}^{\infty} u_B^*(\epsilon_C - \epsilon_A)u_A dx}{\int_{-\infty}^{\infty} u_B^*\epsilon_B u_B dx} = \frac{\omega}{2}\frac{\langle u_B|\epsilon_C - \epsilon_A|u_A\rangle}{\langle u_B|\epsilon_B|u_B\rangle} \tag{2.5}$$

where $\epsilon_{A,B}(x)$ are the cross-sectional index profile for the isolated lasers, sketched in Figure 2.1(b) and (c) respectively. We have dropped the dependence on z in $\epsilon_{C,A,B}(x)$ because they are invariant along the z-axis in this simple model, and hence $\kappa_{AB,BA}$ are also invariant along the z-axis.

In a compact form, we can write Equations (2.2) and (2.3) as

$$\frac{d}{dt}\bar{\boldsymbol{\mathcal{E}}} = -i\bar{\bar{\mathbf{M}}}\bar{\boldsymbol{\mathcal{E}}} \tag{2.6}$$

where $\bar{\boldsymbol{\mathcal{E}}} \equiv \begin{bmatrix} \mathcal{E}_A \\ \mathcal{E}_B \end{bmatrix}$, $\bar{\bar{\mathbf{M}}} \equiv \begin{bmatrix} \omega_A + i\gamma_A & -\kappa_{AB} \\ -\kappa_{BA} & \omega_B + i\gamma_B \end{bmatrix}$. We call $\bar{\bar{\mathbf{M}}}$ the coupling matrix. We will show in the following paragraphs that eigenvectors of $\bar{\bar{\mathbf{M}}}$ represent normal modes in the coupled laser array, and the eigenvalues of $\bar{\bar{\mathbf{M}}}$ are the complex-valued frequencies of the normal modes.

Demanding that the field amplitudes be time-harmonic, i.e.,

$$\bar{\boldsymbol{\mathcal{E}}} \equiv \begin{bmatrix} \mathcal{E}_A \\ \mathcal{E}_B \end{bmatrix} = \begin{bmatrix} E_A \\ E_B \end{bmatrix} e^{-i\omega t} \equiv \bar{\mathbf{E}} e^{-i\omega t} \tag{2.7}$$

and that $E_{A,B}$ have no temporal dependence, Equation (2.6) becomes an eigenvalue problem:

$$\bar{\bar{\mathbf{M}}}\bar{\mathbf{E}} = \omega\bar{\mathbf{E}} \tag{2.8}$$

The eigenvalue ω represents the complex frequency of the normal modes, with real part representing the angular frequency and imaginary part representing the gain/loss coefficient. The eigenvector $\bar{\mathbf{E}}$ represents the composition of the normal modes, which are superpositions of the two individual modes of the isolated lasers. For example, in the case of two identical passive lossless resonators that are evanescently coupled (discussed in Section 2.3), $\bar{\bar{\mathbf{M}}} = \begin{bmatrix} \omega_0 & -\kappa \\ -\kappa & \omega_0 \end{bmatrix}$. The eigenvectors of $\bar{\bar{\mathbf{M}}}$ are $\bar{\mathbf{E}} = \begin{bmatrix} 1 \\ 1 \end{bmatrix}$ and $\begin{bmatrix} 1 \\ -1 \end{bmatrix}$, representing the symmetrical ($E_+ = u_A + u_B$) and anti-symmetrical ($E_- = u_A - u_B$) normal modes. The eigenvalues are $\omega = \omega_0 \mp \kappa$, with no imaginary component, which is consistent with the frequency splitting due to coupling and the assumption that the system is passive and lossless.

In general, the eigenvalue equation (2.8) has solution as

$$\omega = \frac{\omega_A + \omega_B}{2} + \frac{i(\gamma_A + \gamma_B)}{2} \pm \left[\kappa_{AB}\kappa_{BA} + \left(\frac{\omega_A - \omega_B}{2}\right)^2 - \left(\frac{\gamma_A - \gamma_B}{2}\right)^2 + i\,\frac{(\omega_A - \omega_B)(\gamma_A - \gamma_B)}{2}\right]^{\frac{1}{2}} \tag{2.9}$$

and $\bar{\mathbf{E}}$ can be calculated from eigenvalues by

$$\frac{E_B}{E_A} = \frac{-i\kappa_{BA}}{i(\omega - \omega_B) + \gamma_B} \tag{2.10}$$

In the context of coupled VCSEL arrays, the magnitude $|E_B/E_A|$ controls the near field intensity profile of the coupled mode, while the phase $Arg(E_B/E_A)$ determines the relative phase difference between the fields emitted from the two array elements, which overall leads to beam steering in the far field (i.e. off normal-axis propagation direction) [7, 10, 24]. Equations (2.9) and (2.10) take simpler forms when there is only gain contrast or frequency detuning, as discussed in detail in Refs. [23, 25-27], for example. We will apply these discussions later in the context of coupled VCSEL arrays to explain how gain/loss contrast induces phase tuning and how frequency detuning induces near field intensity tuning.

It is convenient to categorize coupled resonator arrays according to the mathematical properties of $\bar{\bar{\mathbf{M}}}$, and doing so can provide mathematical insight. For example, passive coupled resonators (lossless or with uniform loss) have real-valued $\bar{\bar{\mathbf{M}}}$, hence the eigenvectors are real and the relative phase between two resonators is either 0 or π, which is not tunable. On the other hand, two coupled lasers with gain/loss contrast between cavities would have a complex and non-Hermitian $\bar{\bar{\mathbf{M}}}$. A matrix is said to be Hermitian if it is equal to its adjoint (i.e.$\bar{\bar{\boldsymbol{A}}} = \bar{\bar{\boldsymbol{A}}}^{\dagger}$). The identification of a non-Hermitian $\bar{\bar{\mathbf{M}}}$ inherently provides the explanation for the phase tuning (beam steering) that has been observed for decades [9, 28, 29], and also provides new perspective. Non-Hermitian $\bar{\bar{\mathbf{M}}}$ predicts intriguing new properties, such as operation around exceptional points which possess collapsed identical modes [20, 21, 30].

2.2 Non-Hermiticity, parity-time symmetry, and exceptional points

We see that Equation (2.6) has the same form as the Schrödinger equation in quantum mechanics: ($\frac{d}{dt}\psi = -\frac{i}{\hbar}\,\hat{\mathbf{H}}\psi$), with the coupling matrix $\bar{\bar{\mathbf{M}}}$ playing the same role as the Hamiltonian, $\hat{\mathbf{H}}$. This shared mathematical form enables an analogy between two coupled resonators and a quantum-mechanical system. Parity-time (PT) symmetry and non-Hermiticity can be defined in analogy to non-Hermitian quantum mechanics [12, 31]. In this dissertation, we define the Hermiticity/non-Hermiticity of the system according to the Hermiticity/non-Hermiticity of the coupling matrix $\bar{\bar{\mathbf{M}}}$. This is in analogy with the Hamiltonian of a quantum particle inhabiting a coordinate axis that consists of just the two points $x = \pm 1$ (in which case the Hamiltonian is also a 2×2 matrix) [31]. When there is no gain/loss in the system (i.e., everything is passive and energy is conserved), $\bar{\bar{\mathbf{M}}}$ is Hermitian (i.e., $\bar{\bar{\mathbf{M}}}^\dagger = \bar{\bar{\mathbf{M}}}$, $\gamma_A = \gamma_B = 0$, $\kappa_{AB} = \kappa_{BA}^*$) [23, 32]. With the addition of gain/loss into the system, $\bar{\bar{\mathbf{M}}}$ is in general non-Hermitian. Two origins of non-Hermiticity, namely gain/loss contrast that can introduce nonzero $\gamma_{A,B}$ and/or non-Hermitian coupling (i.e., $\kappa_{AB} \neq \kappa_{BA}^*$), will both be discussed in the following sections.

PT symmetry is a special type of non-Hermiticity that has been a focus of research recently because of its intriguing properties. If we introduce precisely balanced gain/loss into two cavities that are otherwise identical (i.e., $\omega_A = \omega_B, \gamma_A = -\gamma_B$) and assuming that the gain/loss are uniform within each cavity, then $\bar{\bar{\mathbf{M}}}$ is non-Hermitian but remains PT symmetric (i.e., $\bar{\bar{\mathbf{M}}}^{\dagger} \neq \bar{\bar{\mathbf{M}}}$, $\hat{\boldsymbol{P}}\hat{\boldsymbol{T}}\bar{\bar{\mathbf{M}}} = \bar{\bar{\mathbf{M}}}$).

The parity operator $\hat{\boldsymbol{P}}$ flips the signs of all spatial coordinates. Within the formulism of coupled mode theory [i.e. Equation (2.6)], it switches subscript A with B. The time-reversal operator $\hat{\boldsymbol{T}}$ reverses the sign of time (i.e., $t \to -t$). When the coupled mode equation is considered, time reversal is equivalent to complex conjugation $i \to -i$. This is formally in analogy with quantum mechanics theory, but also it has an intuitive meaning in optics: it interchanges gain with loss. The total effect of $\hat{\boldsymbol{P}}\hat{\boldsymbol{T}}$ operation on $\bar{\bar{\mathbf{M}}}$ is

$$\left[\hat{\boldsymbol{P}}\hat{\boldsymbol{T}}\bar{\bar{\mathbf{M}}}\right]_{m,n} = \bar{\bar{\mathbf{M}}}^{*}_{3-m,3-n} \tag{2.11}$$

where $m, n = 1{,}2$ are the matrix indexes. In other words, if

$$\bar{\bar{\mathbf{M}}} = \begin{bmatrix} \omega_A + i\gamma_A & -\kappa_{AB} \\ -\kappa_{BA} & \omega_B + i\gamma_B \end{bmatrix}$$

then we have

$$\hat{\boldsymbol{P}}\hat{\boldsymbol{T}}\bar{\bar{\mathbf{M}}} = \begin{bmatrix} \omega_B - i\gamma_B & -\kappa^{*}_{BA} \\ -\kappa^{*}_{AB} & \omega_A - i\gamma_A \end{bmatrix} \tag{2.11b}$$

PT symmetric $\bar{\bar{\mathbf{M}}}$ requires that $\hat{\boldsymbol{P}}\hat{\boldsymbol{T}}\bar{\bar{\mathbf{M}}} = \bar{\bar{\mathbf{M}}}$, which requires

$$\begin{cases} \omega_A = \omega_B \\ \gamma_A = -\gamma_B \\ \kappa_{AB} = \kappa^{*}_{BA} \end{cases} \tag{2.12}$$

In general, Hermitian matrix $\bar{\bar{\mathbf{M}}}$ has real spectra and orthogonal eigenvectors, while non-Hermitian $\bar{\bar{\mathbf{M}}}$ may have complex spectra and non-orthogonal eigenvectors. PT symmetry is a special kind of non-Hermiticity because PT-symmetric $\bar{\bar{\mathbf{M}}}$ may also have real spectra. When the system possesses unbroken PT symmetry, meaning that both the system and its eigenmodes are PT symmetric, the spectra are real. On the other hand, when the system possesses broken PT symmetry, meaning that $\bar{\bar{\mathbf{M}}}$ is PT symmetric but its eigenmodes are not, the spectra are complex.

Moreover, PT-symmetric $\bar{\bar{\mathbf{M}}}$ may have collapsed eigenvectors, meaning that the two sets of eigenvectors become identical and no longer span a 2D vector space. This collapse of eigenvectors happens under certain conditions and are called *exceptional points*. Intriguing phenomena including enhanced sensing sensitivity have been demonstrated around the exceptional points [20, 21]. When the coupling coefficients are real and symmetrical (i.e., $\kappa_{AB} = \kappa_{BA} = \kappa$), exceptional points are at $\omega_A = \omega_B, \gamma_A - \gamma_B = \pm 2\kappa$. More generally, exceptional points can be identified when Equation (2.9) has two identical roots, meaning that

$$\kappa_{AB}\kappa_{BA} + \left(\frac{\omega_A - \omega_B}{2}\right)^2 - \left(\frac{\gamma_A - \gamma_B}{2}\right)^2 + i\frac{(\omega_A - \omega_B)(\gamma_A - \gamma_B)}{2} = 0 \qquad (2.13)$$

Now let us see how the coupled modes $\bar{\mathbf{E}}$ vary with gain/loss contrast and frequency detuning in $\bar{\bar{\mathbf{M}}}$. For simplicity we set the coupling coefficients to be symmetric, real valued, and positive: $\kappa_{AB} = \kappa_{BA} = \kappa > 0$. This is equivalent to assuming negligible deviation in the coupling coefficients from the case of two evanescently coupled passive resonators. This assumption will be justified and further discussed in the following sections.

When the two laser resonators of the array have different native resonant frequencies, but experience no gain/loss contrast (i.e., $\gamma_A = \gamma_B = 0, \omega_A \neq \omega_B$), the coupling matrix $\bar{\bar{\mathbf{M}}}$ is real and symmetrical (also Hermitian). The wavelength, modal gain, and field amplitude ratio (both magnitude and phase) of the coupled modes are derived from the eigenvalues and eigenvectors of $\bar{\bar{\mathbf{M}}}$ and are illustrated in Figure 2.2 [17]. This is the situation often described in textbooks, for example in [23]. The frequency detuning between the two native resonances changes the coupled-mode intensity distribution, such that the out-of-phase mode has more intensity in the cavity with higher natural resonant frequency, while the in-phase mode has more intensity in the cavity with lower natural resonant frequency. The degree of intensity distribution asymmetry increases with frequency detuning as shown in Figure 2.2(c). The fact that the eigenvector $\bar{\mathbf{E}}$ is purely real for a real $\bar{\bar{\mathbf{M}}}$ means no phase tuning or beam steering is induced since the phases remain constant as gain contrast varies, as shown in Figure 2.2(d) [17].

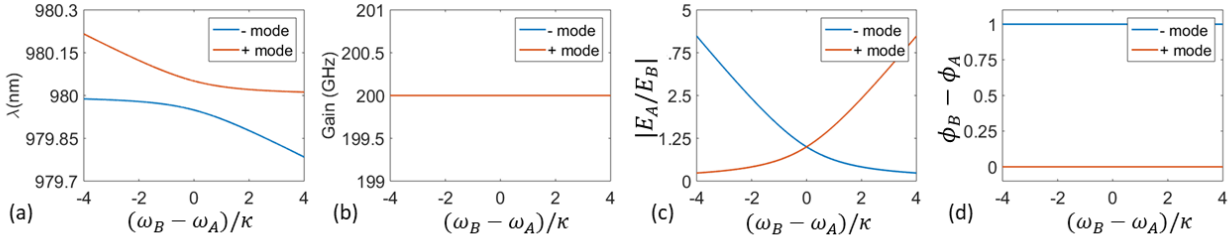

Figure 2.2: Effects of the frequency detuning on (a) wavelengths of the coupled modes; (b) gain of the coupled modes; (c) ratio of the field magnitudes in two cavities; and (d) relative phase between the fields in two cavities [17].

When the two resonators of the array have identical native resonant frequency, but experience gain contrast, i.e., $\omega_A = \omega_B, \gamma_A \neq \gamma_B$, it is found that $\bar{\bar{\mathbf{M}}}$ is non-Hermitian but PT symmetric. In this case the dependence of the coupled modes with varying gain contrast is illustrated in Figure 2.3. Notice that in Figure 2.3 there are bifurcation points at the onset of degeneracy with further variation of gain contrast [Figures 2.3(a) and (d)] or at the onset of multiple solutions from degeneracy with further gain contrast [Figures 2.3(b) and (c)]. The bifurcation points are the exceptional points at $\Delta\gamma = \pm 2\kappa$. The exceptional points separate the regimes of unbroken PT symmetry and broken PT symmetry. When $|\Delta\gamma| < 2\kappa$, the array possesses unbroken PT symmetry, meaning that both the system and the eigenmodes are PT symmetric. The unbroken-PT-symmetric eigenmodes can be written as $\bar{\mathbf{E}} = \begin{bmatrix} 1 \\ e^{i\phi} \end{bmatrix}$ with balanced intensity distribution. When $|\Delta\gamma| > 2\kappa$, the array possesses broken PT symmetry, meaning that the system is PT symmetric but its eigenmodes are not. The broken-PT-symmetric eigenmodes can be written as $\bar{\mathbf{E}} = \begin{bmatrix} 1 \\ \pm ie^{\theta} \end{bmatrix}$, with unbalanced intensity distribution and a $\pm\frac{\pi}{2}$ relative phase. If we can control $\Delta\gamma$ and increase $\Delta\gamma$ from zero, we will first be in the unbroken PT symmetry regime, where the relative phase is tuned but the relative intensity between two cavities stays balanced. As the gain contrast $\Delta\gamma$ increases further, we hit the exceptional points where the amount of relative phase tuning is at its maximum, $\pi/2$. Upon obtaining the π/2 phase tuning limit, further increase of the gain contrast results in driving the array into the PT symmetry broken regime, where the relative phase is pinned at π/2 [see Figure 2.3(d)] while the intensity distribution of the coupled modes becomes asymmetric [see Figure 2.3(c)]. Previously in the experimental characterization of coupled laser arras, it was reported that the phase tuning does not exceed the limit of ±π/2; see for example Refs. [10, 24, 28].

It has also been observed in previous experiments that the mutual coherence between the cavities decreases when the π/2 phase tuning limit is reached [10, 24]. This loss of mutual coherence can be expected as the coupled modes become asymmetric and spatially concentrate into each of the single cavities, resulting in the simultaneous lasing of both coupled modes. The distinctive feature already mentioned in Figure 2.3 is the appearance of exceptional points or branching points at $\gamma_B - \gamma_A = \pm 2\kappa$, where the two eigenmodes collapse. Because of this collapse of eigenmodes, in Figure 2.3(b) and Figure 2.3(c) the modes are not labeled as in-phase or out-of-phase to avoid confusion; unlike the case in Figure 2.4, the coupled modes cannot be traced back across the exceptional point to be identified as in-phase or out-of-phase modes.

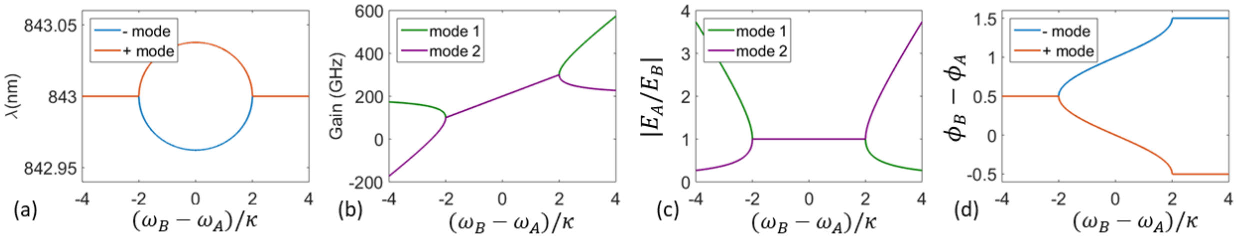

Figure 2.3: Effect of gain contrast without frequency detuning on (a) wavelengths of the coupled modes; (b) gain of the coupled modes; (c) ratio of the field magnitudes in two cavities; and (d) relative phase between the fields in two cavities [17].

When both gain contrast and frequency detuning exist, the coupled modes are controlled by the interplay between frequency detuning and gain contrast. Although this is the most complicated case, often it realistically corresponds to our VCSEL arrays analyzed in Chapter 5. In the coupled VCSEL diode arrays, both frequency detuning and simultaneously gain contrast can be driven by asymmetric current injection into the resonators of the array. If we take both the frequency detuning and the gain contrast to be linearly dependent on the injection current difference (this assumption is not accurate and will be improved in Chapter 3), the dependence of the eigenmodes in this situation are illustrated in Figure 2.4. The perfect degeneracies evident in the ideal PT-symmetric case (Figure 2.3) do not exist when frequency detuning is present. Also note that the gain of the in-phase mode is higher than the out-of-phase mode when the current injection difference is nonzero in Figure 2.4(b). This is because the change of intensity distribution of the in-phase mode, as a result of simultaneous frequency detuning and gain contrast, enhances its spatial overlap with the spatially non-uniform gain, while the intensity distribution change of the out-of-phase mode does the opposite. Whether it is the in-phase mode or out-of-phase mode that gets higher gain depends on the sign of $(\omega_A - \omega_B)(\gamma_A - \gamma_B)$. For the out-of-phase mode to have higher gain requires the local resonant frequency to increase with increasing local gain, for example if carrier induced index suppression dominates the thermal effect. It has been known that evanescently coupled VCSEL arrays tend to operate in the out-of-phase mode due to less spatial overlap with the lossy inter-element area, although for most applications the in-phase mode is preferred. The gain discrimination preference for the in-phase mode suggests that with sufficiently large current injection difference, the mode may hop from out-of-phase mode to in-phase mode, offering a novel modal control method and reconfigurability. This mode hopping behavior is observed experimentally and discussed in Ref [17]. Figure 2.4(d) also illustrates that the phase tuning limit is less than π/2. Hence to achieve the theoretical limit of π/2 phase tuning, one must minimize the frequency detuning accompanying the spatially non-uniform pumping.

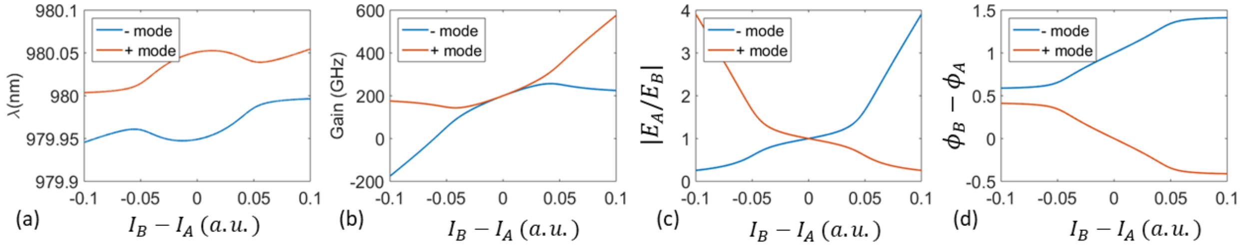

Figure 2.4: Effect of co-existing gain contrast and frequency detuning on (a) wavelengths of the coupled modes; (b) gain of the coupled modes; (c) ratio of the field magnitudes in two cavities; and (d) relative phase between the field in two cavities. It is assumed that the local changes of gain and frequency are both linearly dependent on the current difference, with $\Delta\gamma = -4\Delta\omega$, and the maximum gain contrast at the edge of the graphs are $\Delta\gamma_{max} = 4\kappa$ [17].

Using coupled mode theory with a non-Hermitian coupling matrix introduced in this section, we are able to explain the experimentally observed near-field intensity tuning, relative phase tuning, and mode hopping behavior (all discussed in Chapter 5) with a small set of parameters [17]. We have also experimentally identified PT-symmetry-breaking modes that have $\bar{\mathbf{E}} = \begin{bmatrix} 1 \\ ie^{\theta} \end{bmatrix}$, as is also discussed in Chapter 5 and Ref. [17].

2.3 Coupling matrix in evanescently coupled passive resonators

For passive resonators in the geometry of Figure 2.1, if the loss in the system is negligible (i.e., passive high-Q resonators) or if the loss is a uniform background, then the coupling coefficients are real-valued, because $\epsilon_C(x)$ and $\epsilon_{A,B}(x)$ are real and $u_{A,B}(x)$ can always be chosen to be real-valued [and they should be chosen that way so that the phase information is solely represented by the complex-valued temporally oscillating $\mathcal{E}_{A,B}(t)$]. As discussed in Appendix A, when the loss is a uniform background, we include it in the constant background conductivity σ instead of $\epsilon_C(x)$ and $\epsilon_{A,B}(x)$. When the loss/gain profile is not uniform, for example, when there exists gain-guiding, then we have complex $\epsilon_C(x)$ and $\epsilon_{A,B}(x)$. For index-guided evanescent coupling, when the amount of gain-guiding is negligible, we have real-valued $\epsilon_C(x)$ and $\epsilon_{A,B}(x)$, and the coupling coefficient is real. Furthermore, energy conservation requires that $\kappa_{AB} = \kappa_{BA}^*$ [23], which yields $\kappa_{AB} = \kappa_{BA} \equiv \kappa$ in case of real coupling coefficients. We will show next that in index-guided evanescent coupling, the coupling coefficient is also always positive.

When the two waveguides in Figure 2.1 are identical, the two normal modes of the array are either symmetrical ($\mathcal{E}_A = \mathcal{E}_B$) or anti-symmetrical ($\mathcal{E}_A = -\mathcal{E}_B$). Their frequencies are slightly different, with

$$\omega_- - \omega_+ = 2\kappa \tag{2.14}$$

where $\omega_{-,+}$ are the resonant frequencies of the anti-symmetrical and symmetrical normal modes, respectively. The anti-symmetrical mode (i.e., out-of-phase mode) has a null between the two resonators, while the symmetrical mode (i.e., in-phase mode) does not. This intuitively suggests that the anti-symmetrical mode is a higher-order normal mode, and hence it has lower effective index and higher frequency, which makes κ positive according to Equation (2.14). When it comes to index-antiguiding discussed in Section 2.5, we will see that the anti-symmetrical mode may also have one less node than the symmetrical mode, which leads to negative coupling coefficient.

To recap, the coupling coefficients in evanescently coupled passive resonators (lossless or with uniform loss) are real, positive, and symmetrical.

When the system is lossless, it is obvious that $\gamma_A = \gamma_B = 0$, and that the coupling matrix $\bar{\bar{\mathbf{M}}}$ is real and symmetrical (also Hermitian). When uniform loss exists, we have $\gamma_A = \gamma_B = \gamma < 0$. However, we can extract a common loss factor $e^{\gamma t}$ from the temporal dependence of the field amplitudes, and then $\bar{\bar{\mathbf{M}}}$ is Hermitian. Because the behavior of the coupled system is often independent of this common loss γ, it is convenient to reestablish $\bar{\bar{\mathbf{M}}}$ as Hermitian. In the scope of this dissertation, when we claim that $\bar{\bar{\mathbf{M}}}$ is Hermitian or PT-symmetric, we always allow ourselves to extract a common gain/loss factor. When non-Hermiticity is discussed, this sort of "gauge transformation" is often allowed [15, 18].

2.4 Coupling matrix in coupled lasers with gain/loss profile

From the previous section, we see that the coupling coefficients in coupled passive resonators (lossless or with uniform loss) are real, positive, and symmetrical. The coupling matrix $\bar{\bar{\mathbf{M}}}$ is real and symmetrical (also Hermitian). In this section we will see how the situation changes when we include a gain/loss profile in the coupled system. Let us first look at the various types of gain/loss situations, and how we can treat them within coupled mode theory. For details of the derivations, please refer to Appendix A.

First of all, we assume the mirror loss is spatially invariant and, as discussed in Appendix A, it is included in the theory through the spatially invariant conductivity σ. In fact, for any loss that is a constant background in the system, we include it in the constant conductivity σ (and also in the photon lifetime τ_p). Spatially invariant loss does not introduce non-Hermiticity (at least not in an interesting way), so we extract it out of the coupling matrix.

The gain/loss present in the individual cavities that result from photons interacting with the active medium will be tunable through the concentrations of electron-hole pairs injected into each cavity. In ion-implanted photonic-crystal coupled VCSEL arrays, discussed in more detail in Chapter 5 and Ref. [33], the electron-hole pairs are laterally confined in the cavity of each element and cannot cross the insulating area between the two lasers. Thus a difference in carrier concentrations will introduce non-Hermiticity through nonzero $\gamma_A - \gamma_B$. To the first-order approximation of index-guiding, the gain/loss in each cavity is approximated as uniformly distributed across the cavity mode [$u_{A,B}(x,z)$] and is included in $P_{A,B}(t)$. In other words, it is approximated that the gain/loss does not disturb the mode profile $u_{A,B}(x,z)$, but merely introduces an imaginary part in the frequency [23], which is equivalent to gain/loss being spatially uniform across each $u_{A,B}(x,z)$ (but not necessarily uniform across the composite system). Carrier densities in the individual cavities control $P_{A,B}(t)$ and $P_{A,B}(t)$, which determines $\gamma_{A,B}$. This is the main experimental control we have for tuning the coupled mode. It introduces non-Hermiticity through $i\gamma_{A,B}$, but the coupling coefficients are still real and Hermitian (i.e., $\kappa_{AB} = \kappa_{BA}$ and are both real) when the actual spatial profile of gain/loss is neglected.

For a gain/loss profile that is not uniformly distributed in the individual cavities, they are included in $\epsilon_{A,B}(x)$ and/or $\epsilon_r(x)$. This kind of gain/loss profile introduces non-Hermiticity through complex non-Hermitian coupling coefficients [34, 35]. There are two cases that introduce complex coupling coefficient, depending upon the location of the gain/loss profile. Consider gain-guiding in an individual laser. When gain-guiding becomes comparable to the index-guiding, it perturbs the individual laser mode profiles $u_{A,B}(x)$ and hence should be included in $\epsilon_{A,B}(x)$ and $\epsilon_C(x)$. The other case is any gain/loss that is in the coupling region, which may not be strong enough to perturb $u_{A,B}(x)$, but induces gain splitting between normal modes [36]. For example, loss in the coupling region typically suppresses the in-phase mode while it favors the out-of-phase mode [37], which introduces a positive imaginary part in the coupling coefficient. For this type of gain/loss, when it is weak compared to the real index profile, it could be conveniently treated by considering it only in $\epsilon_C(x)$ but not in $\epsilon_{A,B}(x)$. In the following, these two types of gain/loss that introduce complex coupling coefficient will be discussed.

Complex-valued coupling coefficients in gain-guided lasers have been studied previously [22, 38]. The evaluation of coupling coefficients can be carried out using Equation (2.4) and (2.5), with $\epsilon_C(x)$, $\epsilon_{A,B}(x)$, $u_{A,B}(x)$ all being complex-valued. The complex coupling coefficients can be understood with two intuitive interpretations. The first interpretation is through the phase delay in the wave propagation between cavities. Optical modes in gain-guided lasers have a curved phase-front [39]. (In comparison, index-guided lasers have a flat phase-front.) In other words, the optical wave propagates not only in the z-direction, but also laterally in the x-direction, and the projection of k vector in the lateral direction (k_x) has a real-valued component. (In comparison, in evanescent coupling between two index-guided lasers, k_x is purely imaginary in the coupling region between the two laser cores.) The existence of a real component in k_x in the coupling region can be interpreted as a phase delay when the electro-magnetic waves travel from one cavity to another. This phase delay can be expressed by rewriting the coupled mode equations in an equivalent form to Equations (2.2) and (2.3):

$$\dot{\mathcal{E}}_A = -i\omega_A\mathcal{E}_A + \gamma_A\mathcal{E}_A + i|\kappa_{AB}|\mathcal{E}_B(t - \tau_{AB}) \qquad (2.15a)$$

$$\dot{\mathcal{E}}_B = -i\omega_B\mathcal{E}_B + \gamma_B\mathcal{E}_B + i|\kappa_{BA}|\mathcal{E}_A(t - \tau_{BA}) \qquad (2.15b)$$

where the coupling coefficients can be entirely real and the phase angles in the coupling coefficients are absorbed to the time delays $\tau_{AB,BA}$.

The second interpretation of the complex coupling coefficient is through the gain splitting between the normal modes. When the two resonators have no detuning and no gain/loss contrast ($\omega_A = \omega_B$, $\gamma_A = \gamma_B$), the frequency splitting between the two normal modes is simply twice the coupling coefficient, as stated in Equation (2.14) for the discussion of two passive identical resonators. When there is a spatially dependent gain/loss profile in the system, the two normal modes experience different amounts of gain/loss. We express gain/loss of the normal modes as the imaginary part of the complex frequencies of the normal modes, and hence we have [36, 40, 41]

$$(\omega_- - \omega_+) + i(\gamma_- - \gamma_+) = 2\kappa = 2(\kappa_r + i\kappa_i) \tag{2.16}$$

where $\gamma_{-,+}$ are the gain/loss experienced by the anti-symmetrical and symmetrical normal modes, and κ_r and κ_i are the real and imaginary parts of the coupling coefficient. In particular, the imaginary part of the coupling coefficient represents the gain splitting between the two coupled modes

$$\kappa_i = \frac{1}{2}(\gamma_- - \gamma_+) \tag{2.17}$$

Positive κ_i means the out-of-phase mode experiences larger gain or smaller loss, while negative κ_i means that the in-phase mode is preferred. In other words, for positive (negative) κ_i, the out-of-phase (in-phase) mode would have a lower lasing threshold. We will quantitatively show this result in Chapter 3 where threshold and carrier injections are taken into consideration in the coupled rate equation analysis. This gain splitting between coupled modes plays an important role in the dynamics of the arrays as well [41], which we will also explore in Chapter 3.

The non-Hermitian coupling introduced by the gain splitting between normal modes can be illustrated with a simple model. We sketch the cross-sectional index profile of two coupled resonators in Figure 2.5. The two coupled lasers are index-guided and identical, and we introduce a small amount of loss between the two cavities. As a simple illustration, we set this loss profile to be a Dirac delta function

$$Img[\epsilon_C(x)] = \Lambda\epsilon_0\delta(x) \tag{2.18}$$

with dimensionless parameter Λ. (A positive imaginary component in $\epsilon_C(x)$ represents loss, while a negative value represents gain.) The loss is sufficiently weak and far from the waveguide cores, so that it does not perturb $u_{A,B}(x)$ from that of the lossless waveguides. From Equation (2.4) and (2.5) we obtain

$$\kappa_{AB} = \kappa_{BA} = \kappa_r + i\frac{\omega\epsilon_0\Lambda}{2}\frac{|u_A(x=0)|^2}{\langle u_A|\epsilon_A|u_A\rangle} \tag{2.19}$$

with a nonzero κ_i, proportional to the strength of the loss Λ and the intensity of the u_A (or u_B) at $x = 0$ where the loss is introduced.

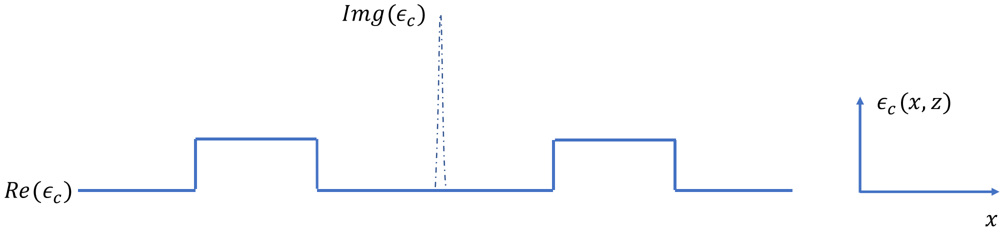

Figure 2.5: Permittivity profile of two coupled index-guided lasers with a δ-function loss in the coupling region.

Alternatively, we can calculate the gain splitting between the in-phase and out-of-phase normal modes by looking at the composite structure. The out-of-phase mode is unaffected by the $i\Lambda\epsilon_0\delta(x)$ loss because it has no intensity at $x = 0$, while the in-phase mode experiences loss that equals to γ_+. From

$$\nabla^2 E_+(x) + \frac{Re[\epsilon_C(x)]\omega^2}{c^2}E_+(x) = 0$$

$$\nabla^2 E_+(x) + \frac{Re[\epsilon_C(x)](\omega + i\gamma_+)^2}{c^2}E_+(x) = -\frac{i\Lambda\epsilon_0\delta(x)\omega^2}{c^2}E_+(x)$$

applying $\langle E_+|$ to both sides, and recognizing that $\gamma_+ \ll \omega$, we obtain

$$\gamma_+ = -\frac{\omega}{2}\frac{\langle E_+|\Lambda\epsilon_0\delta(x)|E_+\rangle}{\langle E_+|\epsilon_C|E_+\rangle} \tag{2.20}.$$

By setting $E_+(x) = u_A(x) + u_B(x)$, we can see that Equations (2.20) and (2.19) lead to an identical result:

$$\kappa_i = \frac{1}{2}(\gamma_- - \gamma_+) = \frac{\omega\epsilon_0 \Lambda}{2}\frac{|u_A(0)|^2}{\langle u_A|\epsilon_A|u_A\rangle} \quad (2.21)$$

Equation (2.21) is an illustration of how gain/loss in the coupling region introduces an imaginary component in the coupling coefficient that is proportional to the strength of gain/loss, represented by Λ in Equation (2.18). When the gain/loss is weak and/or far away from the waveguide cores, it neither perturbs the mode profiles nor introduces a curved phase front, yet it still results in an imaginary component in the coupling coefficients (i.e., non-Hermitian coupling) by splitting the gain/loss of the normal modes. The overlap-integral formula for coupling coefficient [Equations (2.4) and (2.5)] yields the same result as calculating the gain splitting between normal modes.

2.5 Coupling coefficient in index-antiguided coupling

Utilizing refractive index antiguiding to create leaky-wave coupling is a technique that has been widely studied and employed in the pursuit of high-power phase-locked semiconductor laser arrays [42-48]. However, the coupling coefficient in index-antiguided coupling is rarely discussed. While directly solving the composite structure is more accurate than using coupled mode theory, there are occasions when we cannot afford the exact solution. An example would be when we have tunable gain/loss contrast or frequency detuning between the two coupled waveguides/resonators, especially when the tuning is dynamic. This motivates us to at least qualitatively discuss the coupling coefficient for index-antiguided coupling.

Because the coupling coefficient in index-antiguided coupling is relatively unexplored, the following discussion is organized into subsections. We consider the system of two laterally coupled index-antiguided waveguides, where the spatial coupling coefficients have units of cm^{-1}, while the temporal coupling coefficients between two resonators that we have discussed in the previous sections have units of s^{-1}. The temporal coupling coefficient is simply related to the spatial coupling coefficient by

$$\kappa_{temporal} = \kappa_{spatial} v_g \qquad (2.22)$$

where v_g is the group velocity. If dispersion (as a type of nonlinearity) is not included in the model, then we can also use

$$\kappa_{temporal} = \kappa_{spatial} v_{phase} \qquad (2.22b)$$

where v_{phase} is the phase velocity. In this simple waveguide model we terminate the waveguides with mirrors to convert to optical resonators.

2.5.1 Introduction to index-antiguided coupling

Compared with evanescent optical coupling [1, 2, 49], antiguided leaky-wave coupling has several distinct features [45]: the waveguide cores have lower index than their surroundings, and thus the effective indices of the coupled modes are lower than the core material index values. Hence between the waveguide cores in the higher index region there exist leaky travelling waves with real transverse wavevectors, instead of only evanescent waves. Antiguided optical coupling has several benefits as compared to evanescent coupling. First, the coupling strength of leaky-wave coupling does not decay exponentially over distance, which means the coupling will remain strong over a much longer distance than in evanescent coupling [50-52]. Secondly, antiguided coupling at its lateral resonance condition is parallel coupling instead of nearest neighbor coupling, which, in an array with larger number of elements, maximizes the intermodal discrimination, promotes coherence across the whole array, and has graceful degradation [53, 54]. As we discuss in Subsection 2.5.3, there are design conditions where the antiguided coupling coefficient is relatively invariant against separation and refractive index variation, which relaxes fabrication tolerance. Lastly, in properly designed coupled diode laser arrays, index-antiguiding promotes stable in-phase coupled mode over the out-of-phase mode [46, 47, 55-57], and experimentally it has enabled record-high 2 W of in-phase coherent power achieved in a 20-element antiguided semiconductor laser array [56].

Recent studies involving temporal modulation of coupled arrays have shown intriguing dynamical properties when either the array elements or the coupling coefficients are under modulation. Examples include modulation bandwidth enhancement in coupled vertical cavity surface emitting laser (VCSEL) arrays [33, 58-60], indirect interband photonic transition and nonreciprocity in electrically driven coupled silicon waveguides [61], and effective magnetic field for photons and the emergence of topologically protected edge states in a resonator lattice [62]. To understand the influence of index-antiguiding on the dynamical property of coupled arrays, evaluation of the coupling coefficient is an initial step. However, the majority of the previous theoretical treatments of antiguided arrays use the exact solution of the composite waveguide, rather than coupled mode theory (CMT), so the coupling coefficient is rarely included (except for [38, 52]).

Here we analyze the coupling coefficient in a passive antiguided waveguide array [63]. We show that both the sign and magnitude of the coupling coefficient can be controlled by the distance and refractive index between the two coupled waveguide cores. We further confirm that the sign of coupling is of critical importance when the two waveguides are coherently excited [64]. The ability to reverse the sign of the coupling is illustrated by the reversal of power transfer direction in a two-section waveguide, and it opens up possibilities to synthesize more complicated behaviors in 2D coupled lattices, for example gauge transformation and topological effects [64].

Previously, the coupling coefficient in index-antiguided gain-guided waveguides has been evaluated by calculating the overlap integral between the individual waveguide modes [38, 52]. The coupled waveguide structure studied in this section is completely passive and lacks gain guiding. It is enabled by the reflecting termination boundaries [65]. We evaluate the coupling coefficients by solving the composite waveguide modes, rather than through the overlap integral between the individual waveguides. The overlap integral evaluation of coupling coefficient offers insight into the physics underpinning the sign flip of the coupling coefficient, but may give erroneous results, described in Appendix B.

The discussion next is organized as follows. Subsection 2.5.2 introduces the structure of the coupled waveguide under study and the coupled mode formalism. In Subsection 2.5.3, the analysis of coupling coefficient is presented. Subsection 2.5.4 presents the numerical study of a two-section waveguide which illustrates a reversal of the power transfer direction as a result of the sign flipping in the coupling coefficient. Appendix B describes why the overlap integral for evaluation of the coupling coefficient offers insight, but is inaccurate for passive antiguided structures.

2.5.2 Antiguided coupled waveguides

Figure 2.6 shows the transverse structure and refractive index profile of the antiguided pair of parallel waveguides that is considered. Two low-index cores are separated by a high-index spacing layer. The transverse cladding serves as a reflective termination to eliminate the radiation loss where the thickness of the edge layer is designed to maintain lateral resonance [65]. For 850 nm wavelength and the index step indicated in Figure 2.6(b), the edge layer thickness is around 1.8 μm. With reflective termination, the cores are coupled through leaky-wave coupling but the pair of waveguides considered together is not leaky, hence the eigenmodes of the array (normal modes) are guided and have no interaction with the boundary of the calculation domain. This enforces the overall system to be lossless.

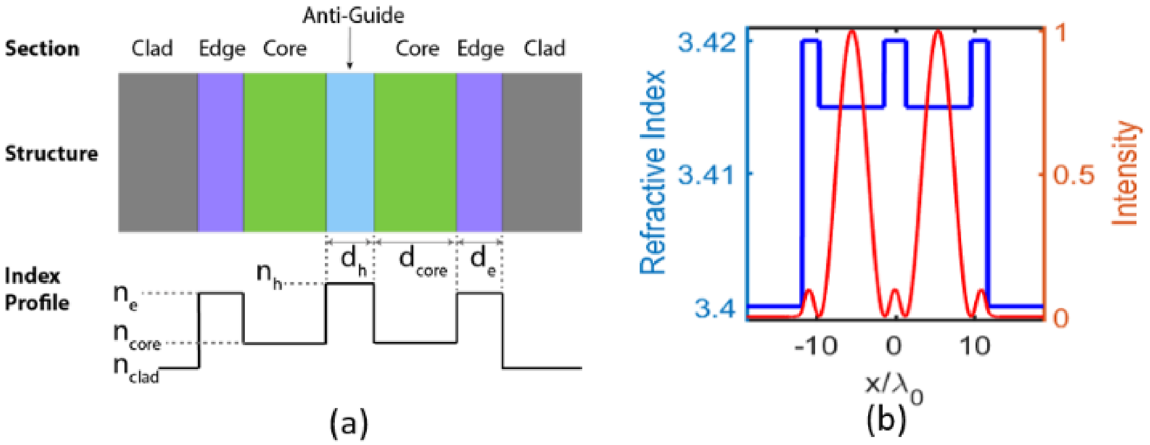

Figure 2.6: (a) Sketch and refractive index profile of an antiguided 2x1 waveguide array. (b) An example of the intensity profile of the resulting in-phase leaky-coupled mode [63].

When analyzing antiguided leaky-wave-coupled arrays without temporal modulation, an exact solution of the normal modes of the composite array structure is preferred over using coupled-mode theory, because the individual (antiguided) waveguides do not support guided modes and the coupling is strong [66]. Nonetheless, CMT can be quantitatively correct if we wisely choose the basis modes (no significant excitation to modes outside the linear space expanded by the basis modes) and it offers intuitive insight [7]. On the other hand, dynamical properties of the arrays involving stability or temporal modulation would be challenging and computationally expensive if calculated from the exact solutions. Evaluation of the coupling coefficient and its parametric dependence is essential for understanding and controlling such dynamical properties in antiguided arrays. The coupling coefficient determines the response of the array eigenmodes to frequency detuning and gain detuning. More specifically, the magnitude of the coupling coefficient determines how sensitive the systems are to the detuning, while the sign (or phase) of the coupling coefficient determines the direction of the response [17].

For simplicity, we limit our analysis to two identical waveguides with transverse-electrical (TE) polarization. We evaluate the spatial coupling coefficients (in units of cm^{-1}) through the separation of propagation constants between the two array normal modes, as

$$\kappa_{AB} = \kappa_{BA} = \kappa = \frac{\beta_{+} - \beta_{-}}{2} \tag{2.23}$$

where β_{+} (β_{-}) is the propagation constant of the symmetric (antisymmetric) normal mode. Equation (2.23) is the equivalent form of Equation (2.14) in the spatial domain. We treat κ as a signed value rather than assuming it to be positive, similar to the interpretation in Ref. [64]. The array normal modes are solved numerically using a one-dimensional (1D) finite difference frequency domain (FDFD) method [67]. For two identical waveguides, Equation (2.23) is valid in the context of both conventional power-orthogonal CMT and the more rigorous power-nonorthogonal CMT [23, 68]. For the latter, Equation (2.23) is accurate up to the second order of small cross power and self-coupling coefficients [68], meaning that the coupling coefficients extracted here are accurate even if non-orthogonal CMT with self-coupling coefficients and cross-power terms is used for dynamical analysis.

2.5.3 Evaluation of the coupling coefficient in antiguided arrays

For antiguided coupled waveguides, the modes of interest are the ones that exist in the waveguide cores (rather than in the spacing or edges) and they do not have the highest effective index (i.e., they are higher order modes). To identify these coupled modes of interest, one way is to calculate the confinement factor (intensity overlap with the core regions) and select the pair of modes with the largest confinement factors. These two modes need to also correlate with the in-phase (the electric fields in the waveguides have the same phase and hence there is an odd number of near-field fringes between the waveguides) and the out-of-phase coupled modes (the electric fields in the waveguides have a π–phase relative shift and hence there is an even number of near-field fringes between the waveguides).

In Figure 2.7(a) we plot the "dispersion" relation of the normal mode propagation constants β versus inter-element spacing thickness d_h, for the structure sketched in Figure 2.6. Shown in Figure 2.7(b) are the normal mode intensity profiles at the points labeled by (i)-(ix) in Figure 2.7(a). The pair of modes that have the minimum difference of propagation constant between them are denoted by blue and red dots in Figure 2.7(a), while black dots denote adjacent higher order normal modes. A principal result of our investigation is that we can identify the pair of coupled antiguided modes from the dispersion curves, such as shown in Figure 2.7(a). If we calculate the propagation constants of all the normal modes and look at the differences between them, the pair of coupled antiguided modes [the ones with largest confinement factors, see Figure 2.7(c)] will have the smallest difference between their propagation constants. As can be observed in Figure 2.7(a)-(c), the mode numbers corresponding to the pair of coupled modes will change with the spacing layer thickness. For example, with d_h = 1300 nm, mode 4 and 5 are the closest together along the dispersion curve and they have the largest confinement factor. For d_h = 3480 nm (5680 nm), mode 5 and 6 (6 and 7) are identified as the coupled modes for the same reason. In addition, notice that the near-field profiles of the pair of coupled modes shown in Figure 2.7(b) correspond to the in- and out-of-phase modes, as defined above.

This minimum difference of propagation constants implies that beating between the coupled modes during propagation determines the long-distance power transfer. The other modes in the array [for example the higher-order normal modes (iii), (vi), and (ix), labeled by black dots in Figure 2.7(a)] are not of practical importance, first because they have poor overlap with

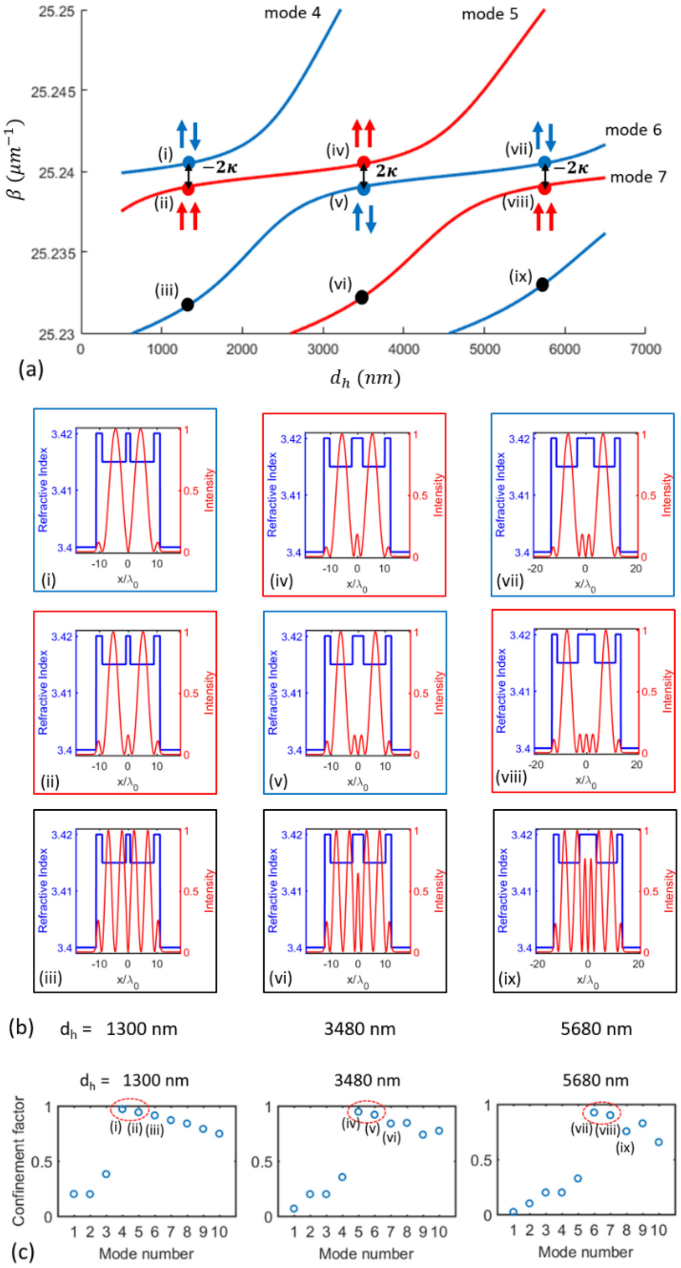

Figure 2.7: (a) Dispersion curves of the normal mode propagation constants vs. the inter-element spacing thickness d_h. In-phase (out-of-phase) coupled modes are denoted by red (blue) dots, and the sign of the coupling is indicated. (b) Mode intensity profiles at the points labeled by (i) – (ix) in the dispersion curves. (c) Confinement factor of normal modes (i.e., intensity overlap with the waveguide cores). The pairs of coupled antiguided modes (with largest confinement factor and smallest separation in β) are circled by dashed red lines. The mode numbers (1 to 10) are in the order of decreasing propagation constants. Note that mode profile (iii), (vi), and (ix) have decent confinement factors, but they are still poorly excited by Gaussian excitation due to the high-order field profile in the cores (i.e., poor field overlap with the Gaussian) [51, 63].

Gaussian excitation in the cores and hence are not excited efficiently. In addition, these modes have poor phase matching.

In Figure 2.7(a) and comparing the corresponding modes in Figure 2.7(b), note that at d_h = 1300 nm and 5680 nm, the out-of-phase mode has larger propagation constant than the in-phase one, while around 3480 nm, the in-phase mode has larger propagation constant. From Equation (2.23), this means that the sign of coupling coefficient is negative for the first case, and is positive for the latter. As we will show in Subsection 2.5.4, the sign of the coupling coefficient has no effect on the power transfer if the excitation is only in one core. However, if both cores are excited coherently, the sign of coupling coefficient determines the direction of power flow. The sign of the coupling coefficient is also important in eigenmode tuning caused by frequency or gain detuning [17].

The coupling coefficient is expected to be real in the passive structure under study, from either the power conservation point of view or from Equation (2.23) noting that both β_+ and β_- are real. The magnitude of the coupling coefficient can be taken as half of the propagation constant difference ($\Delta\beta/2$) between the closest separate modes, and the sign of coupling coefficient corresponds to whether the in-phase or the out-of-phase mode has the larger propagation constant. The coupling coefficient is thus extracted from the “dispersion curves” of Figure 2.7(a) and is plotted in Figure 2.8(a). The refractive index of the spacing layer also causes variation of the coupling coefficient in a similar manner and is plotted in Figure 2.8(b). Note the refractive index of the spacing layer could be dynamically varied in experiments, enabling dynamical control of the magnitude and sign of the coupling coefficient. Figure 2.8(a) shows that the magnitude of the coupling coefficient is quasi-periodic over the inter-element separation instead of an exponential decay that arises from evanescent coupling. Exploiting this property, it has been proposed that remote couplers can be realized [50]. We also see that around the minimum coupling points in Figure 2.8 (known as anti-resonance in [66]), the coupling coefficient, κ, is relatively invariant against variation of both the spacing layer thickness and its refractive index, making these design points attractive for fabrication tolerance.

At the local maxima of the coupling coefficient [around d_h = 2360 nm and 4560 nm in Figure 2.8(a)], the sign of κ is not well-defined, as there are three modes whose propagation constants are equally spaced. These points correspond to the lateral resonances in [66] where the intermodal discrimination is the largest, and is known to be beneficial for coherent single-mode operation of antiguided laser diode arrays. Three-mode beating occurs at these resonant conditions but they can be approximately predicted by the commonly used two-mode beating equations [69].

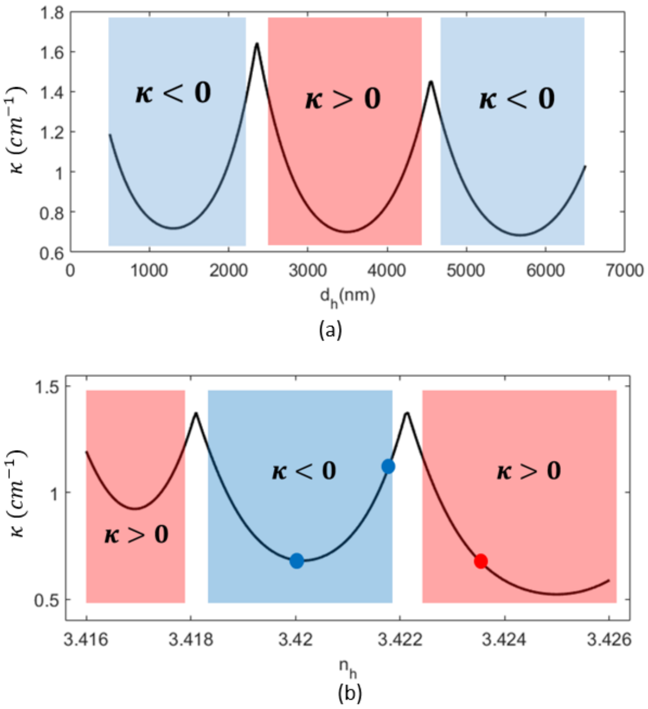

Figure 2.8: Magnitude and sign of the coupling coefficient versus inter-element spacing layer (a) thickness and (b) refractive index. Blue and red dots indicate the points that are simulated in Subsection 2.5.4 [63].

Previous studies of the coupling coefficient in antiguided structures primarily utilized the overlap integral formula derived from CMT [38, 52]. In Appendix B, we show that while the overlap integral offers an intuitive physical picture of the origin of coupling sign flipping, it is erroneous when applied to the passive antiguided structure. It produces inaccurate values of the coupling coefficient and false zero crossings that should not exist.

2.5.4 Wave propagation and reversal of the power transfer direction

Power transfer caused by the beating between two coupled modes in an antiguided leaky-wave-coupled waveguide is shown in Figure 2.9. This is the analog to evanescent coupling between parallel waveguides found in directional couplers or Mach-Zhender interferometers [70]. Wave propagation is simulated by finite element method using the commercial software COMSOL. Only the two coupled modes were included in this simulation. In practice, excitation with a Gaussian input in one waveguide core will excite additional modes, but only to a small extent [51]. We see that by tuning the index of the spacing layer, the coupling length, defined as the length for complete power transfer, can be changed. The coupling length is inversely proportional to the magnitude of coupling coefficient. Extraction of the coupling coefficient from Figure 2.9(b)-(d) is in good agreement with Figure 2.8(b). Comparing Figure 2.9(b) which has negative coupling coefficient to Figure 2.9(d) which has positive coupling coefficient, we see that the sign of coupling does not affect the power transfer if only one core is excited.

To illustrate the consequence of changing the sign of the coupling coefficient, we simulate the wave propagation in a pair of waveguides with two sections, as shown in Figure 2.10(a). The coupling coefficients in the two sections have the same magnitude but opposite sign. At the interface between the two sections in Figure 2.10(b), if there is no coupling sign change, the power transfer would continue towards the lower waveguide. But because of the

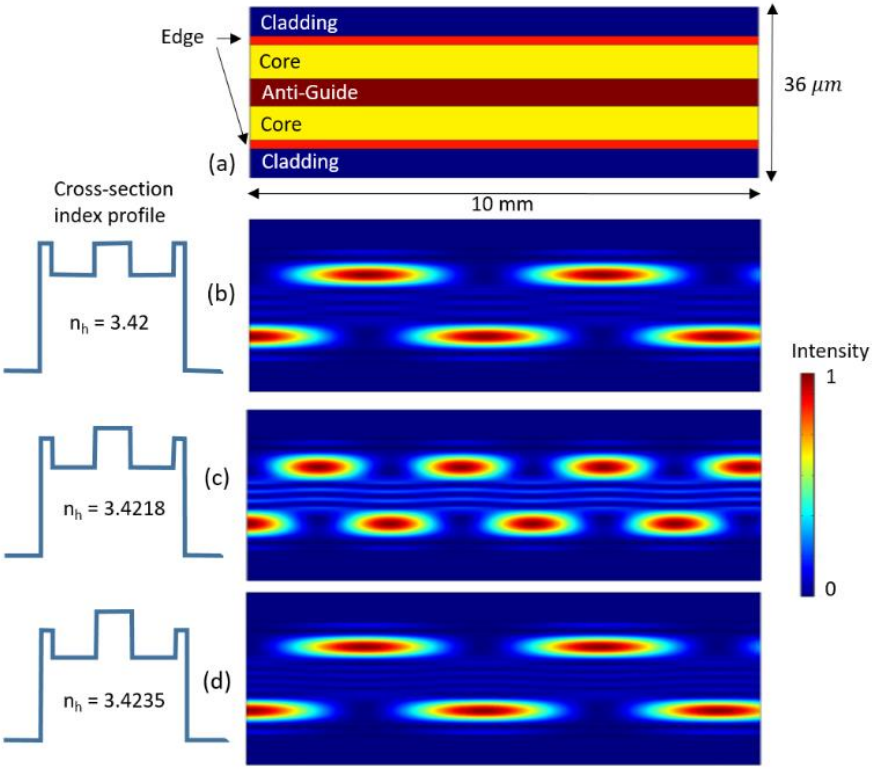

Figure 2.9: Wave propagation and power transfer in antiguided coupled waveguides. (a) Top view of the waveguide structure. (b)-(d) Electric field intensity when propagating to the right for three different antiguiding regions that result in negative [(b) and (c)] or positive [(d)] coupling coefficients. The three index profiles correspond to the three points labeled in Figure 2.8(b) [63].

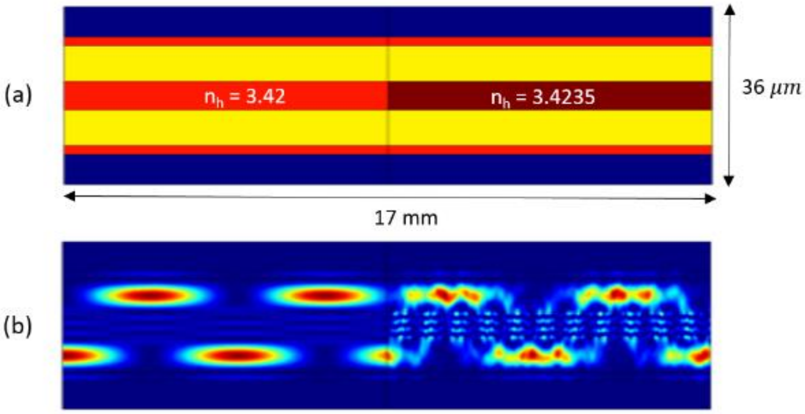

Figure 2.10: Wave propagation and power transfer showing reversal of the power transfer direction in a two-section waveguide. (a) The waveguide structure with two sections of equal κ, but opposite sign. (b) Intensity of the electric field while propagating to the right [63].

change of sign for the coupling coefficient, power is refocused back to the upper waveguide. In other words, the second section was excited by a coherent field across both ports at the interface, and the sign of coupling determines the direction of power flow. Additional modes are also excited in the second section besides the two coupled modes; however, we still see complete power transfer because the additional modes are not strongly excited and they have poor phase matching to the coupled modes.

2.5.5 Summary of index-antiguided coupling

This section has shown how the coupling coefficient between a pair of waveguides with anti-guiding coupling varies with the inter-element separation and refractive index. With increasing separation or refractive index, the magnitude of coupling coefficient varies quasi-periodically, with maxima at lateral resonances and minima at anti-resonances. The variation of the coupling coefficient is large near lateral resonances and relatively small at anti-resonances, suggesting improved fabrication tolerance around the anti-resonance points. The sign of coupling coefficient also changes each time we cross the lateral resonant conditions (κ maxima). The sign flipping can also be accomplished dynamically by varying the refractive index between waveguide cores, without the necessity of adding an auxiliary detuned waveguide as in evanescent coupling [64]. Reversal of the power transfer direction in a two-section antiguided waveguide is an interferometric verification of the coupling sign flipping. The primary disadvantage of antiguided versus evanescent coupling is the inherent multi-mode nature of the array. Coupling to other higher-order guided modes may occur in addition to the coupling between the two desired beating modes, and suppression of this coupling may be necessary to make anti-guided coupling more attractive for making directional couplers that utilize the improved fabrication tolerances.

The approach described herein for extracting the coupling coefficient could be used to study of the stability and modulation response in antiguided arrays. For more accurate modeling of the dynamical response, the use of power non-orthogonal CMT should be applied especially for asymmetrical arrays [68]. For arrays with more than two cores, the antiguided leaky-wave coupling can be either nearest neighbor or parallel coupling depending on whether the array is designed at the anti-resonant condition or resonant condition [66].

2.6 Summary

To summarize this chapter, we have shown that the coupling between two resonators can be described using coupled mode theory with a 2×2 coupling matrix $\bar{\bar{\mathbf{M}}}$. The normal modes of the array are superpositions of the individual cavity modes, and the superposition composition $\bar{\mathbf{E}}$ is the eigenvector of the coupling matrix $\bar{\bar{\mathbf{M}}}$. The complex frequencies of the normal modes (the real part being the angular frequency and the imaginary part being the gain/loss) are the eigenvalues of $\bar{\bar{\mathbf{M}}}$. The coupled array can be categorized according to the categorization of $\bar{\bar{\mathbf{M}}}$, including Hermitian, non-Hermitian, and PT-symmetric as a specific kind of non-Hermitian.

For coupled resonators without gain/loss or with constant gain/loss, $\bar{\bar{\mathbf{M}}}$ is real and symmetric (also Hermitian). The eigenvectors of $\bar{\bar{\mathbf{M}}}$ are real-valued, meaning that the relative phase between the field in the two cavities is fixed at 0 or π. The eigenvalues of $\bar{\bar{\mathbf{M}}}$ are also real-valued, meaning that the two normal modes experience no gain splitting between them. For evanescent coupling, the coupling coefficients are always real and positive, while for index-antiguided coupling, the coupling coefficients can be either positive or negative.

For two coupled resonators with non-uniform gain/loss, $\bar{\bar{\mathbf{M}}}$ is in general complex and non-Hermitian. Gain/loss contrast between the two resonators contributes to the imaginary parts of the diagonal elements in $\bar{\bar{\mathbf{M}}}$, while gain/loss splitting between the two normal modes contributes to the imaginary parts of the off-diagonal elements in $\bar{\bar{\mathbf{M}}}$ (i.e., non-Hermitian coupling). Non-Hermitian coupling manifests itself when the in-phase mode and out-of-phase mode have different lasing thresholds, evident in Chapter 3 and 4. In this chapter, we have illustrated how gain-guiding in the individual lasers or gain/loss in the coupling region induces non-Hermitian coupling.

Note that the coupled mode theory discussed in this section all belong to the conventional coupled mode theory, where self-coupling and cross-power are assumed to be negligible. When the coupling is weak and the two coupled cavities are similar, the conventional coupled mode theory functions well. But when the two coupled cavities are dissimilar or when the coupling is strong, ignoring the self-coupling and cross-power leads to inherent inconsistency regarding power conservation and reciprocity [4, 68]. This is the limitation of conventional coupled mode theory. The possibility of applying power-nonorthogonal CMT motivates future work.

2.7 References

[1] D. Marcuse, "The coupling of degenerate modes in two parallel dielectric waveguides," *Bell System Technical Journal,* vol. 50, no. 6, pp. 1791-1816, 1971.

[2] A. Yariv, "Coupled-mode theory for guided-wave optics," *IEEE Journal of Quantum Electronics,* vol. 9, no. 9, pp. 919-933, 1973.

[3] H. Haus, W. Huang, S. Kawakami, and N. Whitaker, "Coupled-mode theory of optical waveguides," *Journal of Lightwave Technology,* vol. 5, no. 1, pp. 16-23, 1987.

[4] S.-L. Chuang, "A coupled mode formulation by reciprocity and a variational principle," *Journal of Lightwave Technology,* vol. 5, no. 1, pp. 5-15, 1987.

[5] E. Kapon, J. Katz, and A. Yariv, "Supermode analysis of phase-locked arrays of semiconductor-lasers," *Optics Letters,* vol. 9, no. 4, pp. 125-127, 1984.

[6] J. K. Butler, D. E. Ackley, and D. Botez, "Coupled-mode analysis of phase-locked injection-laser arrays," *Applied Physics Letters,* vol. 44, no. 3, pp. 293-295, 1984.

[7] D. F. Siriani, P. S. Carney, and K. D. Choquette, "Coherence of leaky-mode vertical-cavity surface-emitting laser arrays," *IEEE Journal of Quantum Electronics,* vol. 47, no. 5, pp. 672-675, 2011.

[8] D. F. Siriani, K. D. Choquette, and P. S. Carney, "Stochastic coupled mode theory for partially coherent laser arrays," *J Opt Soc Am A,* vol. 27, no. 3, pp. 501-508, 2010.

[9] A. C. Lehman, J. J. Raftery, A. J. Danner, P. O. Leisher, and K. D. Choquette, "Relative phase tuning of coupled defects in photonic crystal vertical-cavity surface-emitting lasers," *Applied Physics Letters,* vol. 88, no. 2, p. 021102, 2006.

[10] M. T. Johnson, D. F. Siriani, J. D. Sulkin, and K. D. Choquette, "Phase and coherence extraction from a phased vertical cavity laser array," *Applied Physics Letters,* vol. 101, no. 3, p. 031116, 2012.

[11] M. T. Johnson, D. F. Siriani, M. P. Tan, and K. D. Choquette, "Beam steering via resonance detuning in coherently coupled vertical cavity laser arrays," *Applied Physics Letters,* vol. 103, no. 20, p. 201115, 2013.

[12] C. M. Bender and S. Boettcher, "Real spectra in non-Hermitian Hamiltonians having PT symmetry," *Physical Review Letters,* vol. 80, no. 24, pp. 5243-5246, 1998.

[13] M. Liertzer, L. Ge, A. Cerjan, A. D. Stone, H. E. Tureci, and S. Rotter, "Pump-induced exceptional points in lasers," *Phys Rev Lett,* vol. 108, no. 17, p. 173901, 2012.

[14] R. El-Ganainy, M. Khajavikhan, and L. Ge, "Exceptional points and lasing self-termination in photonic molecules," *Physical Review A,* vol. 90, no. 1, pp. 013802-013802, 2014.

[15] H. Hodaei, M. A. Miri, M. Heinrich, D. N. Christodoulides, and M. Khajavikhan, "Parity-time-symmetric microring lasers," *Science,* vol. 346, no. 6212, pp. 975-978, 2014.

[16] L. Chang *et al.*, "Parity–time symmetry and variable optical isolation in active–passive-coupled microresonators," *Nature Photonics,* vol. 8, no. 7, pp. 524-529, 2014.

[17] Z. Gao, S. T. Fryslie, B. J. Thompson, P. S. Carney, and K. D. Choquette, "Parity-time symmetry in coherently coupled vertical cavity laser arrays," *Optica,* vol. 4, no. 3, pp. 323-329, 2017.

[18] A. Guo *et al.*, "Observation of PT-symmetry breaking in complex optical potentials," *Phys Rev Lett,* vol. 103, no. 9, p. 093902, 2009.

[19] B. Peng *et al.*, "Parity-time-symmetric whispering-gallery microcavities," *Nature Physics,* vol. 10, no. 5, pp. 394-398, 2014.

[20] W. Chen, S. Kaya Ozdemir, G. Zhao, J. Wiersig, and L. Yang, "Exceptional points enhance sensing in an optical microcavity," *Nature,* vol. 548, no. 7666, pp. 192-196, 2017.

[21] H. Hodaei *et al.*, "Enhanced sensitivity at higher-order exceptional points," *Nature,* vol. 548, no. 7666, pp. 187-191, 2017.

[22] J. Katz, E. Kapon, C. Lindsey, S. Margalit, and A. Yariv, "Coupling coefficient of gain-guided lasers," *Applied Optics,* vol. 23, no. 14, pp. 2231-2233, 1984.

[23] S. L. Chuang, *Physics of Photonic Devices*, 2nd ed. (Wiley series in pure and applied optics). Hoboken, N.J.: John Wiley & Sons, 2009.

[24] A. C. Lehman, J. J. Raftery, P. S. Carney, and K. D. Choquette, "Coherence of photonic crystal vertical-cavity surface-emitting laser arrays," *IEEE Journal of Quantum Electronics,* vol. 43, no. 1, pp. 25-30, 2007.

[25] E. Kapon, J. Katz, S. Margalit, and A. Yariv, "Longitudinal-mode control in integrated semiconductor-laser phased-arrays by phase-velocity matching," *Applied Physics Letters,* vol. 44, no. 2, pp. 157-159, 1984.

[26] G. H. B. Thompson, "Analysis of optical directional-couplers that include gain or loss and their application to semiconductor slab dielectric guides," *Journal of Lightwave Technology,* vol. 4, no. 11, pp. 1678-1693, 1986.

[27] C. E. Ruter, K. G. Makris, R. El-Ganainy, D. N. Christodoulides, M. Segev, and D. Kip, "Observation of parity-time symmetry in optics," *Nature Physics,* vol. 6, no. 3, pp. 192-195, 2010.

[28] E. Kapon, Z. Rav-Noy, L. T. Lu, M. Yi, S. Margalit, and A. Yariv, "Phase-locking characteristics of coupled ridge-waveguide InP/InGaAsP diode lasers," *Applied Physics Letters,* vol. 45, no. 11, pp. 1159-1161, 1984.

[29] L. D. A. Lundeberg and E. Kapon, "Mode switching and beam steering in photonic crystal heterostructures implemented with vertical-cavity surface-emitting lasers," *Applied Physics Letters,* vol. 90, no. 24, pp. 2005-2008, 2007.

[30] J. Doppler *et al.*, "Dynamically encircling an exceptional point for asymmetric mode switching," *Nature,* vol. 537, no. 7618, pp. 76-79, 2016.

[31] C. M. Bender, M. V. Berry, and A. Mandilara, "Generalized PT symmetry and real spectra," *Journal of Physics A-Mathematical and General,* vol. 35, no. 31, pp. L467-L471, 2002.

[32] H. A. Haus, *Waves and Fields in Optoelectronics* (Prentice-Hall series in solid state physical electronics). Englewood Cliffs, NJ: Prentice-Hall, 1984

[33] S. T. M. Fryslie *et al.*, "Modulation of coherently coupled phased photonic crystal vertical cavity laser arrays," *IEEE Journal of Selected Topics in Quantum Electronics,* vol. 23, no. 6, pp. 1-9, 2017.

[34] Z. Gao *et al.*, "Non-Hermitian aspects of coherently coupled vertical cavity laser arrays," in *CLEO: Science and Innovations*, 2017, p. SW1C. 4: Optical Society of America.

[35] S. Longhi and L. Feng, "Non-Hermitian laser phase locking," *arXiv preprint arXiv:1802.05439,* 2018.

[36] K. A. Atlasov, K. F. Karlsson, A. Rudra, B. Dwir, and E. Kapon, "Wavelength and loss splitting in directly coupled photonic-crystal defect microcavities," *Optics Express,* vol. 16, no. 20, pp. 16255-16264, 2008.

[37] D. Botez and J. C. Connolly, "Higg-power phase-locked arrays of index-guided diode lasers," *Applied Physics Letters,* vol. 43, no. 12, pp. 1096-1098, 1983.

[38] M. J. Adams, N. Li, B. R. Cemlyn, H. Susanto, and I. D. Henning, "Effects of detuning, gain-guiding, and index antiguiding on the dynamics of two laterally coupled semiconductor lasers," *Physical Review A,* vol. 95, no. 5, p. 053869, 2017.

[39] D. D. Cook and F. R. Nash, "Gain-induced guiding and astigmatic output beam of GaAs lasers," *Journal of Applied Physics,* vol. 46, no. 4, pp. 1660-1672, 1975.

[40] J. K. Butler, D. E. Ackley, and M. Ettenberg, "Coupled-mode analysis of gain and wavelength oscillation characteristics of diode-laser phased-arrays," *IEEE Journal of Quantum Electronics,* vol. 21, no. 5, pp. 458-464, 1985.

[41] H. G. Winful, S. Allen, and L. Rahman, "Validity of the coupled-oscillator model for laser-array dynamics," *Optics Letters,* vol. 18, no. 21, pp. 1810-1812, 1993.

[42] D. E. Ackley and R. W. H. Engelmann, "High-power leaky-mode multiple-stripe laser," *Applied Physics Letters,* vol. 39, no. 1, pp. 27-29, 1981.

[43] D. Botez and G. Peterson, "Modes of phase-locked diode-laser arrays of closely spaced antiguides," *Electronics Letters,* vol. 24, no. 16, pp. 1042-1044, 1988.

[44] G. R. Hadley, "Index-guided arrays with a large index step," *Opt Lett*, vol. 14, no. 6, pp. 308-10, 1989.

[45] D. Botez, “Monolithic phase-locked semiconductor laser arrays,” in *Diode Laser Arrays*, D. Botez and D. R. Scifres, Ed. New York: Cambridge University Press, 1994, pp. 1-72.

[46] L. J. Mawst *et al.*, "Two-dimensional surface-emitting leaky-wave coupled laser arrays," *IEEE Journal of Quantum Electronics*, vol. 29, no. 6, pp. 1906-1917, 1993.

[47] D. F. Siriani and K. D. Choquette, "Implant defined anti-guided vertical-cavity surface-emitting laser arrays," *IEEE Journal of Quantum Electronics*, vol. 47, no. 2, pp. 160-164, 2011.

[48] D. F. Siriani and K. D. Choquette, "Coherent coupling of vertical-cavity surface-emitting laser arrays," in *Advances in Semiconductor Lasers*, vol. 861 ed.: Elsevier Inc., 2012, pp. 227-267.

[49] E. A. Marcatili, "Dielectric rectangular waveguide and directional coupler for integrated optics," *Bell System Technical Journal*, vol. 48, no. 7, pp. 2071-2102, 1969.

[50] M. Mann, U. Trutschel, C. Wachter, L. Leine, and F. Lederer, "Directional coupler based on an antiresonant reflecting optical waveguide," *Opt Lett*, vol. 16, no. 11, pp. 805-807, 1991.

[51] C. H. Lai and C. I. Hsieh, "Power coupling between gain-guided index-antiguided planar waveguides," *Opt Express*, vol. 24, no. 24, pp. 28026-28038, 2016.

[52] X. R. Wang, C. D. Xiong, and J. Y. Luo, "Coupling coefficients evaluation of a directional coupler using gain guided and index antiguided fibers," *Optics Communications*, vol. 282, no. 3, pp. 382-386, 2009.

[53] W. J. Fader and G. E. Palma, "Normal modes of N coupled lasers," *Opt Lett*, vol. 10, no. 8, pp. 381-3, 1985.

[54] D. Botez and L. J. Mawst, "Phase-locked laser arrays revisited," *IEEE Circuits and Devices Magazine*, vol. 12, no. 6, pp. 25-32, 1996.

[55] D. Botez, L. Mawst, P. Hayashida, G. Peterson, and T. J. Roth, "High-power, diffraction-limited-beam operation from phase-locked diode-laser arrays of closely spaced ‘leaky’ waveguides (antiguides)," *Applied Physics Letters*, vol. 53, no. 6, pp. 464-466, 1988.

[56] L. J. Mawst *et al.*, "Resonant self-aligned-stripe antiguided diode-laser array," *Applied Physics Letters*, vol. 60, no. 6, pp. 668-670, 1992.

[57] Z. Gao, B. J. Thompson, G. Ragunathan, M. T. Johnson, B. Rout, and K. D. Choquette, "Bottom-emitting coherently coupled vertical cavity laser arrays," *IEEE Photonics Technology Letters*, vol. 28, no. 4, pp. 513-515, 2016.

[58] H. Dalir and F. Koyama, "29 GHz directly modulated 980 nm vertical-cavity surface emitting lasers with bow-tie shape transverse coupled cavity," *Applied Physics Letters*, vol. 103, no. 9, p. 091109, 2013.

[59] S. T. M. Fryslie, M. P. Tan, D. F. Siriani, M. T. Johnson, and K. D. Choquette, "37-Ghz modulation via resonance tuning in single-mode coherent vertical-cavity laser arrays," *IEEE Photonics Technology Letters*, vol. 27, no. 4, pp. 415-418, 2015.

[60] X. D. Gu, M. Nakahama, A. Matsutani, M. Ahmed, A. Bakry, and F. Koyama, "850 nm transverse-coupled-cavity vertical-cavity surface-emitting laser with direct modulation bandwidth of over 30 GHz," *Applied Physics Express*, vol. 8, no. 8, p. 082702, 2015.

[61] H. Lira, Z. Yu, S. Fan, and M. Lipson, "Electrically driven nonreciprocity induced by interband photonic transition on a silicon chip," *Phys Rev Lett*, vol. 109, no. 3, p. 033901, 2012.

[62] K. J. Fang, Z. F. Yu, and S. H. Fan, "Realizing effective magnetic field for photons by controlling the phase of dynamic modulation," *Nature Photonics,* vol. 6, no. 11, pp. 782-787, 2012.

[63] Z. Gao, D. Siriani, and K. D. Choquette, "Coupling coefficient in antiguided coupling: magnitude and sign control," *J Opt Soc Am B,* vol. 35, no. 2, pp. 417-422, 2018.

[64] R. Keil *et al.*, "Universal sign control of coupling in tight-binding lattices," *Phys Rev Lett*, vol. 116, no. 21, p. 213901, 2016.

[65] D. F. Siriani and K. D. Choquette, "Reduced loss and improved mode discrimination in resonant optical waveguide arrays," *Electronics Letters,* vol. 48, no. 10, pp. 591-592, 2012.

[66] D. Botez, L. J. Mawst, G. L. Peterson, and T. J. Roth, "Phase-locked arrays of antiguides: modal content and discrimination," *IEEE Journal of Quantum Electronics,* vol. 26, no. 3, pp. 482-495, 1990.

[67] L. A. Coldren, S. W. Corzine, and M. L. Mashanovitch, *Diode Lasers and Photonic Integrated Circuits*. John Wiley & Sons, 2012.

[68] W.-P. Huang, "Coupled-mode theory for optical waveguides: an overview," *J Opt Soc Am A,* vol. 11, no. 3, pp. 963-983, 1994.

[69] C. H. Lai, C. K. Sun, and H. C. Chang, "Terahertz antiresonant-reflecting-hollow-waveguide-based directional coupler operating at antiresonant frequencies," *Opt Lett,* vol. 36, no. 18, pp. 3590-2, 2011.

[70] R. G. Hunsperger, *Integrated Optics, Theory and Technology*, 2nd ed. (Springer series in optical sciences, no. 33). Berlin ; New York: Springer-Verlag, 1984

CHAPTER 3: COUPLED RATE EQUATION ANALYSIS: THE STEADY-STATE SOLUTIONS

Coupled mode theory (CMT), discussed in Chapter 2, has been well developed to describe the coupled optical modes and the mutual coherence in coupled laser arrays [1-5]. However, to determine the coupled mode from CMT it requires knowledge of the frequency detuning $\Delta\omega$ and the gain contrast $\Delta\gamma$ between cavities, which are challenging to measure and are not directly controlled in coupled diode laser arrays. To overcome this challenge, we have developed and adopted coupled rate equation (CRE) analysis, which takes the carrier injection rates and the *cavity frequency detuning* (different from the total frequency detuning $\Delta\omega$) as independent variables. CRE analysis combines the coupled mode theory with the standard semiconductor laser rate equations, and has been used for the study of temporal dynamics of optically coupled semiconductor laser arrays [6, 7]. In addition to capturing the temporal dynamics, the CRE analysis also incorporates carrier-induced nonlinearities [8, 9], for example, the gain saturation and the amplitude-phase coupling (i.e., nonzero linewidth enhancement factor resulting from carrier-induced frequency shift) [6, 10]. In this chapter, we will show that these nonlinearities are critical not only for temporal dynamics, but also for the control of steady-state coupled modes. By solving the steady-state coupled rate equations (SSCREs), we can elucidate the control mechanism for the array normal modes (both the intensity profile and the relative phase between cavities). We show for the first time that the control mechanism is governed by the carrier-induced nonlinearities, and the inclusion of carrier densities is thus crucial in our analysis.

The phase tuning mechanism in optically coupled semiconductor lasers has been a question of longstanding interest [11-15]. In the case of a real-valued coupling coefficient (for example arising from passive evanescent coupling), coupled mode theory predicts that the gain contrast between lasers causes phase tuning, while the frequency detuning between cavities results in asymmetrical intensity distribution (see Chapter 2 Section 2.2 and Ref. [11, 15, 16]). On the other hand, previous CRE analysis concluded precisely the opposite in that frequency detuning was found to cause phase variation but has negligible effect on intensity distribution [7, 14]. The latter is also in agreement with experimental observations suggesting that the frequency detuning causes the relative phase tuning [17]. In this chapter, by carefully accounting for the cavity detuning and the total frequency detuning, we show that the two perspectives, in fact, do not contradict. We define the *cavity frequency detuning* $\Delta\Omega$ to be the frequency detuning that excludes the contribution from the amplitude-phase coupling, and we define the total frequency detuning $\Delta\omega$ to be the detuning that includes the amplitude-phase coupling, which is dependent on the actual carrier density distribution in the array. We show that clearly distinguishing $\Delta\Omega$ from $\Delta\omega$ is important in understanding coupled semiconductor lasers, and is the key to maintaining consistency between CMT and CRE analysis.

In this chapter we also apply our CRE analysis to parity-time (PT) symmetry and exceptional points in this optically coupled non-Hermitian system. When the laser array has a non-Hermitian coupling matrix $\bar{\bar{\mathbf{M}}}$, we say the array is non-Hermitian, in the sense of non-Hermitian coupled mode theory or non-Hermitian effective Hamiltonian in a photonic dimer (see Chapter 2 Section 2.2 and [15, 18-20]). Comparing with previous PT symmetry analysis where gain saturation and frequency perturbation have also been considered [21-25], we show that the amplitude-phase coupling is another nonlinearity that can play a critical role in optically coupled semiconductor lasers in the weak coupling regime. As an addition to the well-known pump-induced PT symmetry breaking and exceptional points [18, 21], we demonstrate PT symmetry breaking induced exclusively by cavity detuning, as well as exceptional points induced by judiciously combining unequal pumping and cavity detuning. For exceptional points, herein we are referring to the points where the two optical modes collapse [26, 27], although the concept of exceptional points can also be extended to other eigenvalue problems [9].

3.1 Coupled rate equations

Assuming the two lasers in the array are similar (i.e., they are identical except the frequency detuning and different carrier injection rates), the coupled rate equations (CREs) can be written as [6, 7]

$$\frac{dE_A}{dt} = \frac{1}{2}\Gamma v_g a_{\mathrm{diff}}(N_A - N_{th})(1 - i\alpha_H)E_A + i(\omega - \Omega_A)E_A + i\kappa E_B \tag{3.1}$$

$$\frac{dE_B}{dt} = \frac{1}{2}\Gamma v_g a_{\mathrm{diff}}(N_B - N_{th})(1 - i\alpha_H)E_B + i(\omega - \Omega_B)E_B + i\kappa E_A \tag{3.2}$$

$$\frac{dN_{A,B}}{dt} = P_{A,B} - \frac{N_{A,B}}{\tau_N} - v_g\left[g_{th} + a_{diff}\left(N_{A,B} - N_{th}\right)\right]\left|E_{A,B}\right|^2 \tag{3.3}$$

where Γ is the confinement factor, v_g the group velocity, a_{diff} the differential gain, N_{th} is the threshold carrier density when the lasers are isolated (same for A and B), α_H the linewidth enhancement factor, ω the frequency of the optical mode (the normal mode), $N_{A,B}$ the carrier densities in cavity A and B respectively. $E_{A,B}(t)$ are the slowly varying envelopes of the electric fields in cavity A and B. [The total electric field in the composite system is $\mathcal{E}_{tot}(x,z,t) = u_A(x,z)E_A(t)e^{-i\omega t} + u_B(x,z)E_B(t)e^{-i\omega t}$. We normalize $u_{A,B}$ so that $\left|E_{A,B}\right|^2$ are the photon densities with units of cm^{-3}.] $\Omega_{A,B}$ are the cavity resonant frequencies of the individual lasers when they are isolated and when their carrier densities are pinned at the threshold value (i.e., $N_{A,B} = N_{th}$). This definition of $\Omega_{A,B}$ may seem particular, but it is very important to recognize that the actual cavity resonant frequencies (we denote as $\omega_{A,B}$) are dependent on the local carrier densities in the cavities. κ is the coupling coefficient, and based on the assumption that the two lasers are almost identical, we have also assumed the coupling coefficients to be symmetrical (i.e., $\kappa_{AB} = \kappa_{BA} = \kappa$).

Equations (3.1)-(3.2) are equivalent to the coupled mode equations (2.2) and (2.3) in chapter 2 if we recognize [28]:

$$\mathcal{E}_{A,B}(t) = E_{A,B}(t)e^{-i\omega t} \tag{3.4}$$

$$\gamma_{A,B} = \frac{1}{2}\Gamma v_g a_{\text{diff}}\left(N_{A,B} - N_{th}\right) \tag{3.5}$$

$$\omega_{A,B} = \Omega_{A,B} + \alpha_H \gamma_{A,B} \tag{3.6}$$

Equation (3.6) describes the total frequency shift which includes the contribution from the carrier density variation (and hence variations in $\gamma_{A,B}$), which is an important nonlinearity in semiconductor lasers, often called the amplitude-phase coupling [6, 10]. When the lasers are isolated, we always have $\gamma_{A,B} = 0$ and $\omega_{A,B} = \Omega_{A,B}$, because of the gain pinning (modal gain always balances modal loss in steady state, resulting in zero net gain). However, in coupled laser arrays, because of the energy transfer between the lasers through optical coupling (to be discussed below), we often have $\gamma_{A,B} \neq 0$ and $\omega_{A,B} \neq \Omega_{A,B}$. Note that although we often control $\Omega_{A,B}$ through external parameters (temperature, cavity design, etc.), we do not have direct control over the carrier densities, hence $\omega_{A,B}$ are often not directly controlled.

Equation (3.3) describes the carrier density dynamics, where τ_N is the carrier lifetime, g_{th} is the threshold gain, $P_{A,B}$ are the carrier injection rates, which are proportional to the injection currents $I_{A,B}$ [28]:

$$P_{A,B} = \eta_i \frac{I_{A,B}}{qV} \tag{3.7}$$

where η_i is the carrier injection efficiency, q is the elementary electron charge, V is the volume of active region.

To connect better with the experimental parameters, we also point out the threshold condition regarding device and material parameters [28]:

$$v_g \Gamma g_{th} = \frac{1}{\tau_p} = \frac{\omega}{Q} = v_g \Gamma a_{diff} (N_{th} - N_{tr}) \tag{3.8}$$

where τ_p is the photon lifetime, Q is the cavity quality factor, N_{tr} is the material transparency carrier density (defined as when stimulated emission balances stimulated absorption).

The CREs can be written in a more elegant manner if we define dimensionless (rescaled) variables [6, 7]. We have followed the rescaling used in [7], which defines the normalized carrier densities $M_{A,B}$, pump rates $Q_{A,B}$, and field magnitudes $Y_{A,B}$ as:

$$M_{A,B} \equiv 1 + v_g \Gamma a_{\text{diff}} \tau_p \left(N_{A,B} - N_{th} \right) \tag{3.9}$$

$$Q_{A,B} \equiv C_Q \left(\frac{I_{A,B}}{I_{th}} - 1 \right) + \frac{I_{A,B}}{I_{th}} \tag{3.10}$$

$$Y_{A,B} \equiv \sqrt{v_g \, a_{\text{diff}} \tau_N} \left| E_{A,B} \right| \tag{3.11}$$

where $I_{A,B}$ are the injected currents, I_{th} is the threshold current (same for A and B), C_Q is the constant relating the injected currents to the normalized pump parameters, defined as $C_Q \equiv \frac{a_{\text{diff}} N_{tr}}{g_{th}}$. The normalized parameters have very intuitive scales: their values at transparency and threshold conditions are simply $M_{A,Btr} = 0$, $M_{A,Bth} = 1$, $Q_{A,Btr} = 0$, $Q_{A,Bth} = 1$, where the subscript tr denotes transparency and th denotes threshold.

The coupled rate equations are now written in the rescaled variables as

$$\frac{dY_A}{dt} = \frac{1}{2\tau_p} (M_A - 1) Y_A - (\kappa_r sin\phi + \kappa_i \cos\phi) Y_B \tag{3.12}$$

$$\frac{dY_B}{dt} = \frac{1}{2\tau_p}(M_B - 1)Y_B + (\kappa_r sin\phi - \kappa_i \cos\phi)Y_A \tag{3.13}$$

$$\frac{d\phi}{dt} = \frac{\alpha_H}{2\tau_p}(M_A - M_B) - \Delta\Omega + \kappa_r cos\phi\left(\frac{Y_A}{Y_B} - \frac{Y_B}{Y_A}\right) + \kappa_i sin\phi\left(\frac{Y_A}{Y_B} + \frac{Y_B}{Y_A}\right) \tag{3.14}$$

$$\frac{dM_{A,B}}{dt} = \frac{1}{\tau_N}\left[Q_{A,B} - M_{A,B}\left(1 + Y_{A,B}^2\right)\right] \tag{3.15}$$

In addition to using the rescaled variables, we have also defined $\phi \equiv \phi_B - \phi_A$, $\Delta\Omega \equiv \Omega_{\mathrm{B}} - \Omega_A$, $\kappa = \kappa_r + i\kappa_i$. All variables are real-valued in Equations (3.12)-(3.15). We have dropped the global phase and have kept only the relative phase ϕ, as the global phase can be arbitrarily defined. The detailed derivation from the original coupled rate equations in complex-valued physical variables [Equations (3.1)-(3.3)] to the rescaled and real-valued dimensionless variables [Equations (3.12)-(3.15)] is presented in Appendix A or in Ref. [7].

As an aside for the benefit of readers, we also want to point out that there is another rescaling approach that has been previously used, for example in Refs. [6, 8, 9, 14], where the rescaled variables are excess pumping rate P, excess carrier density Z, electric field amplitude X. Compared with the normalization adopted in this chapter, the transformation is:

$$\begin{cases} X = \frac{Y}{\sqrt{2}} \\ P = \frac{Q-1}{2} \\ Z = \frac{M-1}{2\Omega} \\ \eta = \kappa\tau_p \end{cases} \tag{3.16}$$

where $\Omega \equiv \sqrt{2P\frac{\tau_p}{\tau_N}}$. Equations (3.16) are valuable if comparing results between papers in the literature.

3.2 Weakly coupled semiconductor laser arrays: the qualitative description

Unlike the case of a single isolated laser, where its steady-state carrier density above threshold is pinned at the threshold value N_{th}, the carrier densities in each coupled laser in the array can be different from N_{th}. For example, one laser may have its carrier density higher than N_{th}, while the other laser has lower than N_{th}. In other words, the total carrier density and the gain of the normal mode are expected to be pinned at lasing threshold, but the local carrier densities $N_{A,B}$ and the local gain $\gamma_{A,B}$ do not necessarily pin. Because of the amplitude-phase coupling (see Equation 3.6), the difference in carrier densities or the difference of gain between cavities ($N_B - N_A$, or $\gamma_B - \gamma_A$) will also contribute to the total frequency detuning:

$$\Delta\omega \equiv \omega_B - \omega_A = \Delta\Omega + \alpha_H \Delta\gamma \tag{3.17}$$

All frequency tuning mechanisms (e.g. thermal tuning of the cavity index) are included in $\mathit{\Omega}_{A,B}$, except for the amplitude-phase coupling. Amplitude-phase coupling is separately treated in Equation (3.17) by the term $\alpha_H \Delta\gamma$. By adopting this definition, all the externally controllable frequency tuning mechanisms are included in $\Delta\Omega$. When the lasers are not coupled, $\Omega_{A,B}$ and $\omega_{A,B}$ are always the same because of gain (carrier density) pinning. But when the lasers are optically coupled, $\Omega_{A,B}$ and $\omega_{A,B}$ will be different. When the lasers are optically coupled, we can still vary $\Omega_{A,B}$ with thermal index tuning for example, but $\omega_{A,B}$ will differ from $\Omega_{A,B}$, because the laser array has the freedom of redistributing its carrier densities through photon-mediated energy transfer between elements as discussed later.

Setting the time derivatives in Equations (3.12) – (3.15) to zero, we get SSCREs, which are five algebraic equations with five real-valued unknowns ($Y_{A,B}, \phi, M_{A,B}$). We consider the pump parameters $Q_{A,B}$ and the cavity detuning $\Delta\Omega$ to be experimentally controlled and measurable. The terms $Q_{A,B}$ are directly related to the injected currents through Equation (3.10), and $\Delta\Omega$ can be measured by extrapolating the frequency shift in the uncoupled region [14, 29], illustrated in Figure 3.1.

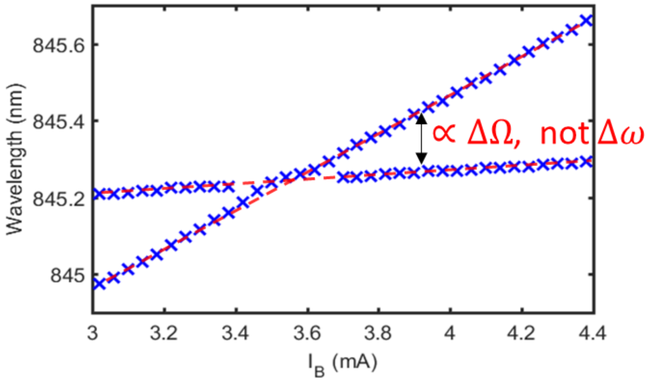

Figure 3.1: Wavelength control by current tuning (I_B was being tuned, I_A was fixed). Blue crosses are data points and the red dashed line is extrapolation of the data points. Inside the coupling region (roughly when there is only a single spectral peak), extrapolation gives us $\Delta\Omega$, but not $\Delta\omega$.

The notional relationship between the coupled mode theory and the coupled rate equations is illustrated in the drawing as Figure 3.2. In CMT, the input variables are $\Delta\omega$ and $\Delta\gamma$. Assuming real-valued κ, CMT says that $\Delta\omega$ controls the intensity distribution and $\Delta\gamma$ controls the relative phase. In coupled rate equations, the input variables are $Q_{A,B}$ and $\Delta\Omega$. How they control the coupled mode depends on the strength of the coupling coefficient, as discussed in the following section. In CRE analysis, nonlinearities in the system are included (shown by the orange arrows in Figure 3.2), and they turn out to have critical roles in the mode control. The two theories are consistent, where CMT can be thought of as the core of CRE analysis.

In general, there are no analytical solutions to the SSCREs when we consider the pump rates $Q_{A,B}$ and the cavity detuning $\Delta\Omega$ as input parameters and solve for $(Y_{A,B}, \phi, M_{A,B})$, because transcendental equations are involved [8]. Approximate analytical solutions to the SSCREs can be found for equal pumping ($Q_A = Q_B$) assuming very weak coupling ($|\kappa| \ll 1/\tau_p$), as reported in Ref. [7]. However, in coupled lasers with coupling coefficient comparable to the cavity loss

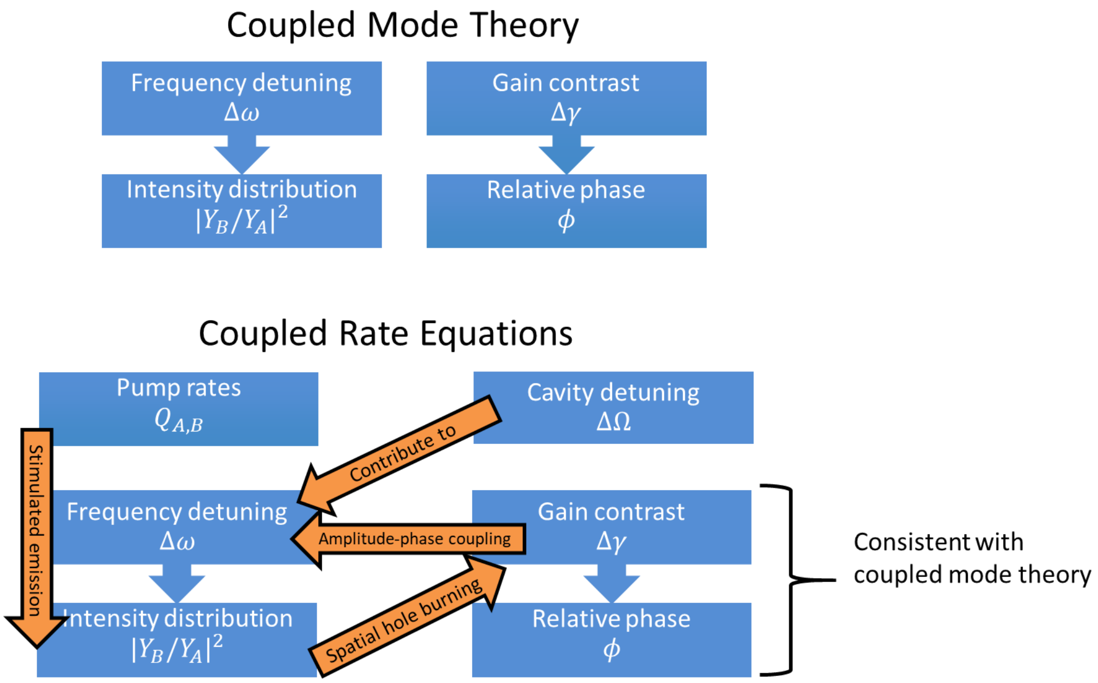

Figure 3.2: Illustration of how coupled rate equations relate to the coupled mode theory (real-valued κ is assumed).

rate, which is the case for VCSEL arrays [14, 30], this approximation is not valid. Numerical root search is used when analytical solutions are not available. In addition to solving for the coupled optical modes, we also examine the tuning mechanism by calculating the gain contrast $\Delta\gamma$ and the total frequency detuning $\Delta\omega$ between cavities. They are related to the carrier density distribution through the following equations:

$$\Delta\gamma \equiv \gamma_B - \gamma_A = \frac{M_B - M_A}{2\tau_p} \tag{3.18}$$

$$\Delta\omega \equiv \omega_B - \omega_A = \Delta\Omega + \frac{\alpha_H}{2\tau_p}(\mathrm{M_B} - \mathrm{M_A}) \tag{3.19}$$

The device parameters used in this dissertation are included in Table 3.1 and are taken as: $\alpha_H = 4$, $\tau_p = 2\text{ps}$, $a_{\text{diff}} = 5 \times 10^{-16}\text{cm}^2$, $N_{tr} = 2 \times 10^{18}\text{cm}^{-3}$, $n_g = 4$, $\Gamma = 0.04$, $C_Q = 0.6$, which are typical values for VCSELs [28] and are listed in Table 3.1. Two values for the coupling coefficient are considered, which we denote as Array 1 and Array 2 in the following

Table 3.1: List of variables. Only those denoted by orange appear in the rescaled (normalized) CREs.

Symbol	Parameter/Variables	Units	Value
$\mathcal{E}_{A,B}(t)$	Electric fields in cavity A and B (oscillate at optical frequencies)	$\mathrm{m}^{-3/2}$	-
$E_{A,B}(t)$	Electric fields (the slowly varying envelope)	$\mathrm{m}^{-3/2}$	-
Γ	Confinement factor	-	0.04
n_g	Group index	-	4
c	Speed of light	$\mathrm{m\ s}^{-1}$	$3 \times 10^8 \mathrm{m/s}$
v_g	Group velocity	$\mathrm{m\ s}^{-1}$	$= c/n_g$
a_{diff}	Differential gain	m^2	$5 \times 10^{-16} \mathrm{cm}^2$
$N_{A,B}$	Carrier density	m^{-3}	-
$N_{A,Bth}$	Threshold carrier density	m^{-3}	-
N_{tr}	Transparency carrier density	m^{-3}	$2 \times 10^{18}\ \mathrm{cm}^{-3}$
α_H	Linewidth enhancement factor	-	4
$\Omega_{A,B}$	Cavity resonant frequency (excluding amplitude-phase coupling)	s^{-1}	-
$\omega_{A,B}$	Total resonant frequency (including everything)	s^{-1}	-
$g_{A,B}$	Modal gain	s^{-1}	
$\gamma_{A,B}$	Net gain (loss) $\equiv g_{A,B} - 1/\tau_p$	s^{-1}	
$P_{A,B}$	Pump rate	$\mathrm{m}^{-3}\mathrm{s}^{-1}$	-
g_{th}	Threshold gain	m^{-1}	$= \dfrac{1}{\tau_p v_g \Gamma}$
C_Q	Pump parameter constant	-	0.6
τ_N	Carrier lifetime	s^{-1}	-
τ_p	Cavity photon lifetime	s	2 ps
κ	Coupling coefficient	s^{-1}	Device 1: $\kappa = 1 \times 10^9 \mathrm{rad/s}$; Device 2: $\kappa = 30 \times 10^9 \mathrm{rad/s}$
$\Delta\Omega$	$\equiv \Omega_B - \Omega_A$, passive-cavity frequency detuning	s^{-1}	-
ϕ	$\equiv \phi_B - \phi_A$, relative phase between two lasers	-	-
$Q_{A,B}$	Dimensionless pump parameter	-	-
$M_{A,B}$	Dimensionless carrier parameter	-	-
$Y_{A,B}$	Dimensionless field magnitude	-	-
$\Delta\omega$	$\equiv \omega_B - \omega_A$, total frequency detuning	s^{-1}	-
$\Delta\gamma$	$\equiv \gamma_B - \gamma_A$, gain contrast	s^{-1}	-

analysis. Array 1 has $\kappa = 1 \times 10^9 \mathrm{rad/s} = \frac{0.002}{\tau_p} \ll \frac{1}{\tau_p}$, while Array 2 has $\kappa = 30 \times 10^9 \mathrm{rad/s} = \frac{0.06}{\tau_p}$. Array 1 is in the limit of very weak coupling, while the coupling in Array 2 is stronger, being an experimentally estimated value for the coupled VCSEL arrays that have been characterized in this dissertation and in Ref. [14]. Note that both cases are in the weak coupling regime, meaning that the photons leak out of the system faster than interacting with the other cavity ($\kappa < 1/\tau_p$). Other optically coupled laser systems, such as index-guided ring coupled ring lasers, are found to have strong coupling, $\kappa > 1/\tau_p$ [18, 19]. Also note that both Array 1 and Array 2 have real-valued coupling coefficient, i.e., $\kappa_i = 0$. In coupled diode laser arrays, it is often that $\kappa_i \neq 0$, especially if we want to promote one of the coupled modes and suppress the other one to obtain single coupled-mode and hence a phased array. However, we choose to first demonstrate the physics when κ is real for its clear physical picture. *In Sections 3.3-3.5, κ is assumed to be real.* The effect of nonzero κ_i is discussed only in Section 3.6.

3.3 Very weakly coupled array under equal pumping (real κ)

We first consider Array 1 consisting of two semiconductor lasers that are very weakly coupled and equally pumped ($Q_A = Q_B$). The approximate analytical solution to the SSCREs (accurate to the first order of small $\tau_p\kappa$) was reported in Ref. [7], and is repeated here (for real-valued κ):

$$sin\phi \cong \frac{\Delta\Omega}{2\alpha_H\kappa} \tag{3.20}$$

$$M_A \cong 1 + 2\tau_p\kappa sin\phi \tag{3.21}$$

$$M_B \cong 1 - 2\tau_p\kappa sin\phi \tag{3.22}$$

$$Y_A^2 \cong Q\left(1 - 2\tau_p\kappa sin\phi\right) - 1 \tag{3.23}$$

$$Y_B^2 \cong Q\left(1 + 2\tau_p \kappa sin\phi\right) - 1 \tag{3.24}$$

Note that although there are also another two sets of solutions with very asymmetrical intensity distributions that mathematically satisfy the SSCREs [8], such modes are not realistic solutions in weakly coupled arrays, as discussed in Appendix C, and we ignore those two sets of solutions and only focus on the realistic solutions. From Equations (3.21)-(3.22), we know the carrier density distribution of the array as a function of cavity detuning ΔΩ. Using Equations (3.18) and (3.19), we can calculate the gain contrast and the total frequency detuning between cavities:

$$\Delta\gamma \cong -\frac{\Delta\Omega}{\alpha_H} \tag{3.25}$$

$$\Delta\omega \cong 0 \tag{3.26}$$

Equations (3.25)- (3.26) demonstrate that the cavity detuning ΔΩ induces a proportional gain contrast $\Delta\gamma$, but the total frequency detuning $\Delta\omega$ is negligibly small. This cavity-detuning-induced gain contrast elucidates why the two explanations for the origin of phase tuning do not contradict. From the coupled mode theory perspective, it is the gain contrast $\Delta\gamma$ that controls the phase tuning, and the total frequency detuning $\Delta\omega$ controls the intensity distribution [15]. But from the CRE perspective, we see that the cavity frequency detuning ΔΩ induces a proportional gain contrast $\Delta\gamma$, and hence it influences the beam steering through the induced gain contrast. On the other hand, the total frequency detuning $\Delta\omega$ is almost zero due to the balancing between ΔΩ and $\alpha_H\Delta\gamma$. Hence ΔΩ controls the beam steering through the lever of $\Delta\gamma$, but it has little effect on the intensity distribution. The consistency between coupled mode theory and CRE will be explained in further detail in the next sections. The key to maintaining this consistency is clearly distinguishing the two frequency detunings $\Delta\omega$ and ΔΩ, defined in Equations (3.17) and (3.19).

When calculating eigenmodes of the laser array using coupled mode theory, the input is gain contrast $\Delta\gamma$ and total frequency detuning $\Delta\omega$, neither of which can be easily measured experimentally. Hence an advantage of CRE analysis is that the input parameters are the cavity detuning $\Delta\Omega$ and the pump rates $Q_{A,B}$, which are both experimentally accessible.

We also solve SSCREs numerically and plot the solution versus $\Delta\Omega$ in Figure 3.3. Figures 3.3(a) and (b) agree well with Equations (3.25) and (3.26), respectively, with Figure 3.3(b) revealing detailed variations of $\Delta\omega$ beyond the first order approximate of Equation (3.26). Figures 3.3(c) and (d) also agree well with Equations (3.20) and (3.23)-(3.24), respectively.

Tuning of the relative phase is expressed as $sin\phi \cong \Delta\Omega/(2\alpha_H\kappa)$ in Equation (3.20). For each $\Delta\Omega$, there are two solutions of ϕ, which are $\phi_+ = \arcsin\left(\frac{\Delta\Omega}{2\alpha_H\kappa}\right)$ and $\phi_- = \pi - \arcsin\left(\frac{\Delta\Omega}{2\alpha_H\kappa}\right)$. From the definition of the $arcsin$ function, $\phi_+ \in [-\pi/2,\ \pi/2\ ]$, while $\phi_- \in [\pi/2,\ 3\pi/2\ ]$. When $\Delta\Omega = 0$, we have $\phi_+ = 0$ and $\phi_- = \pi$, as the in-phase and out-of-phase mode. When $\Delta\Omega \neq 0$, we have a tilted in-phase mode and tilted out-of-phase mode, labeled by + and – respectively. Other variables in the solution are labeled in accordance to ϕ, making one solution the set of $\left[\Delta\gamma_+, \Delta\omega_+, \left(\frac{Y_B}{Y_A}\right)_+, \phi_+\right]$ and the other solution corresponding to the set of $\left[\Delta\gamma_-, \Delta\omega_-, \left(\frac{Y_B}{Y_A}\right)_-, \phi_-\right]$.

The CRE analysis inherently has coupled mode theory embedded, so we can check consistency through the calculation of eigenmodes using couple mode theory with $\Delta\gamma_{+,-}$ and $\Delta\omega_{+,-}$ as input parameters. Coupled mode theory predicts two eigenmodes for $\Delta\gamma_+, \Delta\omega_+$ and another two for $\Delta\gamma_-, \Delta\omega_-$. However, only one out of the two eigenmodes for each set of $\Delta\gamma, \Delta\omega$ is consistent with the steady-state carrier rate equations, while the other eigenmode is not a valid solution. For example, if $\Delta\gamma_+, \Delta\omega_+$ are used as the input for coupled mode theory, the calculated eigenmodes are a tilted in-phase solution ($-\pi/2 < \phi < \pi/2$) and a tilted out-of-phase solution ($\pi/2 < \phi < 3\pi/2$). The tilted-in-phase solution satisfies Equation (3.15) automatically, while the tilted-out-of-phase solution does not. Similarly, for $\Delta\gamma_-, \Delta\omega_-$, only the tilted out-of-phase mode satisfies the carrier rate equation. In short, for the optical mode to be a solution of the SSCREs, not only does the mode need to be a solution of coupled mode theory, it also needs to have a self-consistent carrier density distribution that satisfies the rate equations.

When $|\Delta\Omega| > 2\alpha_H\kappa$, there are no steady-state solutions. Therefore, we can identity the cavity detuning range of $\Delta\Omega \in [-2\alpha_H\kappa, 2\alpha_H\kappa]$ to correspond to the mutual injection locking range. From Equation (3.20) this can be understood as the requirement of $sin\phi < 1$ for real ϕ. To the best of our knowledge, this expression of the locking range first appeared in Ref. [14] and was later formally derived in Ref. [7].

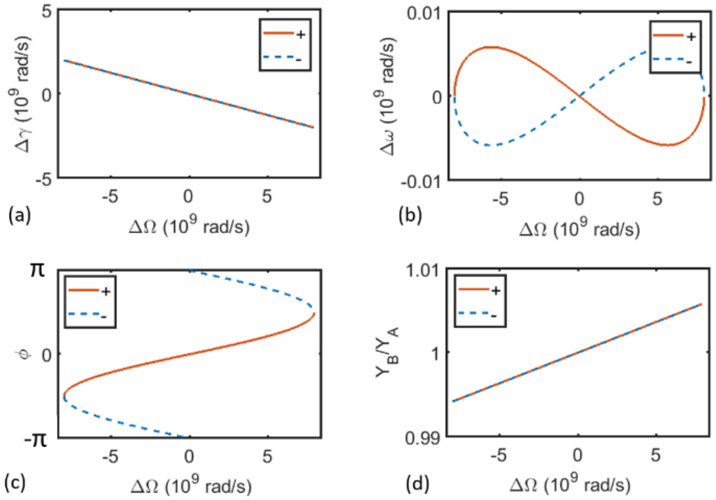

Figure 3.3: Numerical solutions of the SSCREs for Array 1 (very weak coupling, $\kappa = 0.002/\tau_p$). (a) Induced gain contrast; (b) total frequency detuning; (c) relative phase; (d) field magnitude ratio between two cavities are plotted versus the cavity detuning $\Delta\Omega$. For $|\Delta\Omega| < 2\alpha_H\kappa$ there are two sets of solutions, labeled as + and – respectively. In (a) and (d) the two solutions are too close to distinguish in the plot. The pump parameters are set to $Q_A = Q_B = 3.2$, corresponding to $I_A = I_B = 2.375\ I_{th}$ [31].

We consider the gain contrast induced by cavity detuning, shown in Figure 3.3(a). This gain contrast consists of equal amounts of optical gain and loss in the two cavities: $\gamma_A \cong \Delta\Omega/(2\alpha_H)$ and $\gamma_B = -\gamma_\mathrm{A}$. The existence of loss arises from the gain saturation. In other words, the optical loss arises from insufficient carrier density to maintain the excess amount of photons in the cavity. Intuitively, the connection between cavity detuning and the induced gain contrast can be understood as follows: with the existence of frequency detuning, the intensity distribution of the array eigenmodes becomes asymmetric, and this asymmetry in photon numbers in each cavity results in asymmetric depletion rates of carriers (similar to the spatial hole burning in a single laser). In turn, the carrier densities become asymmetric, which creates gain contrast. Mathematically, self-consistent solutions to the SSCREs are found to have equal gain and loss in each cavity while the frequency detuning is almost balanced out.

When the array has gain/loss contrast between the two cavities (i.e. $\Delta\gamma \neq 0$), we say the array is non-Hermitian. The energy transfer via optical coupling between two cavities does not exist within a Hermitian coupled array. This will be revisited in the next section, where we will see that the maximum magnitude of energy transfer scales with the coupling coefficient and thus it explains the different behavior observed in Array 2 compared to Array 1.

This cavity-detuning-induced gain and loss suggests another way of obtaining PT symmetry and exceptional points. In fact, in the limit of very weak coupling, the array under equal pumping nearly exhibits PT symmetry, in the sense that $\Delta\omega \cong 0$ to the first order of $\tau_p\kappa$. However, to reach exact PT symmetry and the exceptional points, tuning of the pump rates is necessary, as discussed in the following sections.

3.4 Weakly coupled arrays under unequal pumping (real κ)

For unequal pumping into the two lasers, because a general analytical solution is not available, we solve SSCREs numerically using a numerical root search. The two cases of very weak coupling (Array 1) and moderate coupling (Array 2) are compared under the conditions of cavity detuning $\Delta\Omega$ (horizontal axis in Figures 3.4 and 3.5) and one of the pump rates Q_B (vertical axis in Figures 3.4 and 3.5) are varied. The in-phase modes for Array 1 and 2 are plotted in Figure 3.4 and Figure 3.5, respectively, where the color scales in the plots corresponds to the induced gain contrast, frequency detuning, relative phase, and the magnitude of the field ratio between the elements. The red lines show where the array is PT symmetric, which is discussed in greater detail in the next section. The out-of-phase modes are plotted in the Appendix D.

In the case of very weak coupling presented in Figure 3.4, from the color gradient we see that varying Q_B has little effect on the gain contrast $\Delta\gamma$ or the relative phase ϕ [Figure 3.4(a) and 3.4(c)], but it does control the total frequency detuning $\Delta\omega$ and the field magnitude ratio (Y_B/Y_A) [Figure 3.4(b) and 3.4(d)]. The gain contrast and the relative phase are mostly controlled by the cavity detuning $\Delta\Omega$, evident from the color gradient in Figures 3.4(a) and 3.4(c) being mostly along the horizontal direction. The in-phase solutions to the SSCREs for moderate coupling are shown in Figure 3.5. Similar to the case of very weak coupling, varying the pump parameter Q_B still has little effect on gain contrast or phase tuning. However, the total frequency detuning $\Delta\omega$ and the field magnitude ratio are now controlled by both the Q_B and $\Delta\Omega$, which is different from the case of very weak coupling.

For both Array 1 and Array 2, we find a finite region where steady-state solutions exist (represented by the colored regions in Figures 3.4 and 3.5), which we identify as the locking

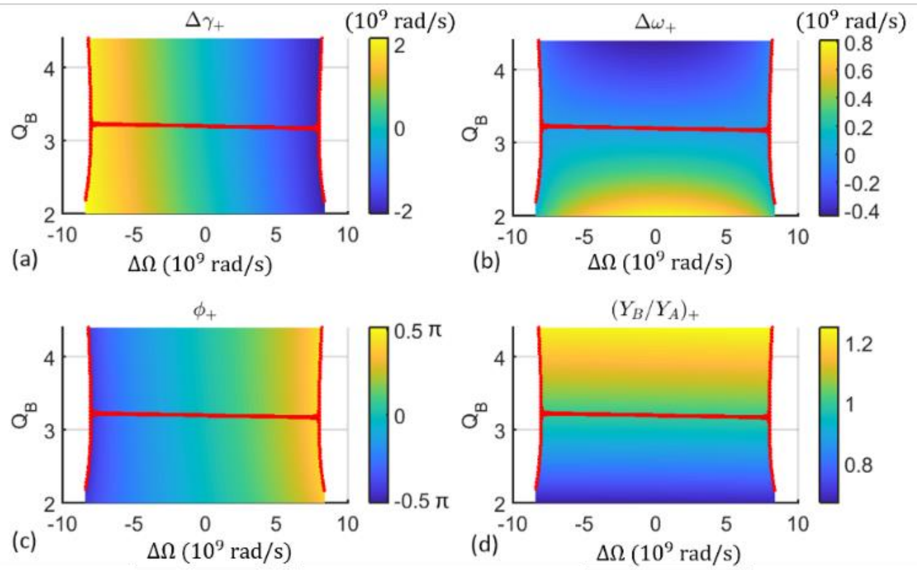

Figure 3.4: The tilted in-phase solution for Array 1 ($\kappa = 0.002/\tau_p$). (a) Induced gain contrast; (b) total frequency detuning; (c) relative phase; and (d) field magnitude ratio versus the cavity detuning and pump parameter Q_B, while Q_A is fixed at 3.2. The pump parameters correspond to having I_A fixed at 2.375 I_{th}, while I_B varies from 1.625 I_{th} to 3.125 I_{th}. Red lines show where the array is PT symmetric [31].

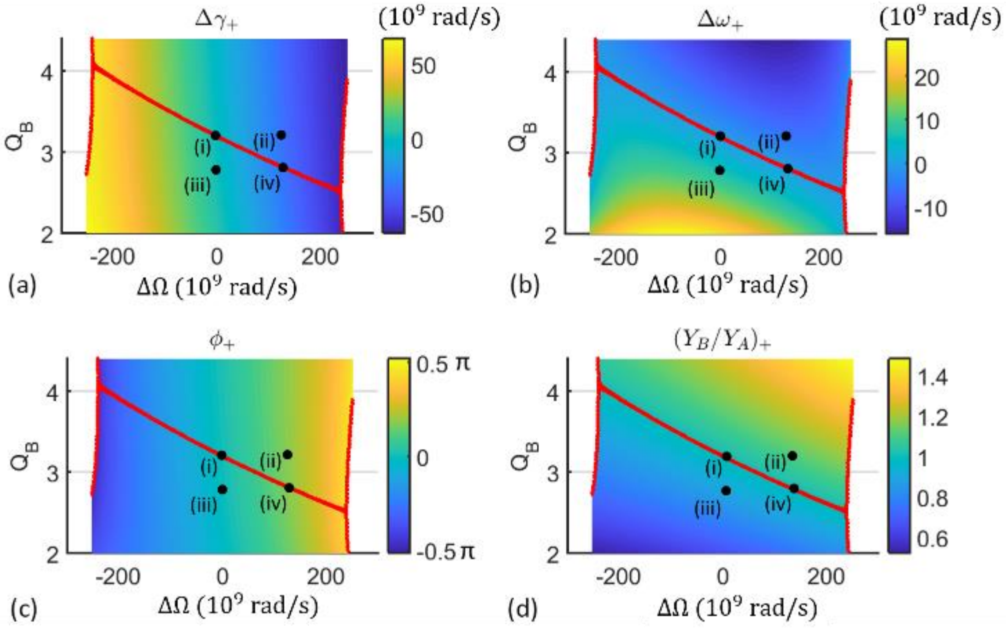

Figure 3.5: The tilted in-phase solution for Array 2 ($\kappa = 0.06/\tau_p$). (a) Induced gain contrast; (b) total frequency detuning; (c) relative phase; and (d) field magnitude ratio versus the cavity detuning and pump parameter Q_B. Again, Q_A is fixed at 3.2, while Q_B varies from 2 to 4.4. The locations labeled with numbers (i)-(iv) correspond to the schematics in Figure 3.6. Red lines show where the array is PT symmetric [31].

region for the two lasers. Outside the locking region, no steady-state solution exists, which suggests either multi-mode lasing or temporally chaotic behavior [7, 32]. The horizontal width of the coupling region ($|\Delta\Omega|_{max}$) in Figures 3.4(a) and 3.5(a) changes slightly with varying Q_B, and is approximately constant with $|\Delta\Omega|_{max} \cong 2\alpha_H\kappa$.

The tilted out-of-phase solutions are plotted in Appendix D. Their response to the tuning of $\Delta\Omega$ and Q_B is similar to the in-phase solutions plotted in Figures 3.4 and 3.5. In coupled VCSEL arrays, experimentally tuning the injected currents into each laser corresponds to varying both $Q_{A,B}$ and the $\Delta\Omega$ at the same time. The magnitude of injection current not only changes the pump parameters $Q_{A,B}$, but also varies the cavity resonance frequency $\Omega_{A,B}$ through ohmic heating and the refractive index temperature dependence. Hence varying the injection currents is equivalent to moving along a given line or trajectory on the 2D maps shown in Figures 3.4 and 3.5.

The different behaviors of very weak coupling (Array 1) and moderate coupling (Array 2) can be interpreted from the perspective of energy conservation and energy transfer. In the very weak coupling limit (Array 1 in Figure 3.4), because the energy transfer between two lasers is very limited, we have approximate energy conservation in each laser. This means that in the very weak coupling limit, Y_B/Y_A is almost solely determined by Q_B/Q_A, because the carrier injection rate (proportional to $Q_{B,A}$) needs to balance the carrier depletion rate, which is proportional to number of photons in the cavity (proportional to $Y_{B,A}^2$). However, when the optical coupling between cavities becomes stronger, the photon-mediated energy transfer between cavities can disturb this balance. For example, for Array 2 in Figure 3.5, Y_B^2/Y_A^2 can be as large as 1.4 when $Q_B/Q_A = 1$, meaning that the photons in cavity B come not only from carriers injected into B, but also from carriers injected into cavity A. This energy transfer is connected to the gain/loss contrast between cavities. The cavity with more photons than injected carriers is interpreted as a lossy cavity, and it gains energy from the other cavity through optical coupling. The cavity that provides energy to the other cavity through optical coupling is interpreted to possess net gain.

There are four cases under equal and unequal pumping that can be considered, and these cases are schematically depicted in Figure 3.6. The sizes of arrows in Figure 3.6 illustrate the magnitude of energy flows associated with the processes of carrier injection, stimulated emission, and optical output from end mirrors of the cavities. The sizes of boxes and circles illustrate the carrier densities $M_{A,B}$ and photon densities $Y_{A,B}^2$. Four steady-state solutions, (i)-(iv), are shown in Figure 3.6, which correspond to the four operating points labeled in Figure 3.5. Solution (i) is where the array is under equal pumping and zero cavity detuning. The array is Hermitian because there is no net gain or loss in either cavity. Solution (ii) is with equal pumping but nonzero cavity detuning $\Delta\Omega$, and the array is non-Hermitian due to gain/loss contrast induced by the cavity detuning. Although the pump rates into each cavity are the same in this situation, nonzero cavity detuning induces asymmetry in photon densities, which in turn affects the carrier depletion rate and results in asymmetric carrier densities. Also note the net energy flow from cavity A into cavity B through optical coupling. This energy flow is necessary for power conservation, which can be examined by summing up all the energy flows in and out of each reservoir. Solution (iii) is with nonequal pumping and zero cavity detuning. In this case, the steady-state solution shows $\Delta\gamma \cong 0$, meaning that the array is approximately Hermitian. In other words, differential pumping does not induce significant non-Hermiticity. At last, solution (iv) is with judiciously chosen unequal pumping and cavity detuning that makes the array PT symmetric.

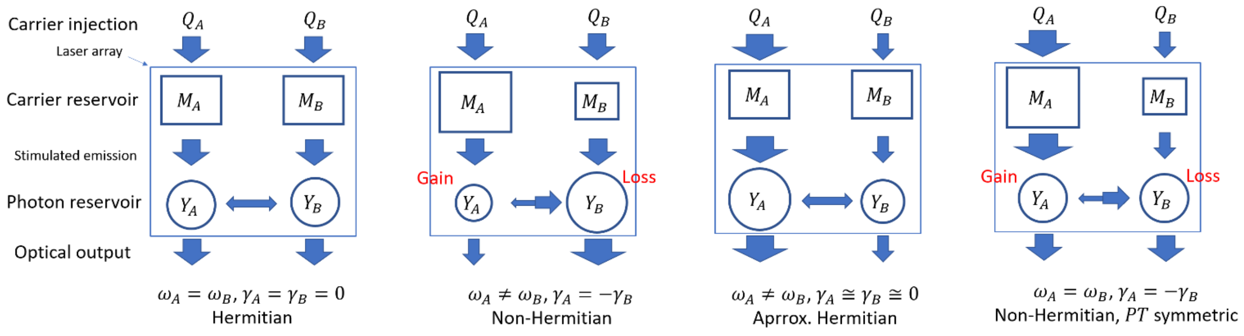

$\omega_A = \omega_B, \gamma_A = \gamma_B = 0$
Hermitian
(i) $(Q_A = Q_B, \Delta\Omega = 0)$

$\omega_A \neq \omega_B, \gamma_A = -\gamma_B$
Non-Hermitian
(ii) $(Q_A = Q_B, \Delta\Omega \neq 0)$

$\omega_A \neq \omega_B, \gamma_A \cong \gamma_B \cong 0$
Aprrox. Hermitian
(iii) $(Q_A \neq Q_B, \Delta\Omega = 0)$

$\omega_A = \omega_B, \gamma_A = -\gamma_B$
Non-Hermitian, PT symmetric
(iv) $(Q_A \neq Q_B, \Delta\Omega \neq 0)$

Figure 3.6: Illustration of the distributions of carrier densities, photon densities, gain/loss, and energy flows at points labeled by (i)-(iv) in Figure 3.5. Sizes of the boxes, circles, and arrows illustrate the asymmetry in carrier densities, photon densities, and energy flows (in the processes of carrier injection, stimulated emission, optical coupling, and optical output) [31].

3.5 PT symmetry and exceptional points (real κ)

As discussed in Section 2.2, for two identical resonators coupled through a real coupling coefficient κ, the system is invariant under $\hat{P}\hat{T}$ if $\omega_A = \omega_B$, and $\gamma_A = -\gamma_B$ [15, 18-21, 33]. However, when the system is PT symmetric (i.e., $\hat{\boldsymbol{P}}\hat{\boldsymbol{T}}\bar{\bar{\mathbf{M}}} = \bar{\bar{\mathbf{M}}}$), the eigenmodes of the system may not be PT-symmetric. It would be designated “unbroken PT symmetry” if both the system and the eigenmodes are PT-symmetric. On the other hand, it would be designated “broken PT symmetry” when the system is PT-symmetric but the eigenmodes are not. It is known that unbroken PT symmetry happens when $\Delta\gamma < 2\kappa$, while PT symmetry is spontaneously broken when $\Delta\gamma > 2\kappa$. At $\Delta\gamma = 2\kappa$, which is known as the exceptional points, the two eigenmodes collapse. Recently, improved sensing functionality has been predicted and demonstrated around the exceptional points [26, 27].

Points with $\omega_A = \omega_B$ are labeled in red in Figures. 3.4 and 3.5, which correspond to where the array exhibits PT symmetry. In Figure 3.7, we specifically denote unbroken and broken PT symmetry regimes as blue and red lines; notice that the exceptional points occur at their intersections. Here the gain contrast arises from equal gain and loss (i.e., $\gamma_A = -\gamma_B$), meaning that it is naturally PT symmetric without the necessity of “gauge transformation” that was mentioned in Section 2.2.

Along the line of unbroken PT symmetry, there are two sets of solutions to the SSCREs. At the exceptional points, the two sets of solutions collapse to the same values. Along the broken PT symmetry lines, there is only one set of solution to the SSCREs that satisfies both the coupled mode theory and the carrier density rate equations. Analytical solutions to the SSCREs are available along the line of unbroken PT symmetry, as discussed in the following.

Operating the laser array at the exceptional point requires judiciously chosen pump ratio and cavity detuning. In most coupled diode laser arrays, since the pump ratio and cavity detuning are both controlled by the same experimental parameter, i.e. the injection currents, it can be challenging to find and operate the array at its exceptional point. However, the PT symmetry-breaking mode is relatively easy to achieve as long as there is sufficient cavity detuning to drive the array to the boundary of locking region (for example see Figure 3.1). We note also that the broken PT symmetry can be achieved by exclusively cavity detuning (with equal pumping).

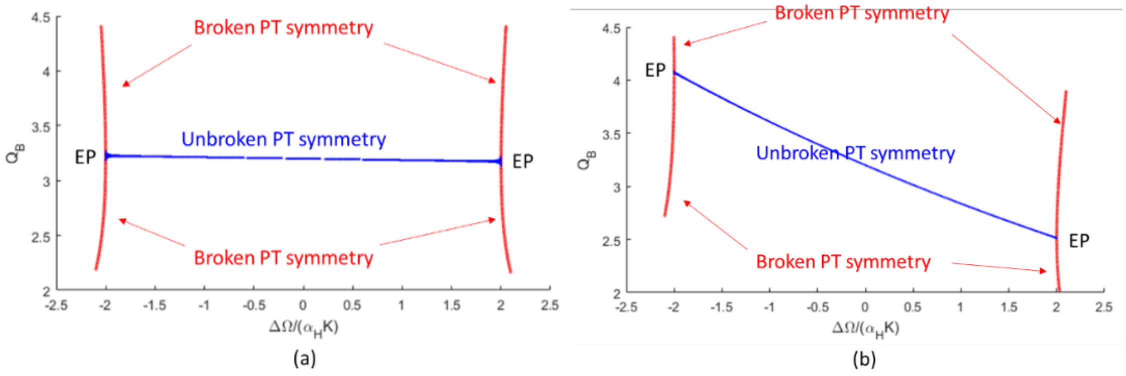

(a) (b)

Figure 3.7: Location of unbroken PT symmetry (blue curves), broken PT symmetry (red curves) and exceptional points (black points) on the 2D parameter space of $(Q_B, \Delta\Omega)$ for (a) very weak coupling (Array 1) and (b) moderate coupling (Array 2) [31].

A further observation is that the two sets of solutions to the SSCREs are generally different from each other, but they converge to the same solution along the lines of broken PT symmetry. Along the line of unbroken PT symmetry, the two sets of solutions share the same values of $\Delta\gamma, \Delta\omega, Y_B/Y_A$, but not ϕ. Instead, they have $\phi_+ + \phi_- = \pi$. This observation is discussed more detail in Appendix D.

The condition of unbroken PT symmetry can be found analytically in the 2D parameter space of Q_B and $\Delta\Omega$ (for example in Figures 3.4, 3.5, 3.6, D.1 and D.2):

$$\frac{Q_B}{Q_A} = \frac{1 - 2\tau_p \kappa sin\phi}{1 + 2\tau_p \kappa sin\phi}$$

$$\Delta\Omega = 2\alpha_H \kappa sin\phi$$

$$\phi \in (-\frac{\pi}{2}, \frac{\pi}{2})$$

Exceptional points are located at the ends of the unbroken PT symmetry region, expressed as

$$\frac{Q_B}{Q_A} = \frac{1 \mp 2\tau_p \kappa}{1 \pm 2\tau_p \kappa}$$

$$\Delta\Omega = \pm 2\alpha_H \kappa$$

Along the line of unbroken PT symmetry, we have analytical solution to the steady-state coupled rate equations:

$$\Delta\omega_{+,-} = 0$$

$$\Delta\gamma_{+,-} = -\frac{\Delta\Omega}{\alpha_H}$$

$$sin\phi = \frac{\Delta\Omega}{2\alpha_H \kappa}$$

$$M_A = 1 + 2\tau_p \kappa sin\phi$$

$$M_B = 1 - 2\tau_p \kappa sin\phi$$

$$Y_A^2 = Y_B^2 = \frac{1}{2}(Q_A + Q_B - 2)$$

This solution takes the same form as the approximate analytical solution for the weakly coupled equally pumped array that was reported in Ref. [7] and repeated as (3.20)-(3.24) in Section 3.3. This can be understood by noting that when the coupling coefficient approaches zero ($\tau_p \kappa \rightarrow 0$), the line of unbroken PT symmetry converges to the line of $Q_B = Q_A$. This solution is also consistent with the analytical expressions in Ref. [8], where a general analytical expression has been provided in an inverse form to what we have solved for (system parameters in terms of optical mode characteristics).

3.6 Nonzero imaginary part in the coupling coefficient

3.6.1 Gain splitting and threshold splitting

As we have discussed in Chapter 2, the imaginary part of the coupling coefficient represents the gain splitting between the two normal modes. It originates from a nonuniform gain/loss profile in the system, for example arising from gain-guiding confinement, or gain/loss in the coupling region. Gain/loss in the coupling region overlaps differently with the in-phase mode versus the out-of-phase mode, and this difference splits the gain/loss experienced by the in-phase and out-of-phase normal modes. The direct result of gain splitting is a threshold difference between the modes, which we refer to as "threshold splitting". Due to the difference in modal gain that the two normal modes experience, they have different threshold carrier densities.

When the two lasers are symmetrical (i.e., $\Delta\Omega = 0$, $Q_A = Q_B = Q$), the normal modes are either symmetrical ($M_A = M_B = M_+$, $Y_A = Y_B = Y_+$, and $\phi = 0$) or anti-symmetrical ($M_A = M_B = M_-$, $Y_A = Y_B = Y_-$, and $\phi_- = \pi$). When there is no imaginary part in the coupling coefficient, the threshold carrier densities for the two normal modes are $M_+ = M_- = 1$, which means that the two normal modes have the same threshold carrier density, and it is the same as the threshold of an isolated laser. In other words, the coupling does not vary the threshold carrier density.

On the other hand, when there exists nonzero imaginary part in the coupling coefficient, say $\kappa_i < 0$, meaning that the in-phase mode is preferred according to our definition [Equation (2.17)], we have

$$M_+ = 1 + 2\tau_p\kappa_i \tag{3.27}$$

$$M_- = 1 - 2\tau_p\kappa_i \tag{3.28}$$

Because $\kappa_i < 0$ we have $M_+ < 1 < M_-$, meaning the in-phase normal mode has lower threshold than the threshold of an isolated laser (which is 1), and the out-of-phase normal mode has higher threshold than that of an isolated laser. In other words, the coupling between the lasers has the effect of reducing the threshold for the in-phase mode (to less than that of an isolated laser), and increasing the threshold for the out-of-phase mode. This behavior will be shown in the experimental characterization in Chapter 5.

This threshold splitting favors one of the normal modes over the other. The mutual coherence between the lasers can be associated with this threshold splitting. When only one normal mode is lasing, we have perfect coherence; when both normal modes are lasing with equal intensity, we have zero coherence; when both normal modes are lasing but with unequal intensity, we have partial coherence. This argument has also been quantitatively established in stochastic coupled mode theory for the study of partial coherence in coupled laser arrays [5].

3.6.2 Non-Hermitian coupling and non-Hermiticity

Complex coupling coefficient itself can make the coupling matrix $\bar{\bar{\mathbf{M}}}$ non-Hermitian [34, 35]. In our case

$$\bar{\bar{\mathbf{M}}} = \begin{bmatrix} \omega_A + i\gamma_A & -\kappa_r - i\kappa_i \\ -\kappa_r - i\kappa_i & \omega_B + i\gamma_B \end{bmatrix}$$

and $\bar{\bar{\mathbf{M}}}$ is not Hermitian, neither is it PT-symmetric.

With the existence of $\kappa_i \neq 0$, the influences of $\Delta\omega$ and $\Delta\gamma$ on the normal modes are mixed. It is found that $\Delta\omega$ contributes to both the intensity asymmetry and beam steering, and $\Delta\gamma$ contributes to both the intensity asymmetry and beam steering as well. More importantly, an exceptional point will not occur for $\Delta\omega = 0, \Delta\gamma = \pm 2\kappa$ anymore. Instead, from Equation (2.13), we see that the exceptional points are at

$$\Delta\omega^2 - \Delta\gamma^2 + 4(\kappa_r^2 - \kappa_i^2) = 0 \tag{3.29}$$

$$\Delta\omega\Delta\gamma + 4\kappa_r\kappa_i = 0 \tag{3.30}$$

From Equation (3.30), we see that unless $\kappa_i = 0$, operating the array at an exceptional point mode requires simultaneously both gain contrast $\Delta\gamma$ and frequency detuning $\Delta\omega$. An example illustration of the eigenmode dependence on $\Delta\omega$ and $\Delta\gamma$ is presented in Figure 3.8. The left column [(a)-(c)] corresponds to when the coupling coefficient is real-valued, while the right column [(d)-(f)] shows the cases when the coupling coefficient is complex.

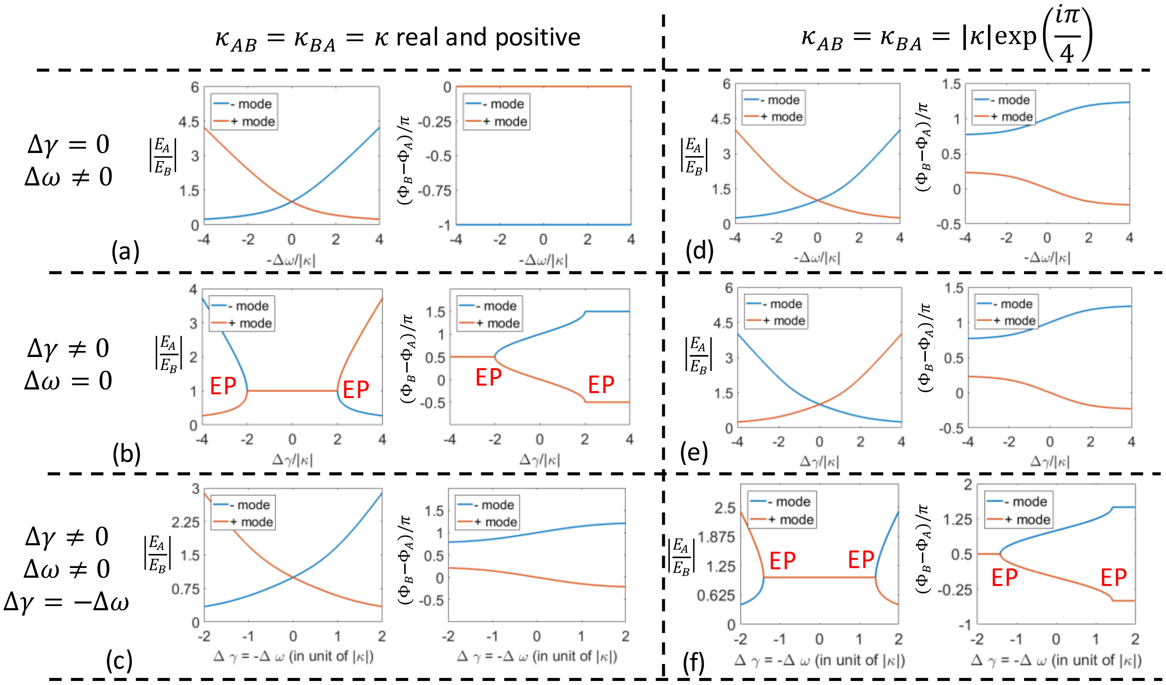

Figure 3.8: Array eigenmode dependence (blue and red curves) on $\Delta\omega$ and $\Delta\gamma$. The left column [(a)-(c)] correspond to real-valued coupling coefficients, while the right column [(d)-(f)] correspond to complex-valued coupling coefficients. Exceptional points are labeled as EP.

3.7 Summary

Mode tuning in coupled semiconductor lasers has been studied by solving the steady-state coupled rate equations. When the coupling coefficient is real-valued, we show that, depending on the strength of coupling compared to the cavity loss rate, the coupled array responds differently to unequal pumping and cavity detuning. When $\kappa \ll 1/\tau_p$, which is the limit of very weak coupling, the cavity detuning induces a gain contrast, but the frequency detuning is almost completely balanced out by the frequency shift from the asymmetric carrier distribution. In the moderate coupling case ($\kappa = 0.06/\tau_p$), the frequency detuning is partially balanced out. In either weak or moderate coupling, gain contrast is more effectively introduced by the cavity detuning than by the difference in pump rates, and the relative phase between two lasers is controlled by the cavity detuning, through the lever of induced gain contrast.

In the limit of very weak coupling, the tuning of intensity ratio between lasers is controlled almost solely by the pump rate difference, as expected from the conservation of energy and particle numbers in each cavity. In moderate coupling, because of the photon-mediated energy transfer between cavities, the particle number conservation should be considered in terms of the whole array instead of the individual cavities, and the intensity ratio is controlled by both the pump rate difference and $\Delta\Omega$. This summary is illustrated in Figure 3.9.

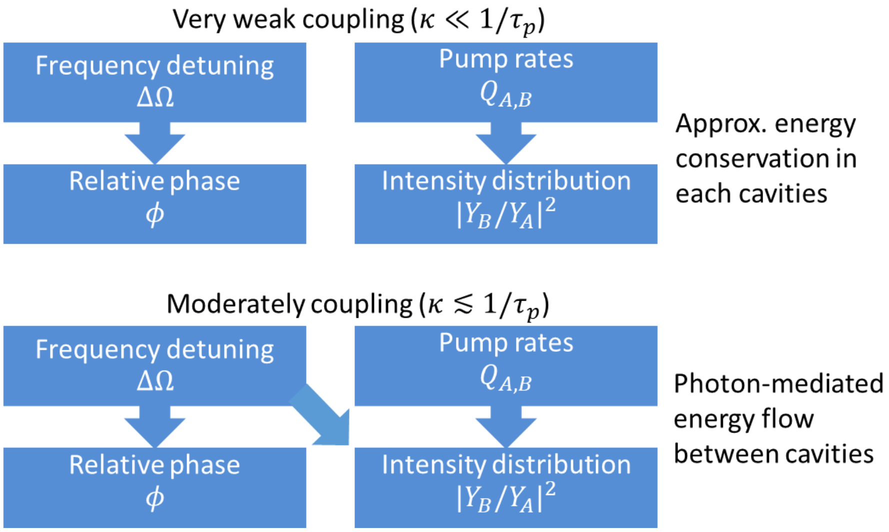

Figure 3.9: Mode control comparison between very weakly coupled laser arrays and moderately coupled arrays (real κ).

We have also shown that to achieve the modes that correspond to unbroken PT symmetry or exceptional points in the semiconductor arrays with weak or moderate coupling, judiciously chosen cavity detuning and unequal pump rates are required. However, broken PT symmetry is less challenging to achieve, and it is possible to drive the array to PT symmetry breaking by exclusively cavity detuning.

Finally, we discussed the physical effects related to the imaginary component in the coupling coefficient (i.e., κ_i), for example the threshold splitting between in-phase mode and out-of-phase modes. This observation leads to a practical approach to extract κ_i in experiments.

Measurements of the threshold splitting (and hence the existence of κ_i) will be reported in Chapter 5, as extracted from the output power versus current (L-I) characteristics of the coupled VCSEL arrays. We also point out that the existence of κ_i changes the mode control mechanism and the location of exceptional points on the 2D $(\Delta\omega, \Delta\gamma)$ plane.

The results presented in the chapter have important implications for mode control in coupled semiconductor laser arrays, as well as the search for PT symmetry and exceptional points in such systems. The stability of the steady-state modes will be discussed in the next chapter.

3.8 References

[1] D. Marcuse, "The coupling of degenerate modes in two parallel dielectric waveguides," *Bell System Technical Journal,* vol. 50, no. 6, pp. 1791-1816, 1971.

[2] A. Yariv, "Coupled-mode theory for guided-wave optics," *IEEE Journal of Quantum Electronics,* vol. 9, no. 9, pp. 919-933, 1973.

[3] A. Hardy and W. Streifer, "Coupled mode theory of parallel waveguides," *Journal of Lightwave Technology,* vol. 3, no. 5, pp. 1135-1146, 1985.

[4] H. Haus, W. Huang, S. Kawakami, and N. Whitaker, "Coupled-mode theory of optical waveguides," *Journal of Lightwave Technology,* vol. 5, no. 1, pp. 16-23, 1987.

[5] D. F. Siriani, K. D. Choquette, and P. S. Carney, "Stochastic coupled mode theory for partially coherent laser arrays," *J Opt Soc Am A,* vol. 27, no. 3, pp. 501-508, 2010.

[6] H. G. Winful and S. S. Wang, "Stability of phase locking in coupled semiconductor-laser arrays," *Applied Physics Letters,* vol. 53, no. 20, pp. 1894-1896, 1988.

[7] M. J. Adams, N. Li, B. R. Cemlyn, H. Susanto, and I. D. Henning, "Effects of detuning, gain-guiding, and index antiguiding on the dynamics of two laterally coupled semiconductor lasers," *Physical Review A,* vol. 95, no. 5, p. 053869, 2017.

[8] Y. Kominis, V. Kovanis, and T. Bountis, "Controllable asymmetric phase-locked states of the fundamental active photonic dimer," *Physical Review A,* vol. 96, no. 4, p. 043836, 2017.

[9] Y. Kominis, V. Kovanis, and T. Bountis, "Spectral signatures of exceptional points and bifurcations in the fundamental active photonic dimer," *Physical Review A,* vol. 96, no. 5, p. 053837, 2017.

[10] C. H. Henry, "Theory of the linewidth of semiconductor-lasers," *IEEE Journal of Quantum Electronics,* vol. 18, no. 2, pp. 259-264, 1982.

[11] E. Kapon, Z. Rav-Noy, L. T. Lu, M. Yi, S. Margalit, and A. Yariv, "Phase-locking characteristics of coupled ridge-waveguide InP/InGaAsP diode lasers," *Applied Physics Letters,* vol. 45, no. 11, pp. 1159-1161, 1984.

[12] A. C. Lehman, J. J. Raftery, A. J. Danner, P. O. Leisher, and K. D. Choquette, "Relative phase tuning of coupled defects in photonic crystal vertical-cavity surface-emitting lasers," *Applied Physics Letters,* vol. 88, no. 2, p. 021102, 2006.

[13] M. T. Johnson, D. F. Siriani, J. D. Sulkin, and K. D. Choquette, "Phase and coherence extraction from a phased vertical cavity laser array," *Applied Physics Letters,* vol. 101, no. 3, p. 031116, 2012.

[14] M. T. Johnson, D. F. Siriani, M. P. Tan, and K. D. Choquette, "Beam steering via resonance detuning in coherently coupled vertical cavity laser arrays," *Applied Physics Letters,* vol. 103, no. 20, p. 201115, 2013.

[15] Z. Gao, S. T. Fryslie, B. J. Thompson, P. S. Carney, and K. D. Choquette, "Parity-time symmetry in coherently coupled vertical cavity laser arrays," *Optica,* vol. 4, no. 3, pp. 323-329, 2017.

[16] C. E. Ruter, K. G. Makris, R. El-Ganainy, D. N. Christodoulides, M. Segev, and D. Kip, "Observation of parity-time symmetry in optics," *Nature Physics,* vol. 6, no. 3, pp. 192-195, 2010.

[17] M. T. Johnson, D. F. Siriani, M. P. Tan, and K. D. Choquette, "High-speed beam steering with phased vertical cavity laser arrays," *IEEE Journal of Selected Topics in Quantum Electronics,* vol. 19, no. 4, p. 1701006, 2013.

[18] H. Hodaei, M. A. Miri, M. Heinrich, D. N. Christodoulides, and M. Khajavikhan, "Parity-time-symmetric microring lasers," *Science,* vol. 346, no. 6212, pp. 975-978, 2014.

[19] B. Peng *et al.*, "Parity-time-symmetric whispering-gallery microcavities," *Nature Physics,* vol. 10, no. 5, pp. 394-398, 2014.

[20] L. Chang *et al.*, "Parity–time symmetry and variable optical isolation in active–passive-coupled microresonators," *Nature Photonics,* vol. 8, no. 7, pp. 524-529, 2014.

[21] M. Liertzer, L. Ge, A. Cerjan, A. D. Stone, H. E. Tureci, and S. Rotter, "Pump-induced exceptional points in lasers," *Phys Rev Lett,* vol. 108, no. 17, p. 173901, 2012.

[22] A. U. Hassan, H. Hodaei, M. A. Miri, M. Khajavikhan, and D. N. Christodoulides, "Nonlinear reversal of the PT-symmetric phase transition in a system of coupled semiconductor microring resonators," *Physical Review A,* vol. 92, no. 6, p. 063807, 2015.

[23] L. Ge and R. El-Ganainy, "Nonlinear modal interactions in parity-time (PT) symmetric lasers," *Scientific Reports,* vol. 6, no. April, p. 24889, 2016.

[24] H. Hodaei *et al.*, "Design considerations for single-mode microring lasers using parity–time symmetry," *IEEE Journal of Selected Topics in Quantum Electronics,* vol. 22, no. 5, pp. 1-7, 2016.

[25] M. H. Teimourpour, M. Khajavikhan, D. N. Christodoulides, and R. El-Ganainy, "Robustness and mode selectivity in parity-time (PT) symmetric lasers," *Scientific Reports,* vol. 7, no. 1, p. 10756, 2017.

[26] H. Hodaei *et al.*, "Enhanced sensitivity at higher-order exceptional points," *Nature,* vol. 548, no. 7666, pp. 187-191, 2017.

[27] W. Chen, S. Kaya Ozdemir, G. Zhao, J. Wiersig, and L. Yang, "Exceptional points enhance sensing in an optical microcavity," *Nature,* vol. 548, no. 7666, pp. 192-196, 2017.

[28] L. A. Coldren, S. W. Corzine, and M. L. Mashanovitch, *Diode Lasers and Photonic Integrated Circuits*. John Wiley & Sons, 2012.

[29] S. T. M. Fryslie, M. T. Johnson, and K. D. Choquette, "Coherence tuning in optically coupled phased vertical cavity laser arrays," *IEEE Journal of Quantum Electronics*, vol. 51, no. 11, pp. 1-6, 2015.

[30] S. T. M. Fryslie *et al.*, "Modulation of coherently coupled phased photonic crystal vertical cavity laser arrays," *IEEE Journal of Selected Topics in Quantum Electronics,* vol. 23, no. 6, pp. 1-9, 2017.

[31] Z. Gao, M. T. Johnson, and K. D. Choquette, "Rate equation analysis and non-Hermiticity in coupled semiconductor laser arrays," *Journal of Applied Physics,* vol. 123, no. 17, p. 173102, 2018.

[32] H. G. Winful and L. Rahman, "Synchronized chaos and spatiotemporal chaos in arrays of coupled lasers," *Phys Rev Lett,* vol. 65, no. 13, pp. 1575-1578, 1990.

[33] C. M. Bender, M. V. Berry, and A. Mandilara, "Generalized PT symmetry and real spectra," *Journal of Physics A-Mathematical and General,* vol. 35, no. 31, pp. L467-L471, 2002.

[34] Z. Gao *et al.*, "Non-Hermitian aspects of coherently coupled vertical cavity laser arrays," in *CLEO: Science and Innovations*, 2017, p. SW1C. 4: Optical Society of America.

[35] S. Longhi and L. Feng, "Non-Hermitian laser phase locking," *arXiv preprint arXiv:1802.05439,* 2018.

CHAPTER 4: COUPLED RATE EQUATION ANALYSIS: SMALL-SIGNAL DYNAMICS

In Chapter 3 we solved the steady-state coupled rate equations (SSCREs) and obtained the steady-state solutions [1]. An important question regarding the steady-state solutions is if they are stable [2, 3]. In other words, if there is a small perturbation applied to the steady-state solution, will the perturbation decay (stable) or grow (unstable) over time. In this chapter we will address this question by studying the small-signal dynamics of the array. By studying the temporal evolution of a small perturbation that is added into the steady-state solution, we can not only obtain the stability of the steady-state solution, but also calculate the small-signal response of the array under external modulation [4, 5].

4.1 Differential analysis of the coupled rate equations

From the coupled rate equations [e.g. Equations (3.12)-(3.15)], if we add a small perturbation to the steady-state solution, the temporal evolution of this small perturbation follows this linear differential equation:

$$\frac{d}{dt}\begin{bmatrix} \Delta Y_A \\ \Delta Y_B \\ \Delta\phi \\ \Delta M_A \\ \Delta M_B \end{bmatrix} = \begin{bmatrix} A_{Y_AY_A} & A_{Y_AY_B} & A_{Y_A\phi} & A_{Y_AM_A} & 0 \\ A_{Y_BY_A} & A_{Y_BY_B} & A_{Y_B\phi} & 0 & A_{Y_BM_B} \\ A_{\phi Y_A} & A_{\phi Y_B} & A_{\phi\phi} & A_{\phi M_A} & A_{\phi M_B} \\ A_{M_AY_A} & 0 & 0 & A_{M_AM_A} & 0 \\ 0 & A_{M_BY_B} & 0 & 0 & A_{M_BM_B} \end{bmatrix}\begin{bmatrix} \Delta Y_A \\ \Delta Y_B \\ \Delta\phi \\ \Delta M_A \\ \Delta M_B \end{bmatrix} + \frac{1}{\tau_N}\begin{bmatrix} 0 \\ 0 \\ 0 \\ \Delta Q_A \\ \Delta Q_B \end{bmatrix} \tag{4.1}$$

where $\begin{bmatrix} \Delta Y_A \\ \Delta Y_B \\ \Delta\phi \\ \Delta M_A \\ \Delta M_B \end{bmatrix}$ is the small perturbation and $\Delta Q_{A,B}$ represents the external current modulation, if it exists. Equation (4.1) is the small-signal (differential) analysis of the coupled rate equations, similar to the small-signal analysis in an isolated diode laser [4, 5]. The steady-state solution $\begin{bmatrix} Y_A \\ Y_B \\ \phi \\ M_A \\ M_B \end{bmatrix}$ (dependent on the DC bias) determines the matrix $\bar{\bar{\boldsymbol{A}}}$, whose terms are defined as

$$\bar{\bar{\boldsymbol{A}}} \equiv \begin{bmatrix} A_{Y_AY_A} & A_{Y_AY_B} & A_{Y_A\phi} & A_{Y_AM_A} & 0 \\ A_{Y_BY_A} & A_{Y_BY_B} & A_{Y_B\phi} & 0 & A_{Y_BM_B} \\ A_{\phi Y_A} & A_{\phi Y_B} & A_{\phi\phi} & A_{\phi M_A} & A_{\phi M_B} \\ A_{M_AY_A} & 0 & 0 & A_{M_AM_A} & 0 \\ 0 & A_{M_BY_B} & 0 & 0 & A_{M_BM_B} \end{bmatrix}$$

$$A_{Y_AY_A} = \frac{1}{2\tau_p}(M_A - 1)$$

$$A_{Y_AY_B} = -(\kappa_r sin\phi + \kappa_i cos\phi)$$

$$A_{Y_A\phi} = Y_B(\kappa_i sin\phi - \kappa_r cos\phi)$$

$$A_{Y_AM_A} = \frac{Y_A}{2\tau_p}$$

$$A_{Y_BY_A} = \kappa_r sin\phi - \kappa_i cos\phi$$

$$A_{Y_BY_B} = \frac{1}{2\tau_p}(M_B - 1)$$

$$A_{Y_B\phi} = Y_A(\kappa_r cos\phi + \kappa_i sin\phi)$$

$$A_{Y_BM_B} = \frac{Y_B}{2\tau_p}$$

$$A_{\phi Y_A} = \frac{\kappa_r cos\phi + \kappa_i sin\phi}{Y_B} + \frac{Y_B}{Y_A^2}(\kappa_r cos\phi - \kappa_i sin\phi)$$

$$A_{\phi Y_B} = \frac{-\kappa_r cos\phi + \kappa_i sin\phi}{Y_A} - \frac{Y_A}{Y_B^2}(\kappa_r cos\phi + \kappa_i sin\phi)$$

$$A_{\phi\phi} = -\kappa_r sin\phi\left(\frac{Y_A}{Y_B} - \frac{Y_B}{Y_A}\right) + \kappa_i cos\phi\left(\frac{Y_A}{Y_B} + \frac{Y_B}{Y_A}\right)$$

$$A_{\phi M_A} = \frac{\alpha_H}{2\tau_p}$$

$$A_{\phi M_B} = -\frac{\alpha_H}{2\tau_p}$$

$$A_{M_A Y_A} = -\frac{2M_A Y_A}{\tau_N}$$

$$A_{M_A M_A} = -\frac{1 + Y_A^2}{\tau_N}$$

$$A_{M_B Y_B} = -\frac{2M_B Y_B}{\tau_N}$$

$$A_{M_B M_B} = -\frac{1 + Y_B^2}{\tau_N}$$

For a steady state solution to be stable, all eigenvalues of $\overline{\overline{\boldsymbol{A}}}$ need to have negative real parts. By evaluating the eigenvalues of $\overline{\overline{\boldsymbol{A}}}$ we can check the stability of the steady-state solutions that we have previously obtained in Chapter 3. Eigenvalues of $\overline{\overline{\boldsymbol{A}}}$ are also the poles in the small-signal modulation response.

4.2 Stability of the steady-state solutions

As an example and a validation for our approach to the array stability, we calculate the array stability under $\Delta\Omega = 0$, $Q_A = Q_B = Q$, because this is the situation that has been previously solved analytically [2]. We first solve SSCREs with $\Delta\Omega$ and $Q_{A,B}$ as the input, and $(Y_{A,B}, \phi, M_{A,B})$ as outputs. Then from the steady-state solutions $(Y_{A,B}, \phi, M_{A,B})$ we evaluate $\overline{\overline{\boldsymbol{A}}}$ and calculate the eigenvalues of $\overline{\overline{\boldsymbol{A}}}$. If all the eigenvalues of $\overline{\overline{\boldsymbol{A}}}$ have negative real parts, then the steady-state solution is stable. Otherwise, if there exist eigenvalue(s) of $\overline{\overline{\boldsymbol{A}}}$ that have positive real part, the steady-state solution is unstable (i.e., random small perturbations will blow up over time) [6].

We first validate our calculation against a case that has been analytically solved: $\Delta\Omega = 0$ and $Q_A = Q_B = Q$. The stability condition of in-phase and out-of-phase modes are [2]:

$$\kappa > \frac{\alpha_H}{\tau_p}\frac{Q-1}{2Q} \text{ (in-phase)} \tag{4.2}$$

$$\kappa < \frac{Q}{2\alpha_H \tau_N} \text{ (out-of-phase)} \tag{4.3}$$

The stability maps (for the in-phase and the out-of-phase mode respectively) are plotted in Figure 4.1, where the yellow region represents stable and the blue region represents unstable. The analytical expressions [Equations (4.2) and (4.3)] are shown as red dashed lines, and we see excellent agreement.

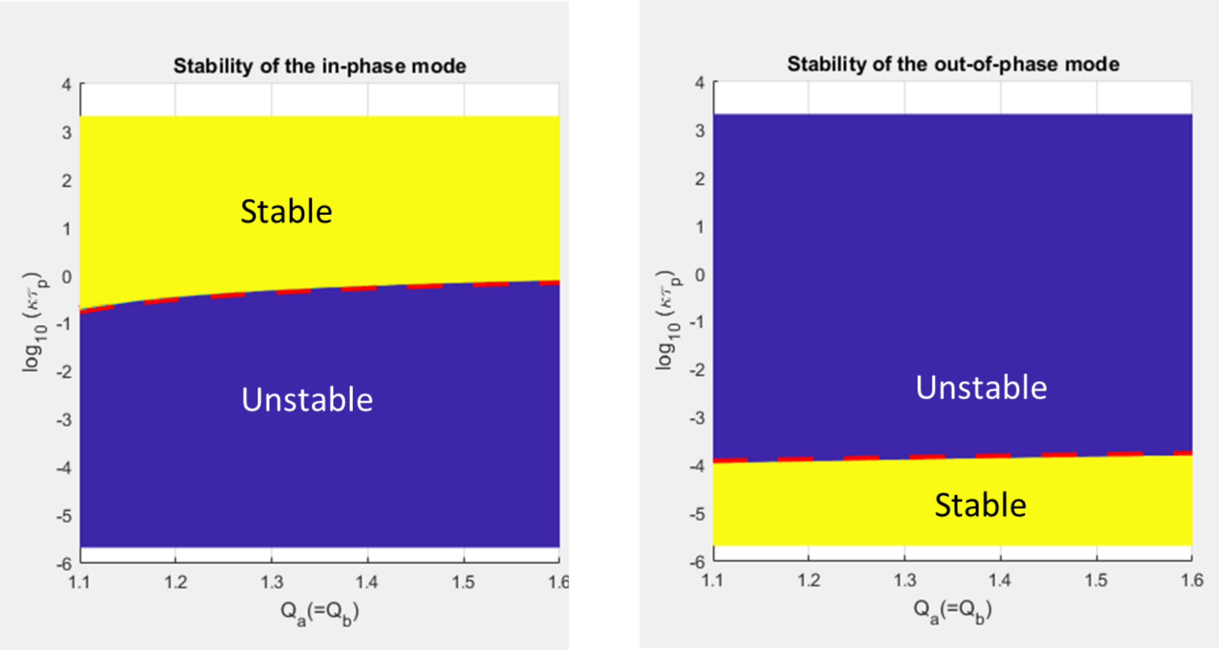

Figure 4.1: Stability of the array under zero detuning and equal injection ($\Delta\Omega = 0$, $Q_A = Q_B = Q$). The yellow region is where the array is stable, while the blue region is where the array is unstable. The horizontal axis is the common pump parameter Q and the vertical axis is the strength of the coupling ($\kappa\tau_p$) in logarithmic scale. The red dashed lines are the analytical criteria [Equations (4.1) and (4.2)] from [2].

4.3 Small-signal response under external current modulation

With external small-signal modulation of the input current(s), we have nonzero ΔQ_A and/or ΔQ_B. For a sinusoidal modulation at frequency ω_m, we have

$$\Delta Q_A(t) = Q_{Am} e^{-i\omega_m t}$$

$$\Delta Q_B(t) = Q_{Bm} e^{-i\omega_m t}$$

$$\Delta Y_A(t) = Y_{Am} e^{-i\omega_m t}$$

$$\Delta Y_B(t) = Y_{Bm} e^{-i\omega_m t}$$

$$\Delta \phi(t) = \phi_m e^{-i\omega_m t}$$

$$\Delta M_A(t) = M_{Am} e^{-i\omega_m t}$$

$$\Delta M_B(t) = M_{Bm} e^{-i\omega_m t}$$

and hence we have $\frac{d}{dt} \rightarrow -i\omega_m$. Note that ω_m in this situation is the frequency of the temporal evolution of the perturbation rather than the frequency of the optical mode (which is ω).

Replacing $\frac{d}{dt}$ with $-i\omega_m$, we have

$$-i\omega_m \begin{bmatrix} Y_{Am} \\ Y_{Bm} \\ \phi_m \\ M_{Am} \\ M_{Bm} \end{bmatrix} e^{-i\omega_m t} = \bar{\bar{\boldsymbol{A}}} \begin{bmatrix} Y_{Am} \\ Y_{Bm} \\ \phi_m \\ M_{Am} \\ M_{Bm} \end{bmatrix} e^{-i\omega_m t} + \frac{1}{\tau_N} \begin{bmatrix} 0 \\ 0 \\ 0 \\ Q_{Am} \\ Q_{Bm} \end{bmatrix} e^{-i\omega_m t}$$

which yields

$$\left(\bar{\bar{\boldsymbol{A}}} + i\omega_m \bar{\bar{I}}\right)\bar{x} = -\frac{1}{\tau_N}\bar{J}$$

where $\bar{\bar{I}}$ is the identity matrix, and

$$\bar{x} \equiv \begin{bmatrix} Y_{Am} \\ Y_{Bm} \\ \phi_m \\ M_{Am} \\ M_{Bm} \end{bmatrix}$$

$$\bar{J} \equiv \begin{bmatrix} 0 \\ 0 \\ 0 \\ Q_{Am} \\ Q_{Bm} \end{bmatrix}$$

Using Cramer's rule, we can solve for the magnitude of the electric field perturbation in cavity A, $\mathrm{Y_{Am}}$:

$$\mathrm{Y_{Am}} = -\frac{1}{\tau_{\mathrm{N}}\Lambda}\begin{vmatrix} 0 & A_{Y_AY_B} & A_{Y_A\phi} & A_{Y_AM_A} & 0 \\ 0 & A_{Y_BY_B} + i\omega & A_{Y_B\phi} & 0 & A_{Y_BM_B} \\ 0 & A_{\phi Y_B} & A_{\phi\phi} + i\omega & A_{\phi M_A} & A_{\phi M_B} \\ Q_{Am} & 0 & 0 & A_{M_AM_A} + i\omega & 0 \\ Q_{Bm} & A_{M_BY_B} & 0 & 0 & A_{M_BM_B} + i\omega \end{vmatrix}$$

where

$$\Lambda \equiv \left|\bar{\bar{\boldsymbol{A}}} + i\omega\bar{\bar{I}}\right| = \begin{vmatrix} A_{Y_AY_A} + i\omega & A_{Y_AY_B} & A_{Y_A\phi} & A_{Y_AM_A} & 0 \\ A_{Y_BY_A} & A_{Y_BY_B} + i\omega & A_{Y_B\phi} & 0 & A_{Y_BM_B} \\ A_{\phi Y_A} & A_{\phi Y_B} & A_{\phi\phi} + i\omega & A_{\phi M_A} & A_{\phi M_B} \\ A_{M_AY_A} & 0 & 0 & A_{M_AM_A} + i\omega & 0 \\ 0 & A_{M_BY_B} & 0 & 0 & A_{M_BM_B} + i\omega \end{vmatrix}$$

Similarly, we can solve for the magnitudes of the perturbations in the electric field in cavity B (Y_{Bm}), in the relative phase between cavities (ϕ_m), and in the carrier densities ($M_{Am,Bm}$)

$$\mathrm{Y_{Bm}} = -\frac{1}{\tau_{\mathrm{N}}\Lambda}\begin{vmatrix} A_{Y_AY_A} + i\omega & 0 & A_{Y_A\phi} & A_{Y_AM_A} & 0 \\ A_{Y_BY_A} & 0 & A_{Y_B\phi} & 0 & A_{Y_BM_B} \\ A_{\phi Y_A} & 0 & A_{\phi\phi} + i\omega & A_{\phi M_A} & A_{\phi M_B} \\ A_{M_AY_A} & Q_{Am} & 0 & A_{M_AM_A} + i\omega & 0 \\ 0 & Q_{Bm} & 0 & 0 & A_{M_BM_B} + i\omega \end{vmatrix}$$

$$\phi_{\mathrm{m}} = -\frac{1}{\tau_{\mathrm{N}}\Lambda}\begin{vmatrix} A_{Y_AY_A} + i\omega & A_{Y_AY_B} & 0 & A_{Y_AM_A} & 0 \\ A_{Y_BY_A} & A_{Y_BY_B} + i\omega & 0 & 0 & A_{Y_BM_B} \\ A_{\phi Y_A} & A_{\phi Y_B} & 0 & A_{\phi M_A} & A_{\phi M_B} \\ A_{M_AY_A} & 0 & Q_{Am} & A_{M_AM_A} + i\omega & 0 \\ 0 & A_{M_BY_B} & Q_{Bm} & 0 & A_{M_BM_B} + i\omega \end{vmatrix}$$

$$M_{Am} = -\frac{1}{\tau_N \Lambda} \begin{vmatrix} A_{Y_A Y_A} + i\omega & A_{Y_A Y_B} & A_{Y_A \phi} & 0 & 0 \\ A_{Y_B Y_A} & A_{Y_B Y_B} + i\omega & A_{Y_B \phi} & 0 & A_{Y_B M_B} \\ A_{\phi Y_A} & A_{\phi Y_B} & A_{\phi\phi} + i\omega & 0 & A_{\phi M_B} \\ A_{M_A Y_A} & 0 & 0 & Q_{Am} & 0 \\ 0 & A_{M_B Y_B} & 0 & Q_{Bm} & A_{M_B M_B} + i\omega \end{vmatrix}$$

$$M_{Bm} = -\frac{1}{\tau_N \Lambda} \begin{vmatrix} A_{Y_A Y_A} + i\omega & A_{Y_A Y_B} & A_{Y_A \phi} & A_{Y_A M_A} & 0 \\ A_{Y_B Y_A} & A_{Y_B Y_B} + i\omega & A_{Y_B \phi} & 0 & 0 \\ A_{\phi Y_A} & A_{\phi Y_B} & A_{\phi\phi} + i\omega & A_{\phi M_A} & 0 \\ A_{M_A Y_A} & 0 & 0 & A_{M_A M_A} + i\omega & Q_{Am} \\ 0 & A_{M_B Y_B} & 0 & 0 & Q_{Bm} \end{vmatrix}$$

From these equations we can extract the small signal frequency response when either one of the injection currents is modulated or when both currents are modulated. When one of the lasers is under small signal current modulation, we set $Q_{Bm} = 0$ and calculate $|\frac{Y_{Am}}{Q_{Am}}|$ and $|\frac{Y_{Bm}}{Q_{Am}}|$. Most conveniently the small signal response is found by determining the poles and zeros of Y_{Am} and Y_{Bm} numerically.

4.4 Stability and modulation response at the exceptional points

At the exceptional points (assuming that $\kappa_i = 0$), the steady-state solution is:

$$\phi = \pm\frac{\pi}{2}$$

$$Y_A = Y_B = Y$$

$$M_A = 1 \pm 2\tau_p \kappa_r$$

$$M_B = 1 \mp 2\tau_p \kappa_r$$

which leads to

$$A_{Y_A Y_A} = A_{Y_B Y_A} = \pm\kappa_r$$

$$A_{Y_A Y_B} = A_{Y_B Y_B} = \mp\kappa_r$$

$$A_{Y_A M_A} = A_{Y_B M_B} = \frac{Y}{2\tau_p}$$

$$A_{\phi M_A} = \frac{\alpha_H}{2\tau_p}$$

$$A_{\phi M_B} = -\frac{\alpha_H}{2\tau_p}$$

$$A_{M_A Y_A} = -\frac{2(1 \pm 2\tau_p \kappa_r)Y}{\tau_N}$$

$$A_{M_B Y_B} = -\frac{2(1 \mp 2\tau_p \kappa_r)Y}{\tau_N}$$

$$A_{M_A M_A} = A_{M_B M_B} = -\frac{1 + Y^2}{\tau_N}$$

$$A_{Y_A \phi} = A_{Y_B \phi} = A_{\phi Y_A} = A_{\phi Y_B} = A_{\phi\phi} = 0$$

and hence

$$\bar{\bar{\boldsymbol{A}}} = \begin{bmatrix} \pm\kappa_r & \mp\kappa_r & 0 & \frac{Y}{2\tau_p} & 0 \\ \pm\kappa_r & \mp\kappa_r & 0 & 0 & \frac{Y}{2\tau_p} \\ 0 & 0 & 0 & \frac{\alpha_H}{2\tau_p} & -\frac{\alpha_H}{2\tau_p} \\ -\frac{2(1 \pm 2\tau_p \kappa_r)Y}{\tau_N} & 0 & 0 & -\frac{1+Y^2}{\tau_N} & 0 \\ 0 & -\frac{2(1 \mp 2\tau_p \kappa_r)Y}{\tau_N} & 0 & 0 & -\frac{1+Y^2}{\tau_N} \end{bmatrix}$$

At the exceptional pint, it can be observed that $\bar{\bar{\boldsymbol{A}}}$ is a singular matrix ($|\bar{\bar{\boldsymbol{A}}}| = 0$). The eigenvectors of singular matrix $\bar{\bar{\boldsymbol{A}}}$ are thus not unique, as we can always add $[0, 0, x, 0, 0]^T$ to any eigenvector and it would still be an eigenvector. In the future, it will be interesting to study the consequence of this singularity at the exceptional points by examination of the asymptotic behavior of the array as it approaches an exceptional point.

4.5 References

[1] Z. Gao, M. T. Johnson, and K. D. Choquette, "Rate equation analysis and non-Hermiticity in coupled semiconductor laser arrays," *Journal of Applied Physics,* vol. 123, no. 17, p. 173102, 2018.

[2] H. G. Winful and S. S. Wang, "Stability of phase locking in coupled semiconductor-laser arrays," *Applied Physics Letters,* vol. 53, no. 20, pp. 1894-1896, 1988.

[3] Y. Kominis, V. Kovanis, and T. Bountis, "Controllable asymmetric phase-locked states of the fundamental active photonic dimer," *Physical Review A,* vol. 96, no. 4, p. 043836, 2017.

[4] S. L. Chuang, *Physics of Photonic Devices*, 2nd ed. (Wiley series in pure and applied optics). Hoboken, N.J.: John Wiley & Sons, 2009.

[5] L. A. Coldren, S. W. Corzine, and M. L. Mashanovitch, *Diode Lasers and Photonic Integrated Circuits*. John Wiley & Sons, 2012.

[6] M. C. Pease, *Methods of Matrix Algebra* (Mathematics in science and engineering, no. 16). New York: Academic Press, 1965.

CHAPTER 5: EXPERIMENTAL STUDY OF THE 2 × 1 COUPLED VCSEL ARRAYS

In this chapter we describe the experimental study of 2 × 1 coherently coupled VCSEL arrays. Coherently coupled semiconductor laser arrays have been experimentally studied for almost 5 decades [1-7]. At the University of Illinois, 2 × 1 coherently coupled VCSEL arrays have been studied both experimentally and theoretically for more than a decade [5, 7-18]. The VCSEL device designs presented here have benefited from inherited parameters determined from the exploration and optimization by prior students in the Photonics Device Research Group, not only from the study of coherently coupled VCSEL arrays, but also from single ion-implanted photonic crystal (PhC) VCSELs [19-22].

We first introduce the design and fabrication of an optically coupled electrically isolated 2x1 VCSEL array [16, 23-25]. Next, we will discuss the experimental characterization of the arrays at room temperature and under continuous wave (CW) operation. Comprehensive characterizations of the mode tuning behavior via independent control of both injection currents (I_A and I_B) are the primary experimental result [24]. Electronic steering of the far field emission angle is observed, as a consequence of the gain/loss tuning (non-Hermiticity) in the array. Optical power versus injection currents (L-I) and far-field intensity profiles are measured in a two-dimensional fashion (at every combination of I_A and I_B) using LabVIEW automation. Near-field intensity profiles and optical spectra are also measured at locations of interest.

Extraction of the coupling coefficient from experimental measurements has long been of interest, and is discussed here in Section 5.4. Lastly, we present experimental results on controlling the mode tuning behavior with designed asymmetrical arrays [24, 25]. The degree of asymmetry serves as an additional array control parameter, in addition to the current tuning.

5.1 Design and fabrication

An example cross-sectional sketch and top image are shown in Figure 5.1 of a 2 x 1 coherently coupled VCSEL array that has been designed, fabricated, and characterized at the University of Illinois. The optical cavities of the two lasers are defined by the two epitaxial distributed Bragg reflector (DBR) mirrors in the longitudinal direction and by the PhCs in the transverse direction. The PhC pattern is a hexagonal lattice of etched holes with b/a ratio of 0.6, where b is the diameter of the holes and a is the center-to-center distance between nearest holes [22, 26]. A single missing PhC hole in the hexagonal pattern forms a cavity. The etched holes in PhC patterns reduce the effective index surrounding the cavity and offer index confinement, similar to the PhC fibers [27]. In addition, the PhCs introduce scattering loss in the cladding area, which offers loss-induced confinement and suppression of the higher-order modes [21], all of which enable single-fundamental-mode lasing operation in an individual PhC VCSEL [28]. The center-to-center distance between the two cavities is $\sqrt{3}a$. The two holes in the coupling region (between the two cavities) are reduced in diameter (and because of their smaller diameter, they are also etched shallower during ICP-RIE) to enhance the lateral coupling [8, 20]. The nominal diameter of the normal holes is $b = 3$ µm, while the nominal diameter of the reduced holes is 2 µm. Note that the “nominal diameter” represents the diameter in the mask design. The actual diameters of holes for the fabricated devices are typically smaller than the nominal values due to imperfect pattern transformation during photolithography and etching.

The electrical apertures which confine the injected currents into the array elements are defined by multiple steps of proton-implantations at various acceleration energies (100 keV to 330 keV) and oxygen-implantation (50 keV to 300 keV) [29]. The nominal diameter of the implantation apertures is 7 µm, which equals to the nominal optical aperture formed by the PhC defect ($2a - b = 7$ μm). The actual diameters of the implant apertures tend to be smaller than those on the photomask, because of the oblique sidewall of photoresist mask and the lateral scattering (straggle) of the implanted ions. To increase the overlap between the un-implanted cavity and the top anode electrode (to reduce series resistance), we increase the implant aperture overlap over the anode electrode to ~4 μm by extending the un-implanted area underneath the anodes. The injection currents into each cavity, I_A and I_B, can be individually tuned, with typically > 1 MΩ electrical isolation between the two top anode electrodes. Polyimide planarization is used to position both the anode and cathode contacts at the top surface with large contact pads for easier and more consistent on-wafer probing. Multiple VCSEL array samples emitting nominally at 850nm have been fabricated using the semiconductor processing tools within the Micro and Nanotechnology Laboratory at the University of Illinois. A complete fabrication process Follower is disclosed in Appendix E.

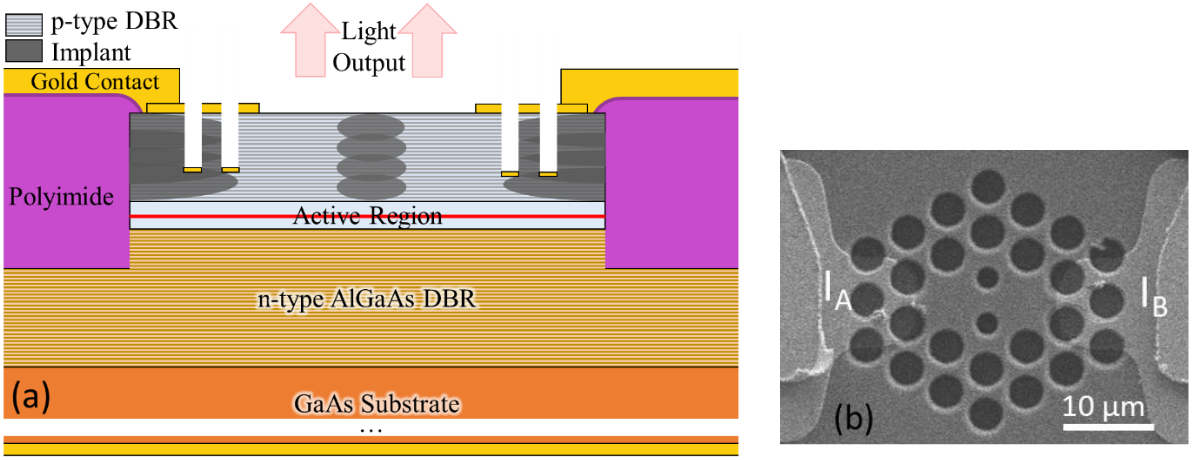

Figure 5.1: (a) Cross-sectional sketch and (b) scanning electron microscopy image of a 2 x 1 coherent VCSEL array.

5.2 Characterization

Because the array injection currents I_A and I_B can be individually and independently tuned, all 2 x 1 VCSEL array characterizations can be represented with 2D graphs with I_A and I_B

as the two coordinate axes, and the measured quantity represented by a color scale. For example, Figure 5.2(a) is a 2D representation of the L-I characterization where the x- and y-axis represent I_A and I_B, and the color scale represents the output optical power at a specific combination of (I_A, I_B). Because of the large parameter space (and the need to sometimes perform high resolution scans), measurements have been automated with a LabVIEW program controlling two Keithley 236 precision current sources and recording the measurements (or one Keithley and one semiconductor parametric analyzer in the case of L-I characterizations).

The injection currents vary the carrier injection rates ($Q_{A,B}$) into the cavities, and also they tune the resonance frequencies of the cavities ($\Omega_{A,B}$) through Joule heating and the temperature dependence of refractive index in semiconductors. The cavity frequency detuning ($\Delta\Omega = \Omega_B - \Omega_A$) varies linearly with $\Delta I = I_B - I_A$, as evident in Figure 5.2(d). From the coupled rate equation analysis presented in Chapter 3, we know that if we want the VCSEL array to lase in a coherent coupled mode, their frequency detuning has to be within $\Delta\Omega \lesssim |\kappa_i + \alpha_H \kappa_r|$ [30, 31]. When the two VCSELs are coherently coupled (phase-locked), the relative phase between two cavities is controlled by $\Delta\Omega$.

When the two lasers are phase-locked, we can also say that the two lasers lase in a single coherent supermode [14]. The single coherent supermode which extends into both optical cavities, is more efficiently pumped than two independent and incoherent individual modes. Evidence of this can be seen along the diagonal of Figure 2(a) above the lasing threshold. Note the “ridge” of increased output power and the decrease in threshold that occurs when the two currents are approximately equal. This increase in output power and decrease in lasing threshold when coherently coupled is evidence of an imaginary component in the coupling coefficient (non-Hermitian coupling), which will be discussed in Section 5.4.

When the lasers are phase-locked, we observe an interference pattern in the far field. The visibility of the interference pattern, defined as $visibility = \frac{I_{max}-I_{min}}{I_{max}+I_{min}}$, is approximately the magnitude of the mutual coherence between the two lasers when their individual intensities are not too different [32]. Unitary visibility corresponds to perfect mutual coherence while zero visibility implies completely incoherent and spatially separate modes. Visibility between zero and one is partial coherence, which can arise as a result of the coexistence of in-phase and out-of-phase coupled modes [7, 10]. We plot the far-field interference visibility versus the two injection currents in Figure 5.2(b) which clearly elucidates the locking region along the diagonal of the plot where the interference visibility approaches 1. Within the locking region, the relative phase between the two lasers can be tuned by the injection currents, leading to beam steering [13]. Shown in Figure 5.2(c) is the plot of beam steering angle (angle of the far-field intensity maximum) versus injection currents. Note that at higher bias levels, beam steering becomes much more sensitive to the current tuning, compared to near threshold. The different beam steering behavior near threshold versus at higher bias levels is discussed in detail in Section 5.3.

The array lasing wavelength is measured using an optical spectrum analyzer (OSA) with 0.02 nm spectral resolution. Shown in Figure 5.2(d) is a plot of the lasing wavelength when I_A is fixed and I_B is varied through the locking region. Within the locking region, the spectrum shows single peak, corresponding to the coherent coupled mode, while outside of the locking region, the two lasers in the array lase in localized modes at distinct wavelengths [13, 14]. (However, we must note that in Figure 5.2(d), we know that the two lasers are mutually locked and emit mostly in a single coupled mode when $3.40\ \text{mA} < I_B < 3.64\ \text{mA}$ not because we see only one spectral peak, but because we performed far-field measurements at the same time, shown later in Figure 5.7. Spectral measurements with OSAs are often not a good characterization of the locking region, due to the low resolution of OSA not being able to resolve closely spaced lasing wavelengths when they are $\lesssim 0.08\ nm$ apart. This means that if the coupling coefficient is $\lesssim 10^{10}\ rad/s$, the OSA may show only one spectral peak when the two lasers have close but distinct lasing wavelength and are not coherently coupled, or if both the in-phase and out-of-phase modes lase simultaneously. The best way to characterize the locking region would be either the far-field visibility measurement or a fine spectral measurement with the frequency resolution at least $0.1 \times \frac{|\kappa|}{2\pi}$.)

The frequency tuning for both cavities apparent in Figure 5.2(d) mostly results from Joule heating and the temperature dependence of refractive index [33]. While increasing I_B mostly increases the temperature (and hence wavelength) of laser B in Figure 5.2(d), there is a small amount of thermal crosstalk evident in the wavelength shift of laser A. The cavity frequency detuning between the two cavities (i.e., $\Delta\Omega$), controlled by I_B in a linear fashion, is an important control parameter in coupled laser arrays. The cavity frequency detuning $\Delta\Omega$ determines the gain/loss contrast between the lasers through the nonlinearities in semiconductor cavities, as discussed in Chapter 3 [31]. From Figure 5.2(d), although we cannot resolve much detail within the locking region, we can very well determine $\Delta\Omega$ by linear extrapolation of the wavelength tuning that is measured unambiguously outside the locking region.

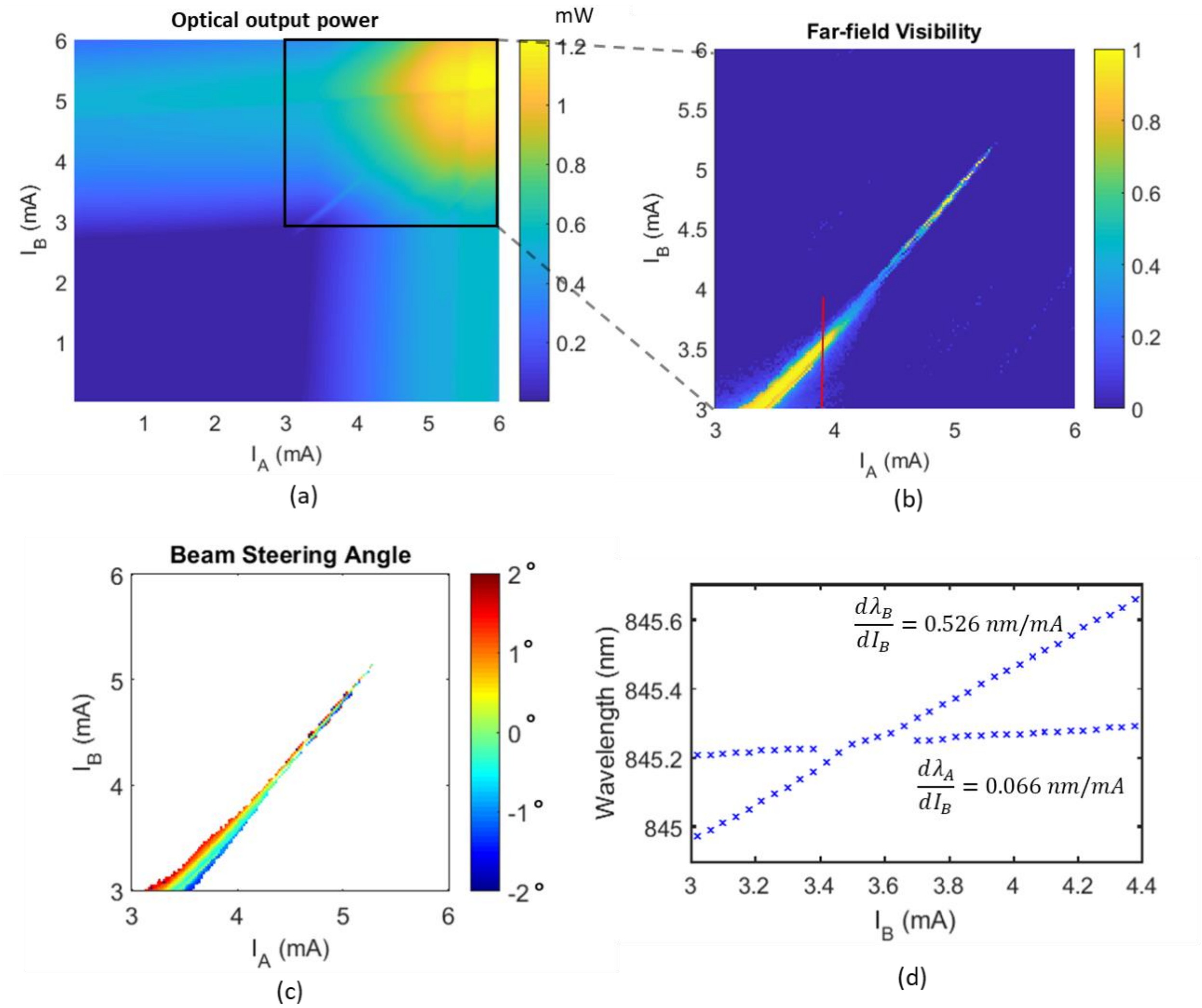

(a) (b) (c) (d)

Figure 5.2: Characterizations of a 2x1 VCSEL array emitting at 850 nm. (a) Output power versus injection currents (L-I). (b) Far-field interference fringe visibility versus injection currents. (c) Beam steering angle (of far-field intensity maximum) versus injection currents. (d) Lasing wavelength versus injection current I_B, while I_A is fixed at 3.9 mA. The red line in (b) labels where the spectral measurement in (d) was taken. In (c), the beam steering angle is plotted only when the far field visibility is > 0.2, otherwise the area is plotted as white. The steering direction towards laser B is defined as positive angle.

5.3 Experimental observation of non-Hermiticity

As discussed in Chapter 2, coupled VCSEL arrays are intrinsically non-Hermitian in the sense that there is often gain/loss contrast between the two cavities ($\gamma_A \neq \gamma_B$), and the coupling coefficient could be non-Hermitian ($\kappa_{AB} \neq \kappa_{BA}^*$), either of which makes the coupling matrix $\bar{\bar{\mathbf{M}}}$

non-Hermitian ($\bar{\bar{\mathbf{M}}} \neq \bar{\bar{\mathbf{M}}}^{\dagger}$). Relative phase tuning between the two elements, resulting in beam steering, is a direct result of the non-uniform gain/loss profile in the array, which manifest as complex and non-Hermitian $\bar{\bar{\mathbf{M}}}$.

Extensive characterization of the optical modes has been conducted on multiple 2 x 1 coherent VCSEL arrays and 2D plots are obtained for L-I, far-field visibility, beam steering angle, and spectral data on frequency detuning, such as shown in Figure 5.2. There are several observations that can be made. Close to lasing threshold, the injection current varies both the relative intensity and relative phase between cavities. However, at higher bias above threshold, the array shows only phase tuning without intensity tuning, and the lasing mode often switches between in-phase and out-of-phase around the phase tuning maxima. The coupling coefficient in the array decreases at higher bias levels, leading to the decrease of locking region and the increase of phase tuning sensitivity. The coupling coefficient in these coupled laser arrays may be a complex number due to gain splitting, which will be discussed in Section 5.4.

Different mode tuning behavior is observed when the array is biased near threshold versus at higher bias. First, the width of the locking region decreases with increasing bias level, as evident in Figure 5.2(b). Figure 5.3 illustrates the example of tuning of coherent mode when both lasers are biased near their thresholds ($\sim 1.1\ I_{th}$), while Figure 5.4 shows the tuning of coherent mode when both lasers are subject to higher bias levels ($\sim 1.4\ I_{th}$). The coherent mode can be expressed as $\bar{\boldsymbol{E}} = \begin{bmatrix} 1 \\ \sqrt{R}e^{i\phi} \end{bmatrix}$, where R is the near-field intensity ratio, and ϕ is the relative phase. From the near-field intensity measurements, we can extract R. From the relationship between far field and near field, we can also experimentally extract ϕ and the magnitude of mutual coherence [12]. The summary of $R,\ \phi$, and the degree of coherence is shown in Figures 5.3(b) and 5.4(b). Near threshold, both R and ϕ are found to be tuned by the current. At high bias currents, R is close to 1 and invariant against current tuning, consistent with coupled modes that resemble $\overline{\boldsymbol{E}} = \begin{bmatrix} 1 \\ e^{i\phi} \end{bmatrix}$ as predicted by PT symmetric non-Hermiticity. Under the bias condition labeled as (vii) in Figure 5.4, the array is at the exceptional point with $\overline{\boldsymbol{E}} = \begin{bmatrix} 1 \\ -i \end{bmatrix}$.

Comparing Figure 5.3 and Figure 5.4, we also see that the phase tuning is more sensitive to the current tuning at higher bias levels. Because the amount of frequency detuning induced by current tuning is measured to be almost the same between low bias and high bias ($\Delta\lambda/\Delta I = 0.460\ \mathrm{nm/mA}$ near 3.8 mA and $0.468\ n\mathrm{m/mA\ near\ 5mA}$), the more sensitive phase tuning at higher bias suggests that the coupling coefficient is smaller at higher bias, which is consistent with the smaller locking region.

At high bias levels, we also observe that the lasing mode switches from a high coherence in-phase mode to a low coherence out-of-phase mode, for example near the exceptional point labeled as point (vii) in Figure 5.4. The decrease of coherence is likely due to multi-coherent-mode operation. The wavelength splitting between in-phase and out-of-phase mode is below the resolution of our OSA, so this multi-coherent-mode operation cannot be measured in spectral measurements. The launch of the second coherent mode is similar to the launch of higher order modes in individual VCSELs due to spatial hole burning [29]. The carriers that are not effectively depleted by the dominating coherent mode will accumulate and the extra carriers may start a secondary lasing mode. Like in the case of spatial hole burning, the launch of the secondary mode is observed at high injection currents, while being rare near threshold.

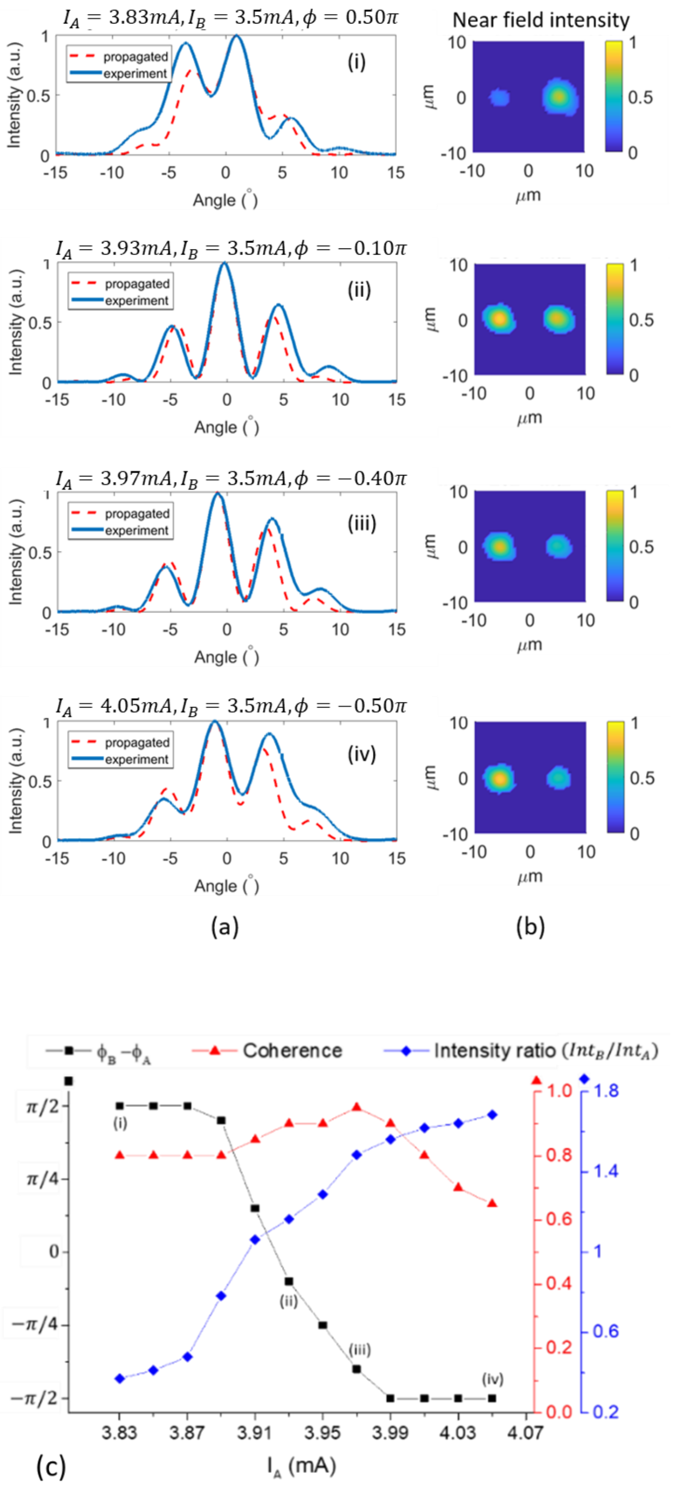

Figure 5.3: Tuning of the coherent mode near threshold (~1.1 I_{th}) with one injection current fixed and the other current varied. (a) Far field and (b) near field profiles tuned by the current. (c) Summary of extracted relative phase, degree of coherence, and near field intensity ratio.

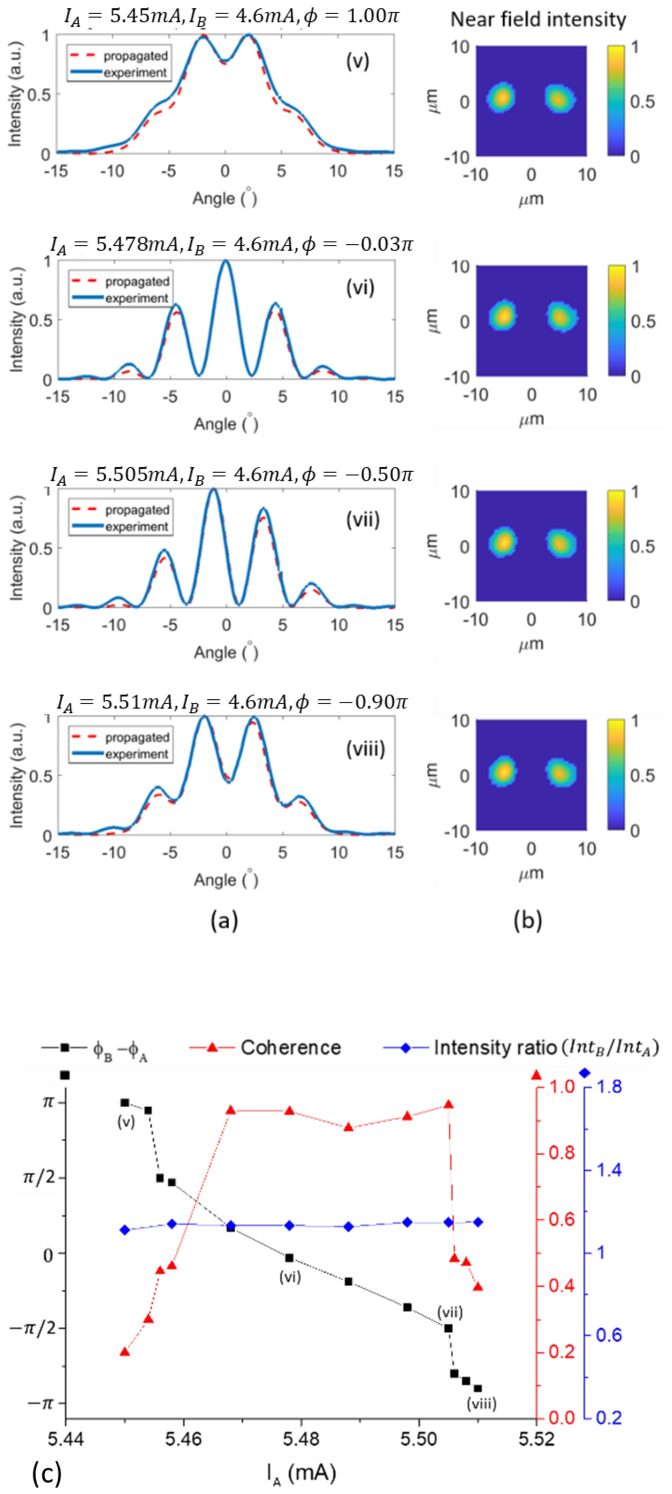

Figure 5.4: Tuning of the coherent mode at a higher bias above threshold (~1.4 I_{th}) with one injection current fixed and the other current varied. (a) Far field and (b) near field profiles tuned by the current. (c) Summary of extracted relative phase, degree of coherence, and near field intensity ratio.

In addition to the phase tuning and the non-Hermitian coupling that we have shown, we also observe modes with broken PT-symmetry ($\bar{\boldsymbol{E}} = \begin{bmatrix}1\\ \pm ie^{\mp\theta}\end{bmatrix}$, i.e., $Y_A \neq Y_B, \phi = \pm\pi/2$). The observed near-field and far-field measurements are compared to the theory in Figure 5.5 [17]. As discussed in Chapter 3, PT-symmetry breaking is relatively easy to achieve simply by driving ΔΩ to the boundary of the locking region, regardless of the values of $Q_{A,B}$.

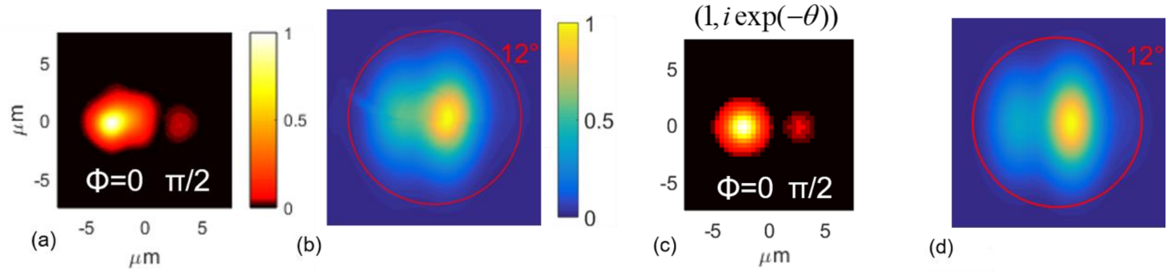

Figure 5.5: Measured (a) near field and (b) far field of the mode with broken PT-symmetry, compared with the simulated (c) near field and (d) far field of the $\bar{\boldsymbol{E}} = \begin{bmatrix}1\\ ie^{-\theta}\end{bmatrix}$ eigenmode [17].

5.4 Experimental extraction of the coupling coefficient

5.4.1 The existence of imaginary component in the coupling coefficient

The presence of an imaginary component in the coupling coefficient is evident in the 2D L-I characteristics of the arrays such as shown in Figure 5.2(a). The imaginary component κ_i represents the gain splitting between the in-phase and the out-of-phase supermodes, as discussed in Chapter 2. In coupled laser arrays, the gain splitting manifests as a difference in the lasing thresholds, which we refer to as “threshold splitting”, discussed using coupled rate equation analysis in Chapter 3. It was found in Chapter 3 that the amount of threshold splitting is proportional to the magnitude of κ_i:

$$M_{+}^{(\mathrm{th})} = 1 + 2\tau_p\kappa_i \tag{5.1}$$

$$\mathrm{M}_{-}^{(\mathrm{th})} = 1 - 2\tau_p\kappa_i \tag{5.2}$$

where $M_{+}^{(\mathrm{th})}$ ($\mathrm{M}_{-}^{(\mathrm{th})}$) is the dimensionless threshold carrier density of the in-phase (out-of-phase) coupled mode. Note that each individual laser has the threshold carrier density of $M_{A,B}^{(th)} = 1$. Because of the threshold splitting, the coupled array has lower threshold carrier density than the isolated lasers when the array is coherently coupled. In other words, *the coherent mode is more efficiently pumped than the incoherent modes.* This causes the output power of the array to show an increase due to the phase locking (coherent coupling), compared with the output power of the array when the two lasers are not coupled due to large frequency detuning. This increase in output power due to the decrease of threshold carrier density is visible on the 2D L-I graphs, for example in Figures 5.2(a) and 5.6.

L-I and visibility characteristics of two different arrays are compared in Figure 5.6. The L-I characteristics indicate different magnitudes of κ_i for the two arrays. Both arrays are in-phase coupled and have similar coherent regions. However, optical output of the left array in Figure 5.6(a) is less affected by the coupling, compared with the right array in Figure 5.6(b). The "ridge" in the L-I characteristics is less visible for the left array compared with the one on the right. This is an indication that the threshold splitting due to coupling is smaller for the left array and hence it has smaller κ_i. The power increase (or threshold decrease) due to coupling is more obvious in Figure 5.6 (b), suggesting larger κ_i for the right array. The change of threshold carrier density for the coupled array is

$$\Delta M \equiv M_{+}^{(th)} - M_{A,B}^{(th)} = 2\tau_p \kappa_i \tag{5.3}$$

The change of output power is proportional to the change of threshold, and it can be used κ_i:

$$|\kappa_i| \cong \frac{1}{2\tau_p}\frac{\Delta P}{h + P} \tag{5.4}$$

where P is the optical output power of the array, ΔP is the power increase due to coherent coupling, τ_p is the photon lifetime, h is a constant (with unit of W) that depends on the photon lifetime, carrier lifetime, and differential gain in the lasers. Equation (5.4) is a method for extracting the imaginary component in the coupling coefficient. The sign of κ_i is determined separately. When in-phase (out-of-phase) mode dominates, $\kappa_i < 0$ (> 0).

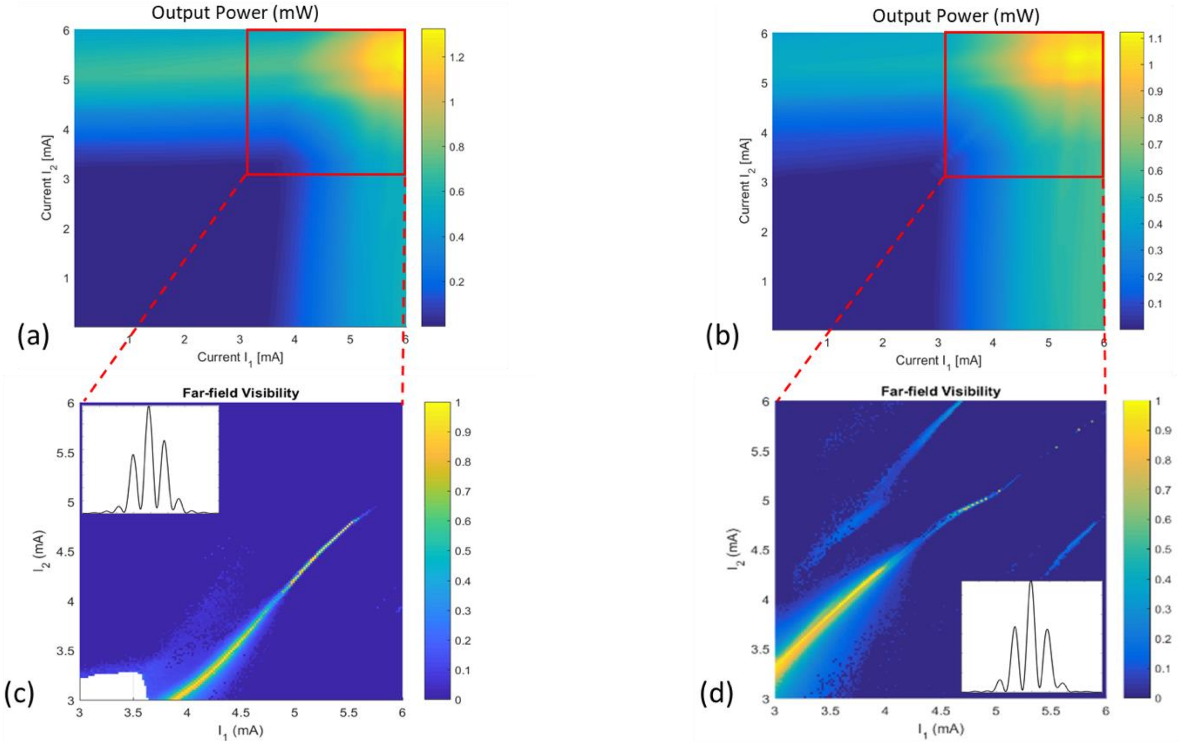

Figure 5.6: Comparison of two 2 x 1 VCSEL arrays. (a)-(b) L-I characteristics of two arrays (referred to as “left array” and “right array”) indicating different magnitudes of κ_i. (c)-(d) Far-field interference visibility maps of the two arrays and example far-field intensity profiles (insets), showing both arrays are in-phase coupled and have similar coherent regions. Different magnitudes of κ_i are evident from the fact the coupling region is less visible for the array in its L-I characteristics (a) and coherence locking range (c).

Origin of the imaginary component in the coupling coefficient is the non-uniform gain/loss profile in the coupled laser array, as discussed in Chapter 2. For example, gain in the coupling region introduces negative κ_i while loss in the coupling region introduces positive κ_i. This suggests that κ_i can be dynamically controlled if we can influence the carrier injection in the coupling region. For example in a 3x1 linear VCSEL array, we can use the middle element to control the coupling between the two outer elements [23].

5.4.2 Extraction of the coupling coefficient from mode tuning and mode stability

As we have studied in Chapter 3, the relative phase tuning that leads to beam steering is controlled by the cavity frequency detuning $\Delta\Omega$. With the coupling coefficient being complex in general, the phase tuning sensitivity [i.e. $\mathrm{d}\phi/d(\Delta\Omega)$] is governed by the factor $(\kappa_i + \alpha_H \kappa_r)$ [30]:

$$sin\phi \cong \frac{\Delta\Omega}{2(\kappa_i + \alpha_H \kappa_r)} \tag{5.5}$$

The factor $(\kappa_i + \alpha_H \kappa_r)$ can be extracted from the slope of phase tuning versus $\Delta\Omega$, since

$$(\kappa_i + \alpha_H \kappa_r) \cong \frac{1}{2} \frac{\mathrm{d}(\Delta\Omega)}{\mathrm{d}(\sin\phi)} \tag{5.6}$$

From the numerical simulations presented in Chapter 3, we find that Equation (5.6) holds not only for very weakly coupled arrays, but also for moderately weakly coupled arrays. Moreover, we find that most coupled VCSEL arrays have moderately weak coupling strength ($\kappa = 10^{10} \sim 10^{11} \mathrm{rad/s}$), as shown in the following calculation and in previous studies [13].

Figure 5.7 shows an example extraction of the coupling coefficient from the phase tuning measurements, performed on the same 2x1 coherent VCSEL array characterized in Figure 5.2. The coupling coefficient is extracted along the bias condition shown by the vertical red line in Figure 5.2(b). Hence I_A is fixed at 3.9 mA and I_B is tuned from 3.40 mA to 3.64 mA. The values of cavity frequency detuning $\Delta\Omega$ vary linearly with I_B, as extrapolated from the spectral measurements shown in Figure 5.2(d). We extract the relative phase between cavities $(\phi_B - \phi_A)$ and the magnitude of coherence from the near-field and far-field measurements [12], plotted in Figure 5.7. Only the four data points with almost perfect coherence (pure in-phase mode) are used in the extraction of coupling coefficient. From the slope in Figure 5.7(b), we extracted

$(\kappa_i + \alpha_H \kappa_r) \cong -3.8 \times 10^{10}$ rad/s. Note that the value of $(\kappa_i + \alpha_H \kappa_r)$ is negative. The sign of $(\kappa_i + \alpha_H \kappa_r)$ determines the beam steering direction, according to Equation (5.5).

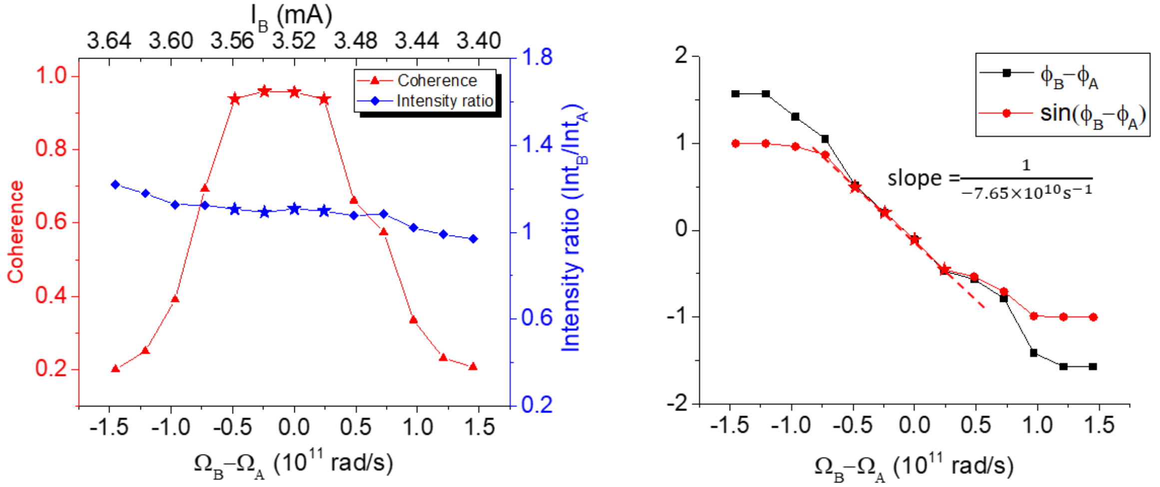

(a) (b)

Figure 5.7: Extraction of the coupling coefficient in the 2x1 coherent VCSEL array also depicted in Figure 5.2 using Equation (5.6): (a) degree of coherence and intensity ratio (Y_B^2/Y_A^2) versus $\Delta\Omega$ (and I_B); (b) $(\phi_B - \phi_A)$ and $\sin(\phi_B - \phi_A)$ versus $\Delta\Omega$. The measurement was done with I_A fixed and I_B varied from 3.40 mA t 3.64 mA [at the red line in Figure 5.2(b)]. The $\Delta\Omega = \Omega_B - \Omega_A$ value is obtained from the extrapolation in Figure 5.2(d). $\Delta\Omega$ varies linearly with I_B as evident in Figure 5.2(d).

One observation regarding the beam steering direction is that for the majority of the arrays we characterized, the direction of the output beam steers to the element with increasing current, no matter whether it is in-phase coupled or out-of-phase coupled, for example see Ref. [12]. This is somewhat surprising, because both the coupled mode theory and the coupled rate equations with real coupling coefficient suggest that the in-phase mode and out-of-phase mode should steer in opposite directions (see Chapters 2 and 3). Our tentative explanation for this phenomenon is that for in-phase arrays, $(\kappa_i + \alpha_H \kappa_r)$ is negative, while for out-of-phase arrays, $(\kappa_i + \alpha_H \kappa_r)$ is positive. The switch of sign in the term $(\kappa_i + \alpha_H \kappa_r)$ is due to the switch of sign in κ_i. For an array that naturally emits in the in-phase coherent mode, it is likely that the in-phase mode is preferred by the gain splitting and threshold splitting, which means $\kappa_i < 0$. On the other hand, for an array that emits in the out-of-phase coherent mode, the out-of-phase mode is preferred (in-phase mode suppressed), which translates to $\kappa_i > 0$. If $|\kappa_i| > |\alpha_H \kappa_r|$, then the sign of κ_i determines the overall sign of $(\kappa_i + \alpha_H \kappa_r)$, which in turn determines the beam steering direction. In our opinion, it is likely that the in-phase array and out-of-phase array often have $(\kappa_i + \alpha_H \kappa_r)$ of opposite signs (and that they often have $|\kappa_i| > |\alpha_H \kappa_r|$), which is the reason that the same beam steering direction is often found for both modes.

After extracting the quantity $(\kappa_i + \alpha_H \kappa_r)$ from the slope of the phase tuning relative to the frequency detuning, we still do not know the specific values of κ_i and $\alpha_H \kappa_r$. Further means to additionally constrain the values of κ_i and κ_r are necessary. We propose two approaches to determine the relative values of κ_i and κ_r. One way is to use Equation (5.4) to extract the value of κ_i from the degree of "active coupling" observed in the 2D L-I characterization, as discussed in Section 5.3. The other approach is to simulate the stability of the array and find out the combinations of κ_r and κ_i that produce a stable coupled mode.

5.5 Controlling the mode tuning behavior by introducing built-in asymmetry

As we have shown in the characterizations of the 2x1 VCSEL array, we can control the optical mode by tuning the injection currents $I_{A,B}$. However, this mode tuning is not ideal, because ideally we would want to individually control $Q_{A,B}$ and $\Delta\Omega$, which are the two independent control parameters for the array. Controlling two parameters with a single control dial (current tuning) limits us to a certain trajectory on the 2D parameter space of $(\Delta Q, \Delta\Omega)$, instead of being able to access the entire parameter space. This motivates us to introduce another control dial into the system as an addition to the current tuning. Here, we introduce built-in array asymmetry as the additional control parameter to engineer the mode tuning behavior. We consider what is introduced here a form of high-level mode engineering, since what is being engineered is not only the mode, but also the general behavior of how the modes are tuned.

We introduce built-in asymmetry into the index profile that defines the cavities of the elements, as evident in the lithographic mask designs, shown in Figure 5.8 [24, 25]. There are two types of asymmetries that are introduced in the 2x1 VCSEL arrays: asymmetry in the PhC patterns [Figure 5.8(a)] and asymmetry in ion-implantation aperture diameters [Figure 5.8(b)]. We denote the asymmetry in PhC holes by Δb and the asymmetry in ion-implantation diameters by ΔD. The degrees of asymmetry, Δb and ΔD, control the mode tuning behavior.

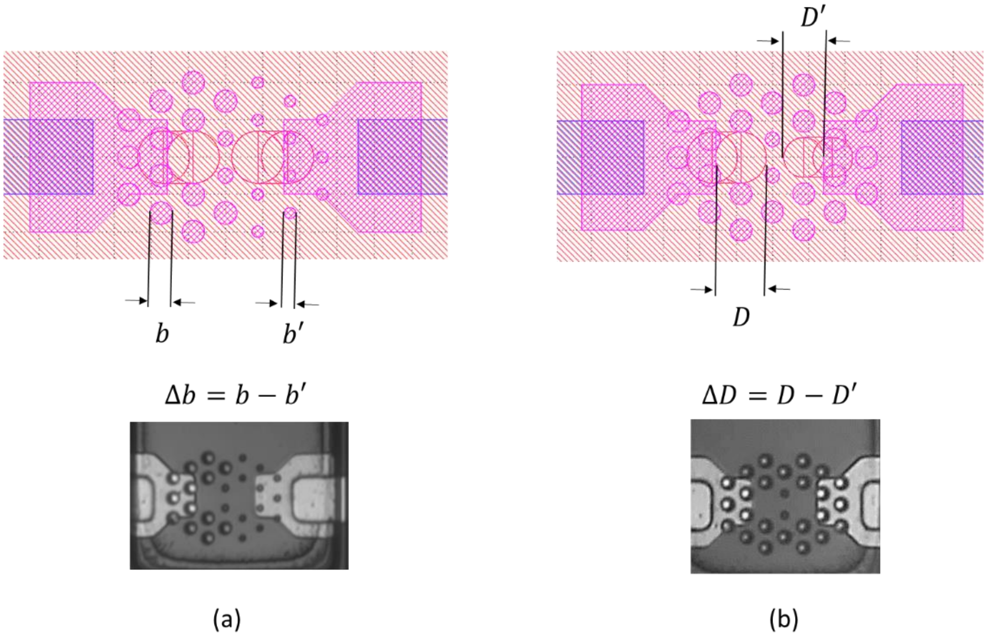

Figure 5.8: Designs of asymmetrical 2x1 VCSEL arrays. (a) Asymmetrical hole diameter in the PhC pattern. (b) Asymmetrical ion-implantation aperture diameters.

Shown in Figure 5.9 are the far-field visibility maps for three arrays with different degrees of asymmetry ($\Delta b = 0.15, 0, -0.2$ µm respectively). It is shown that the location of the high coherence region (coupling region) in the 2D plot is controlled by the degree of asymmetry Δb. In Figure 5.10, we plot the beam steering angle (the absolute value) versus I_A and I_B, and show that the tuning of beam steering angle is influenced by Δb as well. For a symmetrical array, the region with highest coherence (bright yellow region in the coherence map) is the region with normal-angle emission (dark blue region in the bear steering map); both are along the center of the high coherence region. However, in an asymmetrcal array, we often find that the modes with highest coherence are the beam-steered modes (with off-axis emission) instead of the $\phi = 0$ modes, as evident in Figure 5.10(d). No obvious influence was observed from implantation aperture diameter offset. Hence it appears that asymmetry in the photonic crystal structure, potentially is manifest as a means to control the coupling coefficient. Figure 5.10 suggests that variation in the effective refractive index profile surrounding the cavities in the array will influence the modal behavior such that asymmetric current injection creates the highest coherent single supermode.

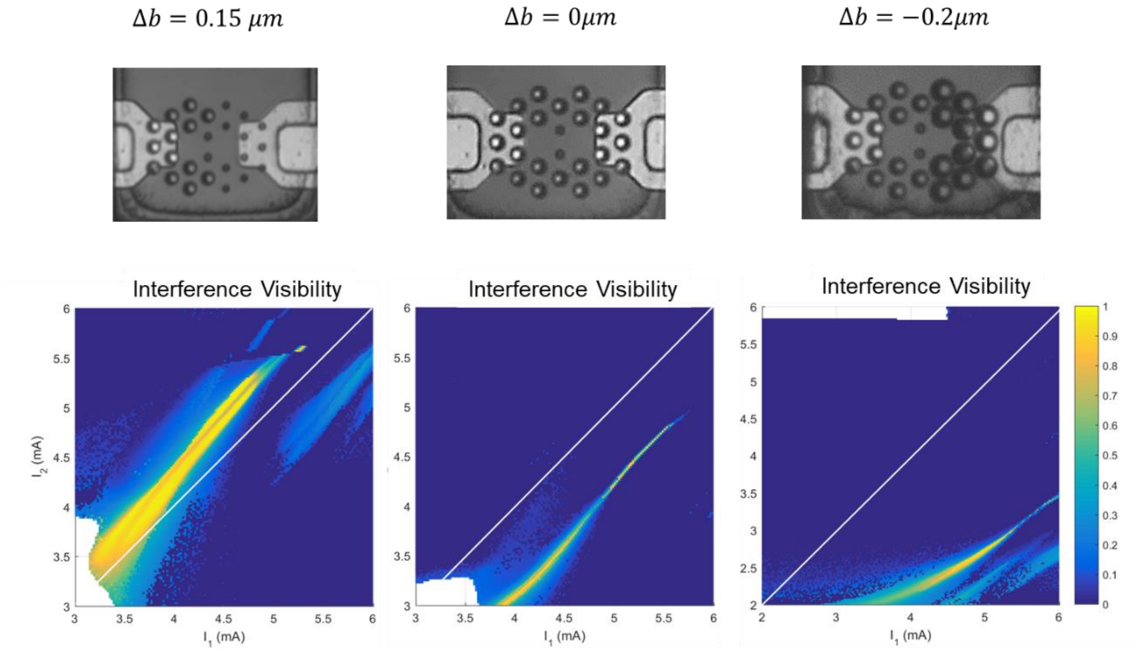

(a) (b) (c)

Figure 5.9: Controlling the location of coupling region with asymmetrical photonic crystal patterns with Δb equal to (a) 0.15 µm; (b) ≈ 0 µm; and (c) -0.2 µm.

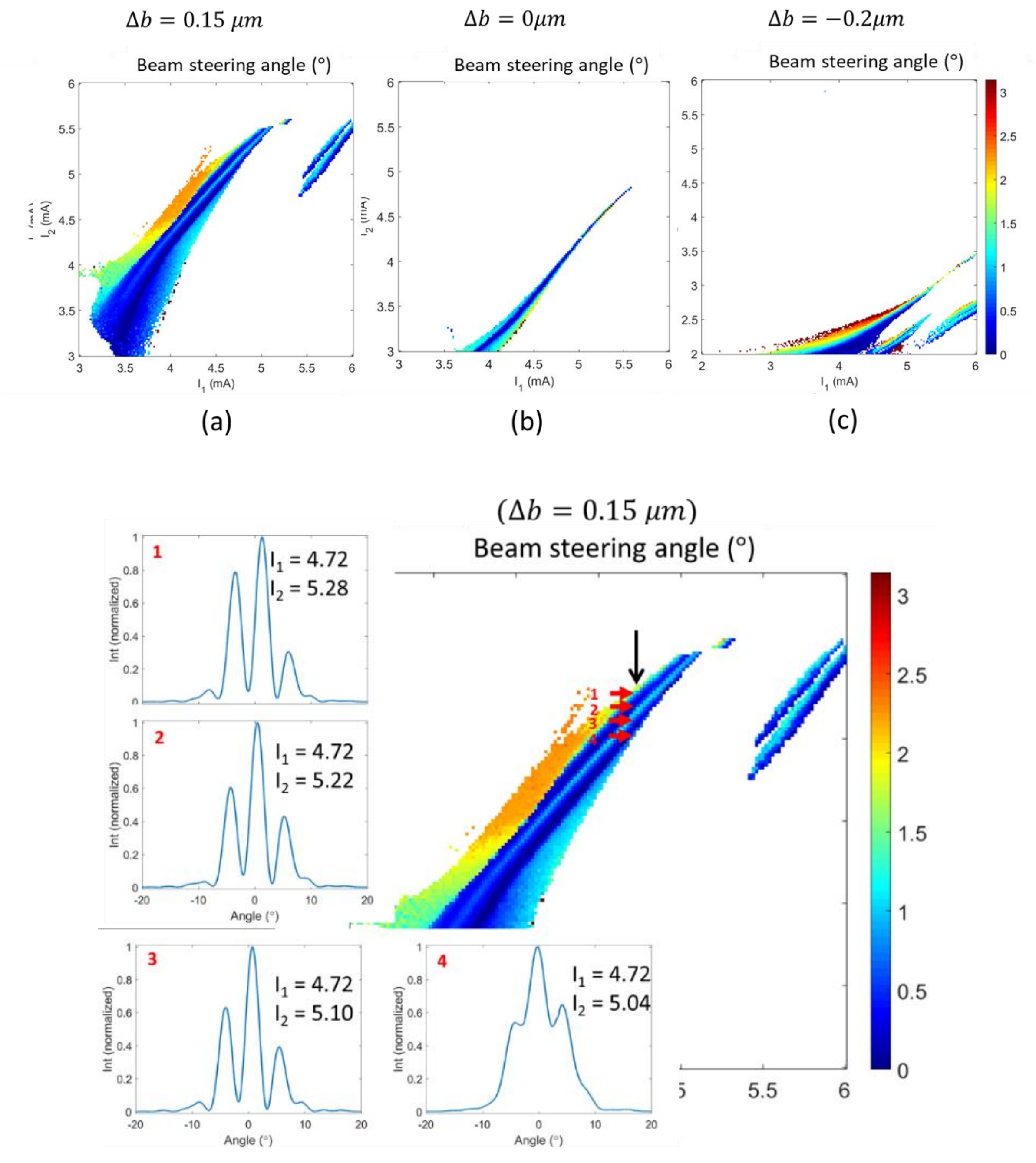

(a) (b) (c)

(d)

Figure 5.10: Absolute value of the beam steering angle versus I_A and I_B for (a) $\Delta b = 0.15$ µm; (b) $\Delta b = 0$; (c) $\Delta b = -0.2$ µm; (d) example far fields for $\Delta b = 0.15$ µm, showing that the array has high-coherence beam-steered modes and a low-coherence normal-angle mode, which is different from the modes of the symmetrical arrays.

5.6 Summary

In summary, we have characterized 2 × 1 coherently coupled VCSEL arrays by concise 2D characterizations, where the variable space is (I_A, I_B). The mode tuning behavior (i.e. the tuning of optical mode through variation of the current) is represented in 2D color graphs of optical output power, far-field interference visibility, and beam steering angle all as a function of (I_A, I_B). It is observed that the width of the high coherence region decreases with higher bias and the beam steering becomes more sensitive to the current tuning at higher bias, both suggesting that the coupling coefficient decreases with higher bias, because both the width of the phase-locking region and the beam steering sensitivity are controlled by $\alpha_i + \alpha_H \kappa_r$.

To study the different mode tuning behavior near threshold and high above threshold, we extract the coherent mode $\overline{\boldsymbol{E}} = \begin{bmatrix} 1 \\ \sqrt{R} e^{i\phi} \end{bmatrix}$ from the near-field and far-field measurements. It is shown that near threshold ($\sim$1.1 I_{th}), R and ϕ are simultaneously tuned by the injection currents, while at higher bias ($\sim$1.4 I_{th}) the modes resemble $\overline{\boldsymbol{E}} = \begin{bmatrix} 1 \\ e^{i\phi} \end{bmatrix}$, with ϕ being tuned and R fixed at 1. Moreover, we experimentally identify modes with broken PT-symmetry ($\overline{\boldsymbol{E}} = \begin{bmatrix} 1 \\ \pm i e^{\mp\theta} \end{bmatrix}$) and modes at the exceptional point ($\overline{\boldsymbol{E}} = \begin{bmatrix} 1 \\ \pm i \end{bmatrix}$).

We also extracted the coupling coefficient of the array around $I \sim 1.2\ I_{th}$ from the slope of beam steering angle versus the cavity frequency detuning and show that $(\kappa_i + \alpha_H \kappa_r) \cong -38 \times 10^9\ \mathrm{rad/s}$. As future work we outlined approaches to further determine the values of κ_i and κ_r separately. The existence of nonzero κ_i can be quantitatively examined from the power increase due to coupling in the 2D LI characteristics. Lastly, we showed that by introducing asymmetry in the design of coupled VCSEL arrays, the mode tuning behavior can be engineered.

The location of the coherence locking region can be shifted away from the diagonal in a controlled manner, and the beam steering behavior becomes asymmetrical too.

5.7 References

[1] J. E. Ripper and T. L. Paoli, "Optical coupling of adjacent stripe-geometry junction lasers," *Applied Physics Letters,* vol. 17, no. 9, pp. 371-373, 1970.

[2] D. R. Scifres, R. D. Burnham, and W. Streifer, "Phase-locked semiconductor-laser array," *Applied Physics Letters,* vol. 33, no. 12, pp. 1015-1017, 1978.

[3] E. Kapon, Z. Rav-Noy, L. T. Lu, M. Yi, S. Margalit, and A. Yariv, "Phase-locking characteristics of coupled ridge-waveguide InP/InGaAsP diode lasers," *Applied Physics Letters,* vol. 45, no. 11, pp. 1159-1161, 1984.

[4] L. J. Mawst *et al.*, "Resonant self-aligned-stripe antiguided diode-laser array," *Applied Physics Letters,* vol. 60, no. 6, pp. 668-670, 1992.

[5] A. J. Danner, J. C. Lee, J. J. Raftery, N. Yokouchi, and K. D. Choquette, "Coupled-defect photonic crystal vertical cavity surface emitting lasers," *Electronics Letters,* vol. 39, no. 18, pp. 1323-1324, 2003.

[6] L. D. A. Lundeberg and E. Kapon, "Mode switching and beam steering in photonic crystal heterostructures implemented with vertical-cavity surface-emitting lasers," *Applied Physics Letters,* vol. 90, no. 24, pp. 2005-2008, 2007.

[7] D. F. Siriani, P. S. Carney, and K. D. Choquette, "Coherence of leaky-mode vertical-cavity surface-emitting laser arrays," *IEEE Journal of Quantum Electronics,* vol. 47, no. 5, pp. 672-675, 2011.

[8] J. J. Raftery, A. C. Lehman, A. J. Danner, P. O. Leisher, A. V. Giannopoulos, and K. D. Choquette, "In-phase evanescent coupling of two-dimensional arrays of defect cavities in photonic crystal vertical cavity surface emitting lasers," *Applied Physics Letters,* vol. 89, no. 8, p. 081119, 2006.

[9] A. C. Lehman, J. J. Raftery, A. J. Danner, P. O. Leisher, and K. D. Choquette, "Relative phase tuning of coupled defects in photonic crystal vertical-cavity surface-emitting lasers," *Applied Physics Letters,* vol. 88, no. 2, p. 021102, 2006.

[10] D. F. Siriani, K. D. Choquette, and P. S. Carney, "Stochastic coupled mode theory for partially coherent laser arrays," *J Opt Soc Am A,* vol. 27, no. 3, pp. 501-508, 2010.

[11] D. F. Siriani and K. D. Choquette, "Implant defined anti-guided vertical-cavity surface-emitting laser arrays," *IEEE Journal of Quantum Electronics,* vol. 47, no. 2, pp. 160-164, 2011.

[12] M. T. Johnson, D. F. Siriani, J. D. Sulkin, and K. D. Choquette, "Phase and coherence extraction from a phased vertical cavity laser array," *Applied Physics Letters,* vol. 101, no. 3, p. 031116, 2012.

[13] M. T. Johnson, D. F. Siriani, M. P. Tan, and K. D. Choquette, "Beam steering via resonance detuning in coherently coupled vertical cavity laser arrays," *Applied Physics Letters,* vol. 103, no. 20, p. 201115, 2013.

[14] S. T. M. Fryslie, M. T. Johnson, and K. D. Choquette, "coherence tuning in optically coupled phased vertical cavity laser arrays," *IEEE Journal of Quantum Electronics,* vol. 51, no. 11, pp. 1-6, 2015.

[15] S. T. M. Fryslie, M. P. Tan, D. F. Siriani, M. T. Johnson, and K. D. Choquette, "37-GHz modulation via resonance tuning in single-mode coherent vertical-cavity laser arrays," *IEEE Photonics Technology Letters*, vol. 27, no. 4, pp. 415-418, 2015.

[16] S. T. M. Fryslie *et al.*, "Modulation of coherently coupled phased photonic crystal vertical cavity laser arrays," *IEEE Journal of Selected Topics in Quantum Electronics,* vol. 23, no. 6, pp. 1-9, 2017.

[17] Z. Gao, S. T. Fryslie, B. J. Thompson, P. S. Carney, and K. D. Choquette, "Parity-time symmetry in coherently coupled vertical cavity laser arrays," *Optica*, vol. 4, no. 3, pp. 323-329, 2017.

[18] B. J. Thompson, Z. Gao, S. T. Fryslie, M. T. Johnson, D. F. Siriani, and K. D. Choquette, "Coherence in multielement-phased vertical-cavity surface-emitting laser arrays using resonance tuning," *IEEE Photonics Journal,* vol. 9, no. 5, pp. 1-8, 2017.

[19] N. Yokouchi, A. J. Danner, and K. D. Choquette, "Two-dimensional photonic crystal confined vertical-cavity surface-emitting lasers," *IEEE Journal of Selected Topics in Quantum Electronics*, vol. 9, no. 5, pp. 1439-1445, 2003.

[20] P. O. Leisher, J. D. Sulkin, and K. D. Choquette, "Parametric study of proton-implanted photonic crystal vertical-cavity surface-emitting lasers," *IEEE Journal of Selected Topics in Quantum Electronics*, vol. 13, no. 5, pp. 1290-1294, 2007.

[21] D. F. Siriani, P. O. Leisher, and K. D. Choquette, "Loss-induced confinement in photonic crystal vertical-cavity surface-emitting lasers," *IEEE Journal of Quantum Electronics,* vol. 45, no. 7, pp. 762-768, 2009.

[22] M. P. Tan, A. M. Kasten, J. D. Sulkin, and K. D. Choquette, "Planar photonic crystal vertical-cavity surface-emitting lasers," *IEEE Journal of Selected Topics in Quantum Electronics,* vol. 19, no. 4, p. 4900107, 2013.

[23] B. J. Thompson, Z. Gao, H. Dave, S. T. Fryslie, K. Lakomy, and K. D. Choquette, "Classification of coherent supermodes in photonic crystal vertical cavity laser arrays," in *IEEE Photonics Conference (IPC),* 2017, pp. 529-530

[24] Z. Gao, B. J. Thompson, H. Dave, S. T. Fryslie, and K. D. Choquette, "Harnessing the asymmetry in coherently coupled 2×1 VCSEL arrays," in *IEEE Photonics Conference (IPC),* 2017, pp. 535-536

[25] Z. Gao *et al.*, "Non-Hermitian aspects of coherently coupled vertical cavity laser arrays," in *CLEO: Science and Innovations*, 2017, p. SW1C. 4: Optical Society of America.

[26] D. F. Siriani *et al.*, "Mode control in photonic crystal vertical-cavity surface-emitting lasers and coherent arrays," *IEEE Journal of Selected Topics in Quantum Electronics,* vol. 15, no. 3, pp. 909-917, 2009.

[27] N. Yokouchi, A. J. Danner, and K. D. Choquette, "Etching depth dependence of the effective refractive index in two-dimensional photonic-crystal-patterned vertical-cavity surface-emitting laser structures," *Applied Physics Letters,* vol. 82, no. 9, pp. 1344-1346, 2003.

[28] K. D. Choquette *et al.*, "Single mode photonic crystal vertical cavity surface emitting lasers," *Advances in Optical Technologies,* vol. 2012, 2012.

[29] K. D. Choquette and K. M. Geib, "Fabrication and performance of vertical-cavity surface-emitting lasers," in *Vertical-Cavity Surface-Emitting Lasers: Design, Characterization, and Applications*, C. Wilmsen, H. Temkin, and L. A. Coldren, Eds. Cambridge, U.K: Cambridge University Press, 1999, pp. 193-232.

[30] M. J. Adams, N. Li, B. R. Cemlyn, H. Susanto, and I. D. Henning, "Effects of detuning, gain-guiding, and index antiguiding on the dynamics of two laterally coupled semiconductor lasers," *Physical Review A*, vol. 95, no. 5, p. 053869, 2017.

[31] Z. Gao, M. T. Johnson, and K. D. Choquette, "Rate equation analysis and non-Hermiticity in coupled semiconductor laser arrays," *Journal of Applied Physics,* vol. 123, no. 17, p. 173102, 2018.

[32] A. C. Lehman, J. J. Raftery, P. S. Carney, and K. D. Choquette, "Coherence of photonic crystal vertical-cavity surface-emitting laser arrays," *IEEE Journal of Quantum Electronics,* vol. 43, no. 1, pp. 25-30, 2007.

[33] S. P. Hegarty *et al.*, "Transverse-mode structure and pattern formation in oxide-confined vertical-cavity semiconductor lasers," *Journal of the Optical Society of America B-Optical Physics,* vol. 16, no. 11, pp. 2060-2071, 1999.

CHAPTER 6: CONCLUSION AND FUTURE WORK

6.1 Conclusion

In this dissertation, we have presented a comprehensive study of 2×1 coherently coupled VCSEL arrays in the context of non-Hermitian photonics and mode engineering.

On the theoretical side, we have presented the analogy between coupled laser arrays and non-Hermiticity [including parity-time (PT) symmetry] in quantum mechanics. Two coupled lasers can be described using coupled mode theory with a 2×2 coupling matrix $\bar{\bar{\mathbf{M}}}$. With the presence of non-uniform gain/loss profile in the coupled laser array, the coupling matrix $\bar{\bar{\mathbf{M}}}$ is in general a complex and non-Hermitian matrix. Relative phase tuning, the origin of beam steering in the far-field intensity profile, is a result of the gain/loss profile in the system and the non-Hermiticity of $\bar{\bar{\mathbf{M}}}$. In Chapter 2, we have described two types of gain/loss profile, which should be treated differently within the formalism of coupled mode theory and the coupling matrix $\bar{\bar{\mathbf{M}}}$. The gain/loss contrast between two cavities (that are uniform within each cavity) induces non-Hermiticity through the diagonal elements in $\bar{\bar{\mathbf{M}}}$ by introducing imaginary components in the local resonant frequencies. On the other hand, gain/loss profiles that are non-uniform within each cavity (for example if the lasers are gain-guided) induce non-Hermiticty through the off-diagonal elements by introducing imaginary components in the coupling coefficients. Gain/loss localized in the coupling region also introduces imaginary components in the coupling coefficients by introducing gain splitting between the in-phase and out-of-phase modes. This in turn opens the possibility of dynamically modulating the array between the in- and out-of-phase modes.

When applying coupled mode theory to the experimentally observed tuning of the coherent mode, there is an inherent aspect of the problem that coupled mode theory itself does not address, namely the interaction between the photons and the carriers injected. Lasers are not simply waveguides with either gain or loss, but rather are inherently nonlinear devices because of the interaction between photons and the gain medium, evident in the existence of lasing threshold. However, coupled mode theory is inherently a linear theory, so it cannot capture the nonlinear behavior of lasers. Stated in another way, the coupled mode theory requires the frequency detuning and gain/loss contrast between cavities as input parameters to calculate the coupled mode, but neither can be directly controlled or measured in coupled diode lasers. To address this problem, we employ coupled rate equation analysis, which includes carrier density dynamics (treated by rate equations) in addition to the coupled mode theory.

In Chapter 3, we presented the coupled rate equation analysis for 2×1 coupled laser arrays. The coupled rate equation analysis takes carrier injection rates ($Q_{A,B}$) and the cavity frequency detuning $\Delta\Omega$ as input parameters, which are both experimentally controllable. In coupled VCSEL arrays, both $Q_{A,B}$ and $\Delta\Omega$ are linearly dependent on the injection currents. Note that we have defined $\Delta\Omega$ to be different from the total frequency detuning $\Delta\omega$ between the two cavities. The total frequency detuning $\Delta\omega$ is the input parameter required by coupled mode theory, while $\Delta\Omega$ is only part of $\Delta\omega$ (the amplitude-phase coupling contribution is excluded). Clearly distinguishing $\Delta\Omega$ and $\Delta\omega$ is crucial to maintain the consistency between conclusions drawn from coupled mode theory and from coupled rate equation analysis.

Using coupled rate equation analysis, we show that depending on the strength of optical coupling compared to the cavity loss rate, the coupled laser array exhibits different response to the tuning of $Q_{A,B}$ and $\Delta\Omega$. Coherently coupled VCSEL arrays as designed and fabricated for this dissertation belong to the weak coupling regime (i.e., $|\kappa| < 1/\tau_p$). In the weak coupling regime, assuming real-valued κ, the cavity detuning $\Delta\Omega$ induces a gain contrast, and the relative phase between two lasers is controlled by the cavity detuning $\Delta\Omega$ through the lever of induced gain contrast. This detuning-induced gain contrast is a unique mode tuning mechanism in weakly coupled semiconductor laser arrays. We have also identified the required $Q_{A,B}$ and $\Delta\Omega$ to achieve PT symmetry and exceptional points in weakly coupled laser arrays.

In addition to the study of mode tuning, we also apply coupled rate equations to the study of small-signal dynamics of the coupled modes, including the stability of the modes and the small-signal modulation response under external current modulation. We have shown that at the exceptional points, the dynamics of the non-Hermitian arrays are undetermined, and warrant future investigation.

The experimental study of 2 × 1 optically coupled electrically isolated VCSEL arrays is summarized in Chapter 5. Because we have independent control over the two injection currents I_A and I_B into cavities A and B, characterization of the arrays is particularly conducive to 2D plots with both I_A and I_B varied. Concise 2D characterizations of light-versus-current, far-field interference visibility, and beam-steering angle have been presented to illustrate the mode tuning behavior. The coherence region (where the two lasers are mutually coherent and interfere in the far field) is very evident in the 2D far-field interference visibility map. It is observed that the width of the high coherence region decreases with higher bias and the beam steering becomes more sensitive to the current tuning at higher bias, both suggesting that the coupling coefficient decreases with higher bias. From near-field and far-field characterizations, we extract the coupled mode and the relative phase between cavities. Near the lasing threshold, the coupled mode resembles $\overline{\boldsymbol{E}} = \begin{bmatrix} 1 \\ \sqrt{R}e^{i\phi} \end{bmatrix}$, with both the intensity ratio between cavities (R) and the relative phase (ϕ) being tuned by the currents. At higher bias levels, the coupled mode resembles $\overline{\boldsymbol{E}} =$

$\begin{bmatrix} 1 \\ e^{i\phi} \end{bmatrix}$, with ϕ being tuned and R fixed at 1. Moreover, we identify modes with broken PT symmetry ($\overline{\boldsymbol{E}} = \begin{bmatrix} 1 \\ \pm ie^{\mp\theta} \end{bmatrix}$) and modes at the exceptional point ($\overline{\boldsymbol{E}} = \begin{bmatrix} 1 \\ \pm i \end{bmatrix}$).

We experimentally extract the coupling coefficient of coherent VCSEL arrays from the slope of beam steering angle versus the cavity frequency detuning and estimate that $(\kappa_i + \alpha_H \kappa_r) \cong -38 \times 10^9\ \mathrm{rad/s}$. We also outlined the approach to further determine the values of κ_i and κ_r separately. The existence of nonzero κ_i can be quantitatively examined from the power increase due to coupling in the 2D LI characteristics.

Finally, we showed that by introducing asymmetry in the design of coupled VCSEL arrays, the mode tuning behavior can be engineered. The location of the coherence locking region can be shifted away from the diagonal in a controlled manner, and the beam steering behavior becomes asymmetrical too.

The work presented in this dissertation represents a step forward in the understanding and engineering of coherently coupled VCSEL arrays. Modeling coupled VCSEL arrays as nonlinear non-Hermitian photonic dimers reveals the unique mode tuning mechanism and can serve as a new foundation for device modeling, which can lead to improved array designs and novel operating schemes. Experimentally, comprehensive characterizations of the 2×1 coupled VCSEL arrays have been carried out, revealing the mode tuning details and answering long posed questions. Future research guided by this dissertation may lead to novel mode control and improved dynamical modulation in coupled laser arrays.

6.2 Future work

Throughout this dissertation future work has been proposed. Here we summarize. First of all, the coupling coefficient is a parameter of great interest, in both the modeling of mode tuning and the modeling of small-signal dynamics. Using the method outlined in Section 5.4, it should be possible to determine both the real and imaginary components of the coupling coefficient. The accurate value of coupling coefficient would benefit future modeling and lead to better designs of the arrays.

In addition, the coupling coefficient (both the real and the imaginary components) is expected to be dynamically controllable if we can locally control current injection into the coupling region. This could be straightforwardly studied using 3×1 arrays with the middle element serving as the coupling region [1]. Varying the pumping in the middle element (below its threshold) should tune the coupling coefficient between the two outer lasers. The variation of the coupling coefficient would be evident from the 2D L-I and visibility maps (using I_1 and I_3 as the two axes while I_2 is fixed at various values). By observing how the value of I_2 changes the 2D maps, or performing coupling coefficient extraction at each I_2 value, we can quantitatively describe the control of coupling coefficient.

Lastly, the calculation for small-signal dynamics setup in Chapter 4 is a powerful tool for modeling the high-speed modulation of coherent VCSEL arrays. It describes two VCSELs that are mutually injection locked with no assumptions of master or slave. It is a numerical method with the flexibility of employing simultaneous frequency detuning, gain/loss contrast, and complex-valued coupling coefficient. It would be interesting to see the modulation response of the non-Hermitian arrays and how non-Hermiticity affects the modulation response, for example the modulation response near the exceptional points. The small signal calculation also offers the ability to model different modulation schemes, say modulating the two VCSELs simultaneously with in-phase ($Q_{Am} = Q_{Bm}$) or out-of-phase ($Q_{Am} = -Q_{Bm}$, push-pull modulation [2]) sinusoidal currents.

6.3 References

[1] B. J. Thompson, Z. Gao, H. Dave, S. T. Fryslie, K. Lakomy, and K. D. Choquette, "Classification of coherent supermodes in photonic crystal vertical cavity laser arrays," in *IEEE Photonics Conference (IPC)*, 2017, pp. 529-530

[2] C. Chen, K. L. Johnson, M. Hibbs-Brenner, and K. D. Choquette, "Push-pull modulation of a composite-resonator vertical-cavity laser," *IEEE Journal of Quantum Electronics,* vol. 46, no. 4, pp. 438-446, 2010.

APPENDIX A: DERIVATION OF THE COUPLED MODE THEORY AND THE COUPLED RATE EQUATIONS

A.1 Coupled mode theory

Although laterally coupled VCSEL arrays are complex 3D structures, we can approximate their behavior with a simpler 2D model in the spirit of effective index method. The 2D model is sketched below. The two coupled VCSELs are modeled as two index-guided stripe waveguides coupled in x direction and propagating in z direction, with high reflectivity mirrors terminating the waveguides at $z = 0$ and $z = -L$. In other words, the longitudinal modes are in z direction and transverse modes are in x direction.

For TE-polarized field [excited by TE polarization $\boldsymbol{P}(x,z) = P(x,z)\hat{\boldsymbol{y}}$], the field components are

$$\boldsymbol{E}(x,z,t) = E(x,z,t)\,\hat{\boldsymbol{y}}$$

$$\boldsymbol{H}(x,z,t) = H_x(x,z,t)\hat{\boldsymbol{x}} + H_z(x,z,t)\hat{\boldsymbol{z}}$$

From Maxwell's equations we can derive the scalar wave equation for TE-polarized electric field as

$$\nabla^2 E(x,z,t) = \frac{\epsilon_C(x,z)}{c^2}\ddot{E}(x,z,t) + \mu_0\sigma\dot{E}(x,z,t) + \mu_0\dot{P}(x,z,t) \qquad (\mathrm{A}.1)$$

where $\nabla^2 = \frac{\partial^2}{\partial x^2} + \frac{\partial^2}{\partial z^2}$, $\ddot{E} = \frac{\partial^2 E}{\partial t^2}$, $\dot{E} = \frac{\partial E}{\partial t}$, $\dot{P} = \frac{\partial P}{\partial t}$, ϵ_C is the relative permittivity of the composite system consisting of two lasers, c is the speed of light in vacuum, μ_0 is the vacuum permeability, and σ is the conductivity (here assumed to be independent of x and z) representing the spatially invariant loss in the cavity (for example mirror loss at the ends of cavities). The interaction between the electric field and the active media is represented through the polarization P.

Now we want to expand the electric field with spatial basis functions $u_m^A(x,z)$ and $u_{m'}^B(x,z)$ that represent individual cavity modes in laser A and B respectively. A set of resonant modes, $u_m^A(x,z)e^{-i\omega_m t}$, exist for VCSEL cavity A when cavity B is absent [with permittivity profile shown in Figure A.1(b)], and $u_{m'}^B(x,z)e^{-i\omega_{m'} t}$ is supported when there is cavity B only [Figure A.1(c)]. For VCSELs, only one longitudinal mode overlaps with the gain spectrum. For the transverse modes, in the simplest (and often experimentally achievable) case, the laser emits in only one transverse mode. In this simplest situation, the basis functions consist of only two modes: $u_A(x,z) \equiv u_{TE0}^A(x)\sin(k_z^A z)$ and $u_B(x,z) \equiv u_{TE0}^B(x)\sin(k_z^B z)$, where $u_{TE0}^A(x)$ and $u_{TE0}^B(x)$ are the fundamental transverse TE mode profiles, $\sin(k_z^A z)$ and $\sin(k_z^B z)$ are the longitudinal mode profiles. We can expand the total field in the composite structure as

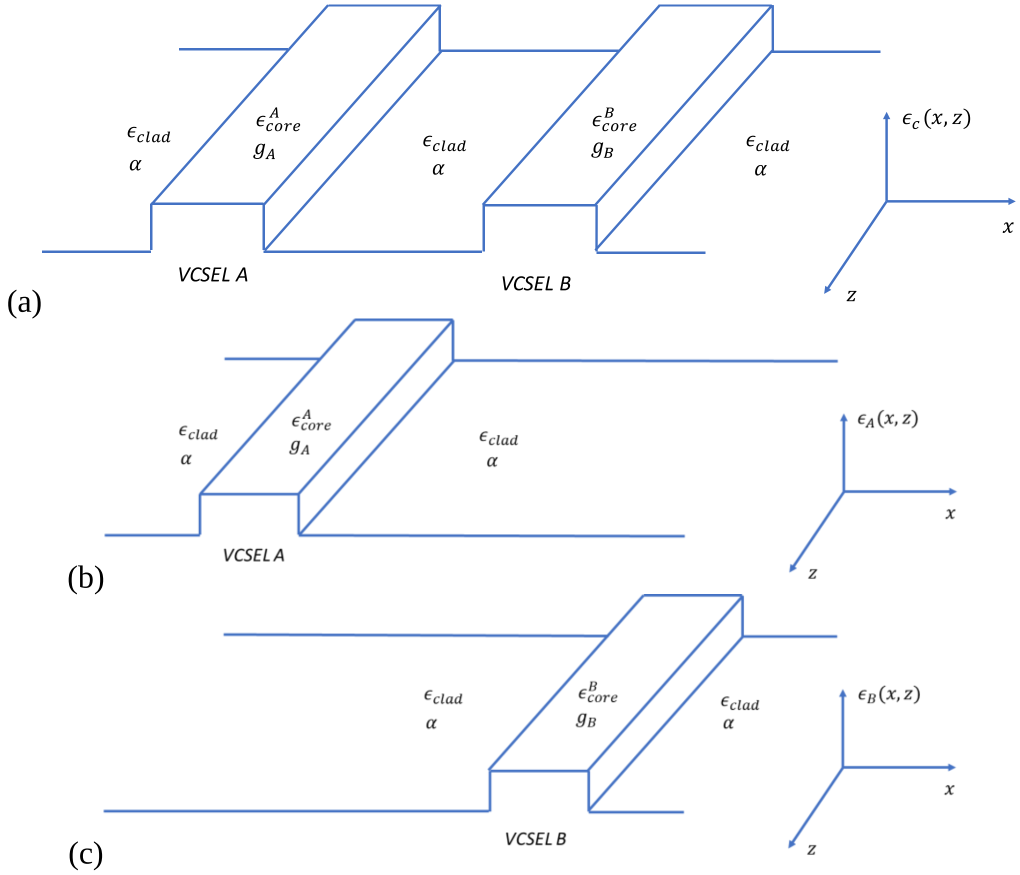

Figure A.1: (a) Permittivity profile for the coupled VCSEL array in a two-dimensional model; (b) Permittivity profile when cavity B is absent; (c) permittivity profile when cavity A is absent.

$$E(x,z,t) = u_A(x,z)|E_A(t)|e^{-i\phi_A(t)-i\omega t} + u_B(x,z)|E_B(t)|e^{-i\phi_B(t)-i\omega t}$$

or simply

$$E(x,z,t) = u_A(x,z)E_A(t)e^{-i\omega t} + u_B(x,z)E_B(t)e^{-i\omega t} \tag{A.2}$$

where $E_{A,B}(t) \equiv \left|E_{A,B}(t)\right|e^{-i\phi_{A,B}(t)}$ are the complex field amplitudes that are slowly varying compared to $e^{-i\omega t}$. Similarly, we can write the polarization as

$$p(x,z,t) = u_A(x,z)p_A(t)e^{-i\phi_A(t)-i\omega t} + u_B(x,z)p_B(t)e^{-i\phi_B(t)-i\omega t} \tag{A.3}$$

where $p_{A,B}(t)$ are also complex-valued and slowly varying. The real part of $p_{A.B}(t)$ represents the polarization that is in-phase with the electric field, while the imaginary part of $p_{A.B}(t)$ represents the polarization that is $\pi/2$ out of phase with the electric field. Later we will see that $Re(p_{A,B})$ represents the carrier suppression of index and $Im(p_{A,B})$ represents the gain/loss from stimulated emission/absorption [1].

Note that by writing the polarization in the form of Equation (A.3), we have assumed that the polarization shares the same spatial profile as the electric field in each cavity. In other words, *the gain/loss and index change represented by $p(x,z,t)$ are assumed to be uniformly distributed within each individual cavity mode $u_{A,B}(x,z)$ here*. Although strictly speaking the gain (in the active region) and loss (in the cladding or other unpumped region) profile are not uniform in the individual laser, as a first-order perturbation theory, we treat the gain/loss as a perturbation on top of the real-valued index-guiding profile. We assume that the gain/loss profile is weak compared to the unperturbed real-valued index profile so that it does not vary the optical mode profile [$u_{A,B}(x,z)$] but rather only adds an imaginary part to the resonant frequency of the mode [2]. This assumption is consistent with the index-guiding nature of the laser (instead of being gain-guided). By making this assumption, we have effectively ignored the spatial profile of gain/loss and treat it as uniformly distributed across the mode profile $u_{A,B}(x,z)$, which is why we can expand the polarization in the form of Equation (A.3). *Any gain/loss profile that is not uniform within the individual cavities should be included in $\epsilon_{C,A,B}(x,z)$ as an imaginary component* - for example if the lasers are gain-guided, or if there is gain/loss located between the two cavities, as discussed in Section 2.4.

Now we want to rewrite the wave equation, Equation (A.1), with the electric field and polarization represented by the expansions in Equation (A.2) and (A.3). With slowly varying approximation, which says $|\dot{E}_{A,B}| \ll \omega|E_{A,B}|$, $|\dot{p}_{A,B}| \ll \omega|p_{A,B}|$, $|\dot{\phi}_{A,B}| \ll \omega$ (hence $|\ddot{E}_{A,B}| \ll \omega|\dot{E}_{A,B}|$, $|\ddot{p}_{A,B}| \ll \omega|\dot{p}_{A,B}|$, etc.), we have

$$\nabla^2 E(x,z,t) = (\nabla^2 u_A)E_A(t)e^{-i\omega t} + (\nabla^2 u_B)E_B(t)e^{-i\omega t} \tag{A.4}$$

$$\begin{aligned}\ddot{E}(x,z,t) &= u_A e^{-i\omega t}\left(\ddot{E}_A - 2i\omega\dot{E}_A - \omega^2 E_A\right) + u_B e^{-i\omega t}\left(\ddot{E}_B - 2i\omega\dot{E}_B - \omega^2 E_B\right)\\ &\cong e^{-i\omega t}\left(-2i\omega u_A\dot{E}_A - \omega^2 u_A E_A - 2i\omega u_B\dot{E}_B - \omega^2 u_B E_B\right)\end{aligned} \tag{A.5}$$

$$\begin{aligned}\sigma\dot{E}(x,z,t) &= u_A e^{-i\omega t}\left(\sigma\dot{E}_A - i\omega\sigma E_A\right) + u_B e^{-i\omega t}\left(\sigma\dot{E}_B - i\omega\sigma E_B\right)\\ &\cong e^{-i\omega t}\sigma(-i\omega u_A E_A - i\omega u_B E_B)\end{aligned} \tag{A.6}$$

$$\begin{aligned}\ddot{p}(x,z,t) = e^{-i\omega t}\big(&u_A\ddot{p}_A e^{-i\phi_A} - 2iu_A\dot{p}_A\dot{\phi}_A e^{-i\phi_A} - iu_A p_A\ddot{\phi}_A e^{-i\phi_A} - u_A p_A\dot{\phi}_A\dot{\phi}_A e^{-i\phi_A}\\ &+ u_B\ddot{p}_B e^{-i\phi_B} - 2iu_B\dot{p}_B\dot{\phi}_B e^{-i\phi_B} - iu_B p_B\ddot{\phi}_B e^{-i\phi_B} - u_B p_B\dot{\phi}_B\dot{\phi}_B e^{-i\phi_B}\\ &- 2i\omega u_A\dot{p}_A e^{-i\phi_A} - 2\omega u_A p_A\dot{\phi}_A e^{-i\phi_A} - 2i\omega u_B\dot{p}_B e^{-i\phi_B} - 2\omega u_B p_B\dot{\phi}_B e^{-i\phi_B}\\ &- \omega^2 u_A p_A e^{-i\phi_A} - \omega^2 u_B p_B e^{-i\phi_B}\big)\\ \cong e^{-i\omega t}\big(&-\omega^2 u_A p_A e^{-i\phi_A} - \omega^2 u_B p_B e^{-i\phi_B}\big)\end{aligned} \tag{A.7}$$

In the expression of $\ddot{E}(x,z,t)$, we keep terms to the order of $\omega\dot{E}_A$, while in the expression of $\sigma\dot{E}(x,z,t)$ and $\ddot{p}(x,z,t)$, we drop the terms with first order time derivatives of E, p and ϕ and only keep terms to the order of $E_{A,B}$ and $p_{A,B}$, because $\mu_0\sigma\dot{E}(x,z,t)$ and $\mu_0\dot{p}(x,z,t)$ represent loss and gain, and they are small quantities compared to $\nabla^2 E(x,z,t)$ and $\frac{\epsilon_C(x,z)}{c^2}\ddot{E}(x,z,t)$ [3].

Taking Equations (A.4)-(A.7) into Equation (A.1), we have

$$\begin{aligned}\left(\nabla^2 u_A + \frac{\epsilon_C}{c^2}\omega^2 u_A\right)E_A + \left(\nabla^2 u_B + \frac{\epsilon_C}{c^2}\omega^2 u_B\right)E_B + 2i\omega\frac{\epsilon_C}{c^2}\left(u_A\dot{E}_A + u_B\dot{E}_B\right)\\ +i\omega\mu_0\sigma(u_AE_A + u_BE_B) + \omega^2\mu_0(u_Ap_A + u_Bp_B) = 0\end{aligned} \tag{A.8}$$

From the definition of u_A and u_B being the resonant mode for the individual waveguides, we know that they satisfy Maxwell's equations given the individual laser permittivity profile $\epsilon_A(x,z)$ and $\epsilon_B(x,z)$ shown in Figures A.1(b) and (c):

$$\nabla^2 u_{A,B}(x,z) + \frac{\epsilon_{A,B}(x,z)}{c^2}\Omega_{A,B}^2 u_{A,B}(x,z) = 0 \tag{A.9}$$

where $\Omega_{A,B}$ are the resonant frequencies of cavity A and B respectively. Later, after we introduce the carrier densities, we will clarify that $\Omega_{A,B}$ should be defined as the resonant frequencies for a specific carrier density, and we will define $\Omega_{A,B}$ as the resonant frequencies at threshold carrier densities.

Taking $\nabla^2 u_{A,B}(x,z) = -\frac{\epsilon_{A,B}}{c^2}\Omega_{A,B}^2 u_{A,B}(x,z)$ into Equation (A.8), we have

$$\begin{aligned}(\epsilon_C\omega^2 - \epsilon_A\Omega_A^2)u_AE_A + (\epsilon_C\omega^2 - \epsilon_B\Omega_B^2)u_BE_B + 2i\omega\epsilon_C\left(\dot{E}_Au_A + \dot{E}_Bu_B\right)\\ +i\omega c^2\mu_0\sigma(E_Au_A + E_Bu_B)\ + \omega^2c^2\mu_0(u_Ap_A + u_Bp_B) = 0\end{aligned} \tag{A.10}$$

Multipling Equation (A.10) by $u_A^*(x,z)$ and integrating over x from $-\infty$ to ∞, we get

$$\begin{aligned}E_A\int_{-\infty}^{\infty}u_A^*(\epsilon_C\omega^2 - \epsilon_A\Omega_A^2)u_Adx + E_B\int_{-\infty}^{\infty}u_A^*(\epsilon_C\omega^2 - \epsilon_B\Omega_B^2)u_Bdx + 2i\omega\dot{E}_A\int_{-\infty}^{\infty}u_A^*\epsilon_Cu_Adx\\ +2i\omega\dot{E}_B\int_{-\infty}^{\infty}u_A^*\epsilon_Cu_Bdx + i\omega c^2\mu_0\sigma\left(E_A\int_{-\infty}^{\infty}u_A^*u_Adx + E_B\int_{-\infty}^{\infty}u_A^*u_Bdx\right)\\ +\omega^2c^2\mu_0\left(p_A\int_{-\infty}^{\infty}u_A^*u_Adx + p_B\int_{-\infty}^{\infty}u_A^*u_Bdx\right) = 0\end{aligned} \tag{A.11}$$

We treat $\int_{-\infty}^{\infty}u_A^*u_Bdx \equiv \langle u_A|u_B\rangle$ as a small perturbation and drop the terms that are higher-order to $\langle u_A|u_B\rangle$. For example, $2i\omega\dot{E}_B\int_{-\infty}^{\infty}u_A^*\epsilon_ru_Bdx$, $i\omega c^2\mu_0\sigma E_B\int_{-\infty}^{\infty}u_A^*u_Bdx$ and $\omega^2c^2\mu_0p_B\int_{-\infty}^{\infty}u_A^*u_Bdx$ are dropped because they are second order terms (contain multiplication of two small quantities). More specifically, $2i\omega\dot{E}_B\int_{-\infty}^{\infty}u_A^*\epsilon_r u_B dx$ is second order because $\omega\dot{E}_B \ll \omega^2 E_B$, and also $\int_{-\infty}^{\infty}u_A^*\epsilon_C u_B dx$ is small:

$$2i\omega\dot{E}_B\int_{-\infty}^{\infty}u_A^*\epsilon_C u_B dx \ll E_B\omega^2\int_{-\infty}^{\infty}u_A^*(\epsilon_C-\epsilon_B)u_B dx \sim E_B\int_{-\infty}^{\infty}u_A^*(\epsilon_C\omega^2-\epsilon_B\Omega_B^2)u_B dx$$

Equation (A.11) then turns into

$$E_A\int_{-\infty}^{\infty}u_A^*(\epsilon_C\omega^2-\epsilon_A\Omega_A^2)u_A dx + E_B\int_{-\infty}^{\infty}u_A^*(\epsilon_C\omega^2-\epsilon_B\Omega_B^2)u_B dx + 2i\omega\dot{E}_A\langle u_A|\epsilon_C|u_A\rangle + i\omega c^2\mu_0\sigma E_A\langle u_A|u_A\rangle + \omega^2c^2\mu_0 p_A\langle u_A|u_A\rangle = 0 \qquad (\mathrm{A.12})$$

where we used notations $\langle u_A|u_A\rangle \equiv \int_{-\infty}^{\infty}u_A^*\epsilon_r u_A dx$ and $\langle u_A|\epsilon_C|u_A\rangle \equiv \int_{-\infty}^{\infty}u_A^*\epsilon_C u_A dx$.

Furthermore, we also know that $\left|\omega-\Omega_{A,B}\right| \ll \omega, \Omega_{A,B}$ when the coupling happens. Hence, we can use $\epsilon_C\omega^2-\epsilon_B\Omega_B^2 \cong \omega^2(\epsilon_C-\epsilon_B)$ in the cross-coupling term:

$$E_B\int_{-\infty}^{\infty}u_A^*(\epsilon_C\omega^2-\epsilon_B\Omega_B^2)u_B dx \cong E_B\omega^2\int_{-\infty}^{\infty}u_A^*(\epsilon_C-\epsilon_B)u_B dx \equiv E_B\omega^2\langle u_A|\epsilon_C-\epsilon_B|u_B\rangle$$

In the self-coupling term, we need to use a more accurate approximation $\Omega_A \cong \omega^2-2\omega(\omega-\omega_A)$ because the self-coupling term is a 0-th order term. Then we have

$$\begin{aligned} E_A\int_{-\infty}^{\infty}u_A^*(\epsilon_C\omega^2-\epsilon_A\Omega_A^2)u_A dx &= E_A\int_{-\infty}^{\infty}u_A^*u_A\{\epsilon_C\omega^2-\epsilon_A[\omega^2-2\omega(\omega-\Omega_A)+(\omega-\Omega_A)^2]\}dx \\ &\cong E_A\int_{-\infty}^{\infty}u_A^*u_A[(\epsilon_C-\epsilon_A)\omega^2+2\omega\epsilon_A(\omega-\Omega_A)]dx \\ &= E_A\omega^2\int_{-\infty}^{\infty}u_A^*u_A(\epsilon_C-\epsilon_A)dx + E_A 2\omega(\omega-\Omega_A)\int_{-\infty}^{\infty}u_A^*u_A\epsilon_A dx \\ &\cong E_A 2\omega(\omega-\Omega_A)\int_{-\infty}^{\infty}u_A^*u_A\epsilon_A dx \qquad (\mathrm{A.13}) \end{aligned}$$

where we have dropped the second order term $E_A\omega^2\int_{-\infty}^{\infty}u_A^*u_A(\epsilon_C-\epsilon_A)dx$. $\epsilon_C-\epsilon_A$ is nonzero only within cavity B, and $u_A(\epsilon_C-\epsilon_A) \ll u_B$ within cavity B. Hence $\int_{-\infty}^{\infty}u_A^*u_A(\epsilon_C-\epsilon_A)dx \ll \int_{-\infty}^{\infty}u_A^*u_B dx$.

Now Equation (A.12) turns into

$$E_A 2\omega(\omega-\Omega_A)\langle u_A|\epsilon_A|u_A\rangle + E_B\omega^2\langle u_A|\epsilon_C-\epsilon_B|u_B\rangle + 2i\omega\dot{E}_A\langle u_A|\epsilon_C|u_A\rangle + i\omega c^2\mu_0\sigma E_A\langle u_A|u_A\rangle + \omega^2c^2\mu_0 p_A\langle u_A|u_A\rangle = 0 \tag{A.14}$$

Using the approximation $\langle u_A|\epsilon_r|u_A\rangle \cong \langle u_A|\epsilon_A|u_A\rangle$, as we have previously argued that $\langle u_A|\epsilon_r-\epsilon_A|u_A\rangle$ is a second order term, we have

$$\dot{E}_A = i(\omega-\Omega_A)E_A + i\frac{\omega}{2}\frac{\langle u_A|\epsilon_C-\epsilon_B|u_B\rangle}{\langle u_A|\epsilon_A|u_A\rangle}E_B - \frac{\sigma}{2\epsilon_0}\frac{\langle u_A|u_A\rangle}{\langle u_A|\epsilon_A|u_A\rangle}E_A + i\frac{\omega}{2\epsilon_0}\frac{\langle u_A|u_A\rangle}{\langle u_A|\epsilon_A|u_A\rangle}p_A \tag{A.15}$$

Although it is phenomenological and a bit arbitrary, we use $-\frac{\sigma}{2\epsilon_0}\frac{\langle u_A|u_A\rangle}{\langle u_A|\epsilon_A|u_A\rangle}E_A$ to represent cavity loss (mirror loss), and use $i\frac{\omega}{2\epsilon_0}\frac{\langle u_A|u_A\rangle}{\langle u_A|\epsilon_A|u_A\rangle}p_A$ to represent the gain/loss related to the stimulated emission/absorption and the carrier induced index change. We can write the cavity loss as

$$-\frac{\sigma}{2\epsilon_0}\frac{\langle u_A|u_A\rangle}{\langle u_A|\epsilon_A|u_A\rangle} = -\frac{\gamma_E}{2} \tag{A.16}$$

where γ_E is the mirror loss rate. We can write the polarization term as

$$i\frac{\omega}{2\epsilon_0}\frac{\langle u_A|u_A\rangle}{\langle u_A|\epsilon_A|u_A\rangle}p_A = i\frac{\omega}{2}\chi E_A = i\frac{\omega}{2}\chi' E_A - \frac{\omega}{2}\chi'' E_A \tag{A.17}$$

by defining $p_A \equiv \epsilon_{eff}\epsilon_0\chi E_A$ where $\epsilon_{eff} \equiv \frac{\langle u_A|\epsilon_A|u_A\rangle}{\langle u_A|u_A\rangle}$ is the effective permittivity, $\chi = \chi' + i\chi''$ is the effective susceptibility. χ' represents carrier induced index change (amplitude phase coupling) and χ'' represents inter-band emission/absorption (gain/loss). Although $\chi = \chi' + i\chi''$ can be calculated *ab inito* [1], it is also convenient to write Equation (A.16) and (A.17) using experimentally measured parameters [4]:

$$-\frac{\sigma}{2\epsilon_0}\frac{\langle u_A|u_A\rangle}{\langle u_A|\epsilon_A|u_A\rangle} + i\frac{\omega}{2\epsilon_0}\frac{\langle u_A|u_A\rangle}{\langle u_A|\epsilon_A|u_A\rangle}p_A = \frac{\Gamma v_g a_{\mathrm{diff}}}{2}(N_A-N_{th})(1-i\alpha_H)E_A \tag{A.18}$$

where Γ is the confinement factor, v_g the group velocity, a_{diff} the differential gain of active material, N_A the carrier density in laser A, N_{th} the threshold carrier density (assumed to be the same for both laser A and B), and α_H the linewidth enhancement factor. Equation (A.18) equals zero when $N_A = N_{th}$, meaning that the carrier-induced index change (hence carrier-induced frequency shift) is also zero, which is consistent with our definition that Ω_A is the resonant frequency at threshold carrier density level.

Taking Equation (A.18) into (A.15), we arrive at

$$\dot{E}_A = i(\omega - \Omega_A)E_A + i\kappa_{AB}E_B + \frac{\Gamma v_g a_{diff}}{2}(N_A - N_{th})(1 - i\alpha_H)E_A \qquad (\mathrm{A}.19)$$

where $\kappa_{AB} \equiv \frac{\omega}{2}\frac{\langle u_A|\epsilon_C - \epsilon_B|u_B\rangle}{\langle u_A|\epsilon_A|u_A\rangle}$.

Similarly, we have

$$\dot{E}_B = i(\omega - \Omega_B)E_B + i\kappa_{BA}E_A + \frac{\Gamma v_g a_{diff}}{2}(N_B - N_{th})(1 - i\alpha_H)E_B \qquad (\mathrm{A}.20)$$

where

$$\kappa_{BA} \equiv \frac{\omega}{2}\frac{\langle u_B|\epsilon_C - \epsilon_A|u_A\rangle}{\langle u_B|\epsilon_B|u_B\rangle} \qquad (A20b).$$

Equations (A.19) and (A.20) are the temporal coupled mode equations for two side-by-side coupled lasers. In terms of real-valued variables ($E_{A,B} = |E_{A,B}|e^{i\phi_{A,B}}, \kappa_{AB} = \kappa_{BA} = \kappa_r + i\kappa_i$), we have

$$\frac{d|E_A|}{dt} = \frac{1}{2}\Gamma v_g a_{diff}(N_A - N_{th})|E_A| - [\kappa_i\, cos(\phi_B - \phi_A) + \kappa_r\, sin(\phi_B - \phi_A)]|E_B| \qquad (\mathrm{A}.21)$$

$$\frac{d|E_B|}{dt} = \frac{1}{2}\Gamma v_g a_{diff}(N_B - N_{th})|E_B| - [\kappa_i \cos(\phi_B - \phi_A) - \kappa_r \sin(\phi_B - \phi_A)]|E_A| \qquad (\mathrm{A}.22)$$

$$\frac{d(\phi_B - \phi_A)}{dt} = -(\Omega_B - \Omega_\mathrm{A}) + \frac{1}{2}\alpha_H \Gamma v_g a_{diff}(N_A - N_B)$$
$$+\kappa_r \cos(\phi_B - \phi_A)\left(\left|\frac{E_A}{E_B}\right| - \left|\frac{E_B}{E_A}\right|\right) + \kappa_i \sin(\phi_B - \phi_A)\left(\left|\frac{E_A}{E_B}\right| + \left|\frac{E_B}{E_A}\right|\right) \qquad (\mathrm{A}.23)$$

[Equations (A.21)-(A.23) are obtained by taking $E_{A,B} = |E_{A,B}|e^{i\phi_{A,B}}, \kappa_{AB} = \kappa_{BA} = \kappa_r + i\kappa_i$ into Equations (A.19) and (A.20). Then separately write equations for the terms that are in-phase with $e^{i\phi_A}$ and the terms that are in-phase with $ie^{i\phi_A}$.]

The coupling coefficients have been taken to be symmetrical ($\kappa_{AB} = \kappa_{BA}$) on the ground that we are assuming that the two lasers are identical except for the different injection rates and the frequency detuning. As a first-order perturbation theory we see that the frequency detuning does not change the coupling coefficient. κ is taken to be complex in general, with κ_r representing the frequency splitting between the in-phase and out-of-phase coupled modes, while κ_i represents the gain splitting between them [5].

A.2 Coupled rate equations

Coupled rate equations consist of the coupled mode Equations (A.21) - (A.23) and the carrier density rate equation

$$\frac{dN_{A,B}}{dt} = P_{A,B} - \frac{N_{A,B}}{\tau_N} - v_g\left[g_{th} + a_{diff}\left(N_{A,B} - N_{th}\right)\right]\left|E_{A,B}\right|^2 \tag{A.24}$$

where $P_{A,B}$ are the carrier injection rates with unit of $\mathrm{cm}^{-3}\mathrm{s}^{-1}$, τ_N is the carrier lifetime, g_{th} is the threshold gain. Also note that we choose the normalization of $E_{A,B}(t)$ to be that $\left|E_{A,B}(t)\right|^2$ are the photon densities with unit of cm^{-3}.

We have followed [4] and defined the dimensionless carrier densities $M_{A,B}$, dimensionless pump rates $Q_{A,B}$, and dimensionless field magnitudes $Y_{A,B}$ as:

$$M_{A,B} \equiv 1 + v_g \Gamma a_{diff} \tau_p \left(N_{A,B} - N_{th}\right) \tag{A.25}$$

$$Q_{A,B} \equiv 1 + v_g \Gamma a_{diff} \tau_p \left(P_{A,B}\tau_N - N_{th}\right) \tag{A.26}$$

$$Y_{A,B} \equiv \sqrt{v_g a_{diff} \tau_N}\left|E_{A,B}\right| \tag{A.27}$$

From Equation (A.26) we have $Q_{A,B} = C_Q \left(\frac{P_{A,B}}{P_{th}} - 1\right) + \frac{P_{A,B}}{P_{th}} = C_Q \left(\frac{I_{A,B}}{I_{th}} - 1\right) + \frac{I_{A,B}}{I_{th}}$, where C_Q is the constant relating injected currents to normalized pump parameters, defined as $C_Q \equiv \frac{a_{\mathrm{diff}} N_{tr}}{g_{th}}$. N_{tr} is the transparency carrier density, $I_{A.B}$ are injected currents and I_{th} is the threshold current. The threshold gain g_{th} is related to photon lifetime by $v_g \Gamma g_{th} = v_g \Gamma a_{diff}(N_{th} - N_{tr}) = \frac{1}{\tau_p} = \gamma_E + v_g \alpha_0$, where α_0 is the absorption coefficient from the unpumped cladding. The normalized parameters at transparency and threshold conditions are simply: $M_{A,Btr} = 0$, $M_{A,Bth} = 1$, $Q_{A,Btr} = 0$, $Q_{A,Bth} = 1$, where the subscript tr denotes transparency and th denotes threshold. In terms of the dimensionless variables, coupled rate equations are written as

$$\frac{dY_A}{dt} = \frac{1}{2\tau_p}(M_A - 1)Y_A - (\kappa_r sin\phi + \kappa_i \cos\phi)Y_B \qquad (A.28)$$

$$\frac{dY_B}{dt} = \frac{1}{2\tau_p}(M_B - 1)Y_B + (\kappa_r sin\phi - \kappa_i \cos\phi)Y_A \qquad (A.29)$$

$$\frac{d\phi}{dt} = \frac{\alpha_H}{2\tau_p}(M_A - M_B) - \Delta\Omega + \kappa_r cos\phi \left(\frac{Y_A}{Y_B} - \frac{Y_B}{Y_A}\right) + \kappa_i sin\phi \left(\frac{Y_A}{Y_B} + \frac{Y_B}{Y_A}\right) \qquad (A.30)$$

$$\frac{dM_{A,B}}{dt} = \frac{1}{\tau_N}\left[Q_{A,B} - M_{A,B}\left(1 + Y_{A,B}^2\right)\right] \qquad (A.31)$$

where $\phi = \phi_B - \phi_A$, $\Delta = \Omega_B - \Omega_A$.

Equations (A.28)-(A.31) are the coupled rate equations. In the future, if we want to study asymmetrical arrays with different quality factors, we will need to modify these equations to incorporate different photon lifetimes and different threshold carrier densities between two lasers.

A.3 References

[1] W. W. Chow, S. W. Koch, and M. Sargent III, *Semiconductor-Laser Physics*. Springer-Verlag Berlin Heidelberg, 1994.

[2] S. L. Chuang, *Physics of Photonic Devices*, 2nd ed. (Wiley series in pure and applied optics). Hoboken, N.J.: John Wiley & Sons, 2009.

[3] M. Sargent III, M. O. Scully, and W. E. Lamb, *Laser Physics*, Reading, Mass.,: Addison-Wesley Pub. Co., Advanced Book Program, 1974

[4] M. J. Adams, N. Li, B. R. Cemlyn, H. Susanto, and I. D. Henning, "Effects of detuning, gain-guiding, and index antiguiding on the dynamics of two laterally coupled semiconductor lasers," *Physical Review A*, vol. 95, no. 5, p. 053869, 2017.

[5] K. A. Atlasov, K. F. Karlsson, A. Rudra, B. Dwir, and E. Kapon, "Wavelength and loss splitting in directly coupled photonic-crystal defect microcavities," *Optics Express*, vol. 16, no. 20, pp. 16255-16264, 2008.

APPENDIX B: EVALUATION OF THE ANTIGUIDING COUPLING COEFFICIENT VIA OVERLAP INTEGRAL

The overlap integral formulation can be used to calculate the coupling coefficient [1-4]. We show below that in our passive antiguided structure, it offers insight but is inaccurate.

When the refractive index profile is passive, conventional CMT says that the coupling coefficient can be expressed as

$$\kappa_{BA} = \frac{k_0^2}{2\beta_B} \frac{\int_{-\infty}^{+\infty} E_A(x) \Delta\epsilon_B(x) E_B(x) dx}{\int_{-\infty}^{+\infty} E_B(x)^2 dx} \tag{B.1}$$

where k_0 is the vacuum wavenumber, β_B the propagation constant in waveguide B, $\Delta\epsilon_B(x)$ the index profile of waveguide B, and $E_{A,B}(x)$ are the amplitude profiles of the individual waveguide modes in waveguide A and B, respectively. When the fields and the index profiles are real-valued, we see Equation (B.1) is consistent with Equation (A.30b) in Appendix A. We have chosen $E_{A,B}(x)$ to be real since the structure we study is completely passive. [When there exists a complex-valued index profile, meaning there is nonuniform gain/loss present, Equation (A.30b) should be used instead of Equation (B.1).] To evaluate this overlap integral, we should define $\Delta\epsilon_{A,B}(x)$ first, so that we can solve for $E_{A,B}(x)$. Our definition of $\Delta\epsilon_A(x)$ is shown by the blue outlines in Figure B.1(a), by assuming the absence of the waveguide B. Similarly, $\Delta\epsilon_B(x)$ is defined in the same fashion (not shown). The separation between two waveguides is chosen to support positive coupling in index profile (i) and negative coupling in index profile (ii). The mode profiles $E_{A,B}(x)$ are calculated by a 1D numerical FDFD mode solver, shown by red and black lines in Figure B.1(a). Comparing the mode profiles in Figure B.1(a), it can be observed that in (i) $E_A(x)$ and $E_B(x)$ have the same sign at the center of waveguide B, while in (ii) they have opposite signs. Because of this, the overlap integral (and hence the coupling coefficient) is positive in (i) and negative in (ii). In other words, the phase delay caused by lateral leaky-wave propagation, $k_t \cdot d$, is 0 and π respectively for the in-phase and out-of-phase coupling. This offers insight into the physics of coupling sign control from the leaky-wave propagation point of view.

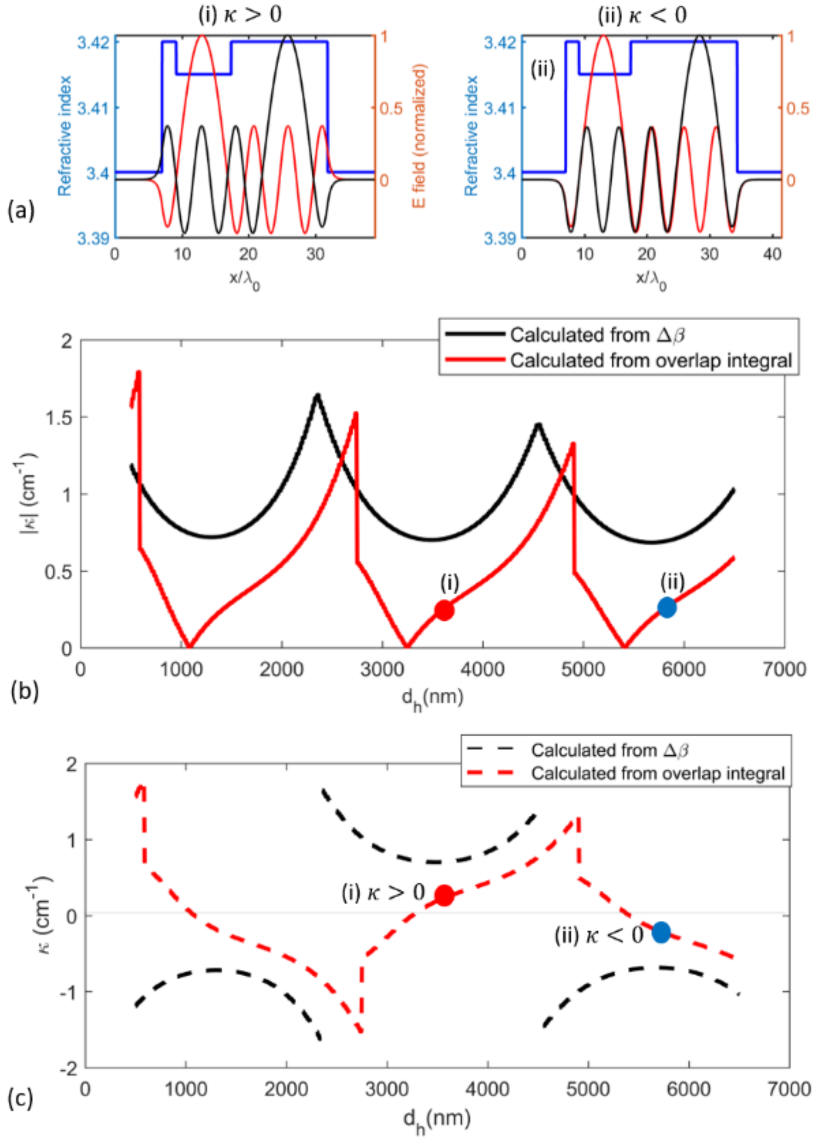

Figure B.1: (a) Individual waveguide index profile $\Delta\epsilon_A(x)$ (blue) and the two individual waveguide mode profiles $E_{A,B}(x)$ (red and black), for inter-element separation equal to (i) 3500 nm or (ii) 5800 nm. (b) Absolute value and (c) signed value of the coupling coefficients calculated from the overlap integral (red) compared with the values extracted from exact solution of normal modes (black). The two points correspond to the two cases shown in (a).

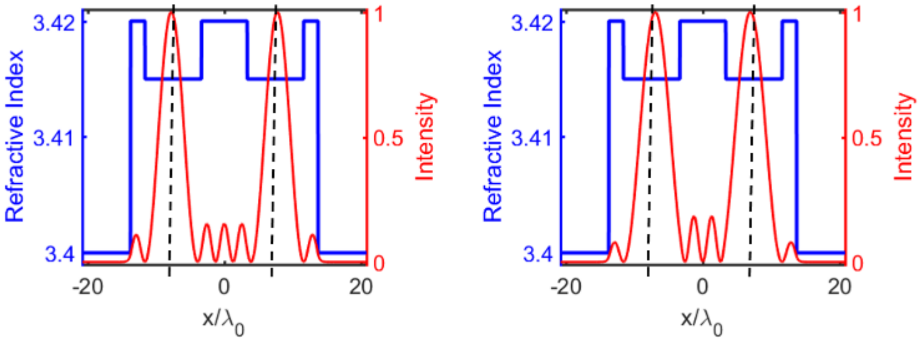

Figure B.2: Intensity profile of the two coupled modes in the antiguided coupled waveguide, showing that the in-phase and out-of-phase normal modes have their intensity peaks at slightly different locations in the core. Center of the cores are labeled by the black dashed lines.

However, the value of κ_{BA} calculated by the overlap integral [red curves in Figures B.1 (b) and B.1(c)] shows a noticeable amount of error compared with the value extracted from exact solutions. More importantly, it shows qualitatively wrong behavior by having zero crossings. There can be no zero crossings for κ_{BA}, because mathematically there are no degenerate states in the one-dimensional passive (Hermitian) system. This error arises from the definition of $E_{A,B}(x)$. Examination of the intensity distribution of the coupled modes from the exact solution of composite waveguide structure, shown in Figure B.2, shows that the intensity peaks for the in-phase and out-of-phase mode are slightly shifted in opposite directions from the middle of the waveguide cores. Thus, a better choice of basis modes is required if the overlap integral formula is to be used for the antiguided coupling coefficient calculation.

B.1 References

[1] A. Yariv, "Coupled-mode theory for guided-wave optics," *IEEE Journal of Quantum Electronics*, vol. Qe 9, no. 9, pp. 919-933, 1973.

[2] H. A. Haus, *Waves and Fields in Optoelectronics* (Prentice-Hall series in solid state physical electronics). Englewood Cliffs, NJ: Prentice-Hall, 1984

[3] X. R. Wang, C. D. Xiong, and J. Y. Luo, "Coupling coefficients evaluation of a directional coupler using gain guided and index antiguided fibers," *Optics Communications*, vol. 282, no. 3, pp. 382-386, 2009.

[4] M. J. Adams, N. Li, B. R. Cemlyn, H. Susanto, and I. D. Henning, "Effects of detuning, gain-guiding, and index antiguiding on the dynamics of two laterally coupled semiconductor lasers," *Physical Review A*, vol. 95, no. 5, p. 053869, 2017.

APPENDIX C: THE OTHER TWO SETS OF SOLUTIONS TO THE STEADY-STATE COUPLED RATE EQUATIONS

When solving the steady-state coupled rate equations (SSCREs), in addition to the two sets of solutions discussed in the main text, there are another two sets of solutions that to our knowledge were first recognized in Ref. [1]. These interesting modes remain asymmetrical even when the system is completely symmetrical (i.e. $Q_A = Q_B = Q, \Delta\Omega = 0$). However, when the coupling is weak (i.e. $\tau_p \kappa \ll 1$), those modes have very asymmetrical intensity distribution unless $Q_{A,B} \approx 1$ (i.e. pump levels very close to threshold). Since we need to consider above-threshold situations, they are not realistic modes and are ignored in our analysis. These two modes can be numerically identified and plotted in Figures C.1 and C.2 as the green curves. At equal pumping and zero cavity detuning (i.e. $Q_A = Q_B = Q, \Delta\Omega = 0$), one of the modes is approximately

$$\frac{Y_B}{Y_A} \cong \frac{Q-1}{2\tau_p \kappa}\sqrt{\alpha_H^2 + 1} \gg 1$$

$$M_A \cong Q$$

$$M_B \cong 1$$

$$\phi \cong \tan^{-1}(1/\alpha_H)$$

and the other mode is

$$\frac{Y_A}{Y_B} \cong \frac{Q-1}{2\tau_p \kappa}\sqrt{\alpha_H^2 + 1} \gg 1$$

$$M_A \cong 1$$

$$M_B \cong Q$$

$$\phi \cong -\tan^{-1}(1/\alpha_H)$$

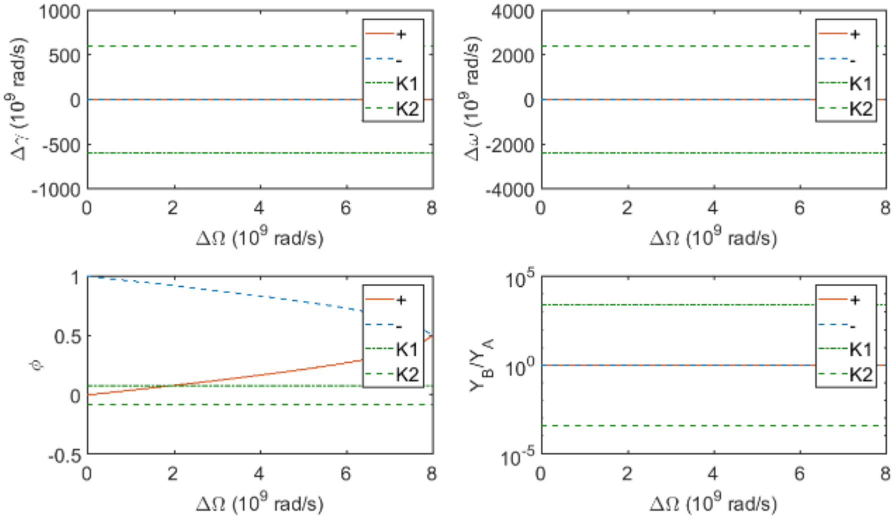

Figure C.1: Numerical solutions of the SSCREs for Array 1 (very weak coupling, $\kappa = 0.002/\tau_p$) that include the two asymmetrical modes (K1 and K2): (a) Induced gain contrast; (b) total frequency detuning; (c) relative phase; (d) field magnitude ratio between two cavities are plotted versus the cavity detuning $\Delta\Omega$. The pump parameters are set to $Q_A = Q_B = 3.2$, corresponding to $I_A = I_B = 2.375\ I_{th}$.

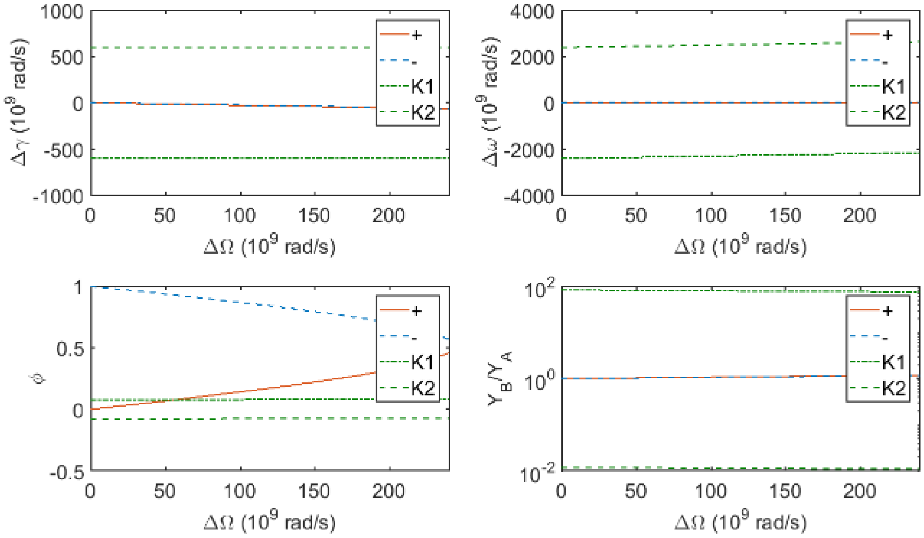

Figure C.2: Numerical solutions of the SSCREs for Array 2 (moderately weak coupling, $\kappa = 0.06/\tau_p$) that include the two asymmetrical modes (K1 and K2): (a) Induced gain contrast; (b) total frequency detuning; (c) relative phase; (d) field magnitude ratio between two cavities are plotted versus the cavity detuning $\Delta\Omega$. The pump parameters are set to $Q_A = Q_B = 3.2$, corresponding to $I_A = I_B = 2.375\ I_{th}$.

The extremely asymmetrical intensity distribution and the large $\Delta\gamma$ are results of a cavity being almost completely empty of photons while the carrier density in that cavity accumulates to unrealistically high above the threshold carrier density. This is likely unrealistic because the factors ignored in the coupled rate equations (CREs), for example the spontaneous emission and multi-mode lasing in an individual cavity, would start being significant and the simplified CREs that we use would not be valid anymore.

C.1 References

[1] Y. Kominis, V. Kovanis, and T. Bountis, "Controllable asymmetric phase-locked states of the fundamental active photonic dimer," *Physical Review A*, vol. 96, no. 4, p. 043836, 2017.

APPENDIX D: OUT-OF-PHASE SOLUTION OF THE COUPLED RATE EQUATIONS AND ITS CONVERGENCE TO THE IN-PHASE SOLUTION

We discuss the out-of-phase mode and the convergence of the tilted in-phase and tilted out-of-phase optical modes of coupled laser arrays. Similar to Figures 3.4 and 3.5 that show the in-phase mode, we plot the out-of-phase mode in Figures D.1 and D.2, for Array 1 and Array 2 respectively.

One further observation can be made by calculating the difference between the tilted out-of-phase mode and the tilted in-phase mode, namely $|\Delta\gamma_- - \Delta\gamma_+|$, $|\Delta\omega_- - \Delta\omega_+|$, $(\phi_- - \phi_+)$, and $\left|\left(\frac{\mathrm{Y_B}}{\mathrm{Y_A}}\right)_- - \left(\frac{\mathrm{Y_B}}{\mathrm{Y_A}}\right)_+\right|$, as shown in Figures D.3 and D.4. It can be observed that the two sets of solutions converge to the same value along the lines of broken PT symmetry, located at the boundary of the locking region. [For $(\phi_- - \phi_+)$, converging to 2π is equivalent to converging to 0.] Along the line of unbroken PT symmetry (see Figure 3.5), $\Delta\gamma, \Delta\omega,$ and Y_B/Y_A from the two sets of solutions converge to the same value, but not ϕ. From the property of the unbroken PT symmetric modes, we know that $\phi_+ + \phi_- = \pi$. In other words, $\Delta\gamma, \Delta\omega,$ and Y_B/Y_A of the two sets of solutions converge when the array has either broken or unbroken PT symmetry, while ϕ_+ and ϕ_- converge only when the array has broken PT symmetry. The underlying mathematical structure of the solutions, which may be responsible for the converging behavior along the broken PT symmetry lines, is interesting for future study. It can be observed from the numerical solutions that $|\Delta\omega_+ - \Delta\omega_-|$ and $|\Delta\gamma_+ - \Delta\gamma_-|$ are linearly related and the line depicting broken PT symmetry might be a branch cut if we take linear combinations of $\Delta\omega$ and $\Delta\gamma$ to be the real and imaginary part of a complex variable.

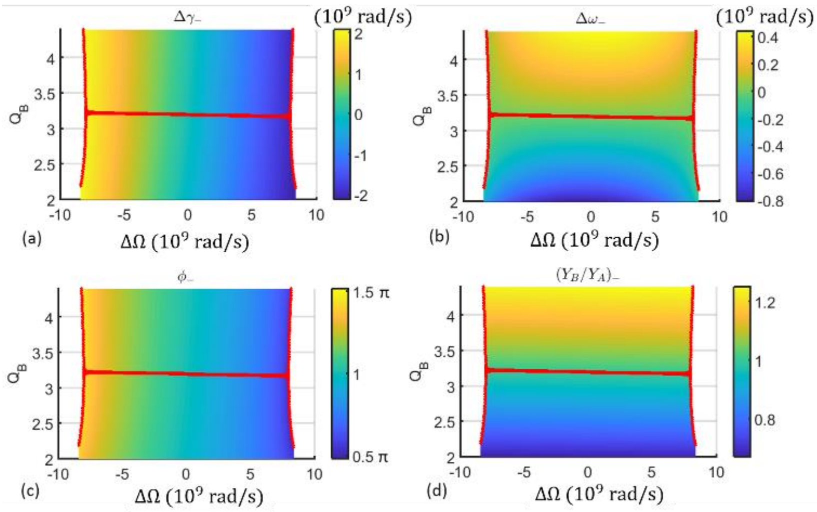

Figure D.1: The tilted-out-of-phase solution for Array 1 ($\kappa = 0.002/\tau_p$): (a) Induced gain contrast; (b) total frequency detuning; (c) relative phase; and (d) field magnitude ratio versus the cavity detuning and pump parameter Q_B, while Q_A is fixed at 3.2. The pump parameters correspond to having I_A fixed at $2.375\ I_{th}$, while I_B varies from $1.625\ I_{th}$ to $3.125\ I_{th}$. Red lines show where the array is PT symmetric.

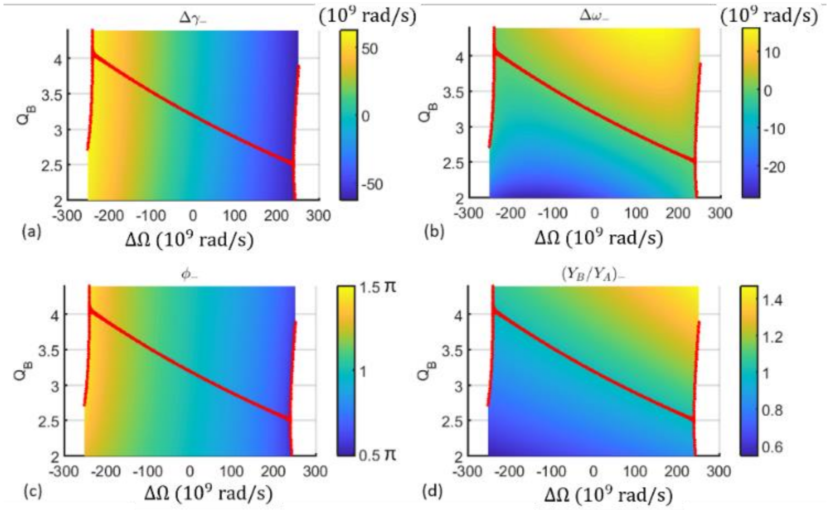

Figure D.2: The tilted-out-of-phase solution for Array 2 ($\kappa = 0.06/\tau_p$): (a) Induced gain contrast; (b) total frequency detuning; (c) relative phase; and (d) field magnitude ratio versus the cavity detuning and pump parameter Q_B. Again, Q_A is fixed at 3.2, while Q_B varies from 2 to 4.4. Red lines show where the array is PT symmetric.

Although we find the two solutions to SSCREs will collapse anywhere along the lines of broken PT symmetry, this collapsing is different from the eigenmode collapse occurring at the exceptional points. At the exceptional points, the coupled mode equations predict two collapsed

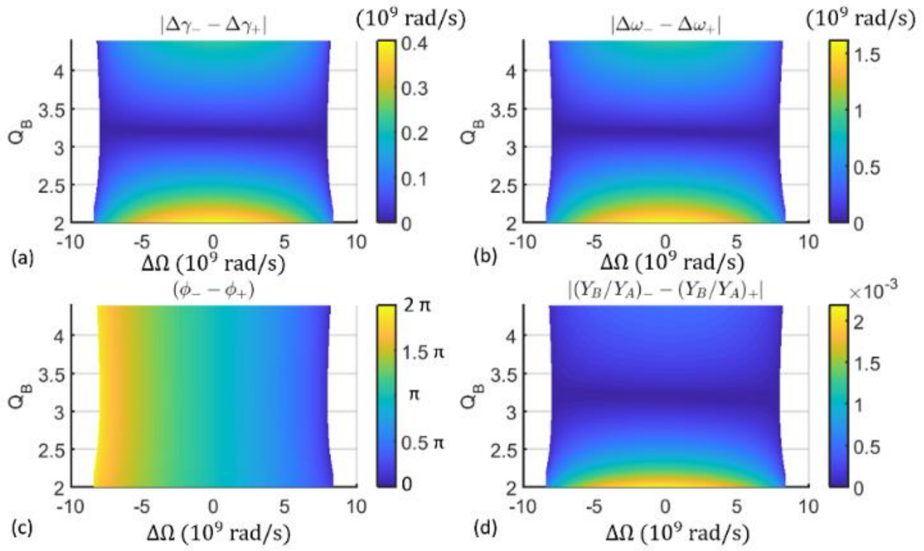

Figure D.3: Plot of the difference between the tilted-out-of-phase and tilted-in-phase solutions (Array 1, very weak coupling): (a) Absolute difference between the gain contrast $|\Delta\gamma_- - \Delta\gamma_+|$; (b) absolute difference between the total frequency detuning $|\Delta\omega_- - \Delta\omega_+|$; (c) difference between the relative phase $(\phi_- - \phi_+)$; (d) absolute difference between the field magnitude ratio $\left|\left(\frac{\mathrm{Y_B}}{\mathrm{Y_A}}\right)_- - \left(\frac{\mathrm{Y_B}}{\mathrm{Y_A}}\right)_+\right|$.

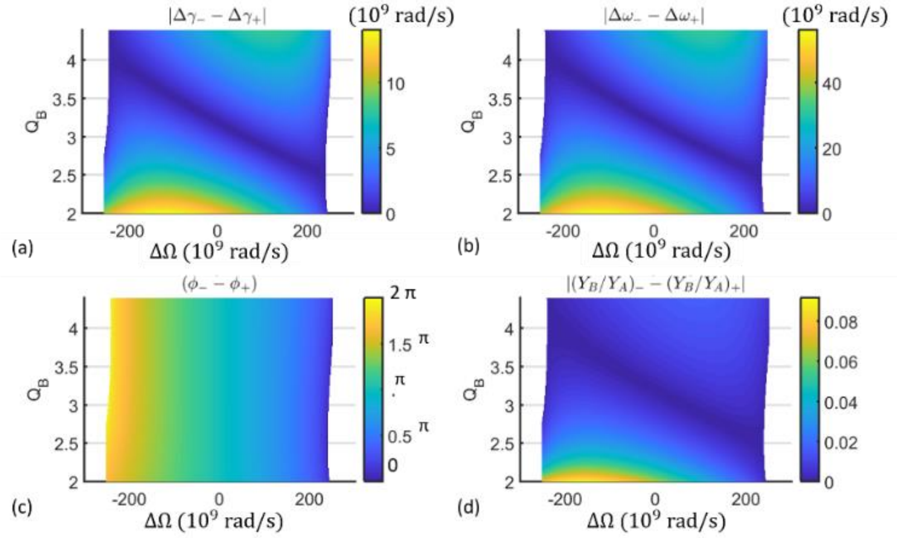

Figure D.4: Plot of the difference between the tilted-out-of-phase and tilted-in-phase solutions (Array 2, moderate coup): (a) Absolute difference between the gain contrast $|\Delta\gamma_- - \Delta\gamma_+|$; (b) absolute difference between the total frequency detuning $|\Delta\omega_- - \Delta\omega_+|$; (c) difference between the relative phase $(\phi_- - \phi_+)$; (d) absolute difference between the field magnitude ratio $\left|\left(\frac{\mathrm{Y_B}}{\mathrm{Y_A}}\right)_- - \left(\frac{\mathrm{Y_B}}{\mathrm{Y_A}}\right)_+\right|$.

eigenmodes. Anywhere else along the lines of broken PT symmetry, the coupled mode equations predict two linearly independent eigenmodes, but only one of them satisfies the carrier rate equations.

APPENDIX E: COHERENT ARRAY PROCESS FOLLOWER

Sample Name:

Include notes on backside of pages (e.g. for different samples note difference in recipe, measured thickness, etc.)

Process Order: Mesa+PhC (DoC), Stacked Implant Aperture (DoC), Top Contact (DoC), [optional: Bottom Contact (CoD)], Planarization (DoC), Fan Metal (CoD)

0. ______Cleave and Clean

☐ Cleave, take ID photo, degrease (Acetone, IPA, DI, IPA) and N_2 dry.
No identification scratch/label on backside, reduces durability

1. ______SiO_2 Deposition:

☐ Degrease
☐ ~ 4000 Å – Time: ______ min, Rate: ______ Å/min
(750 seconds at low dep rate on Trion for 4000 Å)
☐ Thickness: ______Å (ellipsometer)

2. ______Mesa + PhC photolithography

☐ Degrease
☐ Dehydration bake (110 ^{o}C for 5 min)
(note for ALL bakes use a transfer/carrier wafer)
☐ HMDS spin (30 s 4000 rpm)

☐ AZ5214 spread (3 s 500 rpm)
☐ AZ5214 spin (30 s 4000 rpm)
☐ Edge bead removal
☐ Bake (110 ^{o}C for 45 s)
☐ Mask: **Coherent Array - Implant / Mesa & PhC - BJT** (5/13/16)
☐ Expose: 30 s (aligner A at 9 mW/cm^2)
☐ Power: ______W; Time: ______s
☐ Develop in AZ327 MIF (~ 50-55 s): _______s

3. ______SiO_2 Etch:

☐ O_2 plasma descum (250W for 3min)
☐ CF_4 RIE for > 4000 Å (~ 22 min)
☐ Time: _______min
☐ Make sure field conducts before proceeding! If not, more etching is required before PR removal.
☐ Remove PR mask (Acetone, IPA, DI, IPA)
☐ Alpha-step: _______µm

4. ______Stacked implant aperture photolithography:

(Double spin resist!)
(Do not leave 9260 double-spinned undeveloped overnight)
(Pay special care to the PR sidewall during development. Stop development before the field is totally clear to preserve straight sidewall. Then use O2 plasma to clear up the field.)

- ☐ Degrease
- ☐ Dehydration bake (110 °C for 5 min)
- ☐ NO HMDS spin, double spin better without it
- ☐ Apply photoresist AZ9260 for spin #1
- ☐ AZ9260 spread (5 s 500 rpm)
- ☐ AZ9260 spin (30 s 4000 rpm)
- ☐ Soft-bake (110 °C for 3 min)
- ☐ Edge bead removal (3 min on C, 1min30s AZ421K 1:3 dilution, and swab)
- ☐ Apply photoresist AZ9260 again, spin #2
- ☐ AZ9260 spread (5 s 500 rpm)
- ☐ AZ9260 spin (30 s 4000 rpm)
- ☐ Soft-bake (110 °C for 3 min)
- ☐ Edge bead removal (3 min on C, 4 min AZ421K 1:3, and swab)
- ☐ Mask: **Coherent Array - Implant / Mesa & PhC - BJT** (5/13/16)
- ☐ Expose: 4 min (aligner A at 9 mW/cm^2)
- ☐ Power: ______W; Time: ______s
- ☐ Develop in AZ421K 1:2 (~ 3 min 50 s): _______s
- ☐ O_2 plasma descum (500W for 5 min)
- ☐ Goal (~9-11 µm) Alpha-step: _______µm
- ☐ (Optional) UV harden on Aligner A for 10 minutes (no bake after UV)

5. ______Send for implant: Kroko Stacked H+ implant, 7° tilt

protons 330 keV	5x10^{14} /cm^{2}
protons 300 keV	5x10^{14} /cm^{2}
protons 260 keV	5x10^{14} /cm^{2}
protons 210 keV	5x10^{14} /cm^{2}
protons 160 keV	5x10^{14} /cm^{2}
protons 100 keV	5x10^{14} /cm^{2}
oxygen 300 keV	5x10^{13} /cm^{2}
oxygen 150 keV	5x10^{13} /cm^{2}
oxygen 50 keV	5x10^{13} /cm^{2}

6. ______Remove implant PR:
- ☐ O_2 plasma descum (1000W for 8 min)
- ☐ Boiling acetone soak (40 °C)

☐ Squirt gun
☐ Swab unimportant area (edges)
☐ Repeat steps above until sample is clean (make take 3 repetitions)

7. ______ICP Etch:

☐ Clean ICP-RIE using O_2
☐ Use ICP-RIE $SiCl_4$/Ar recipe and reflectometry setup
☐ Etch according to required etch depth
☐ (Optional surface treatment: 1:1 HCl:DI 1min, 10 min DI decanting, Hydrogen plasma)
☐ Etch according to required etch depth
May require calibration etch of blank piece
Stop at GaAs/high signal layer 4 DBR pair past active
☐ Time: _______min (rate: ________Å/min)
☐ Alpha-step: _______µm

(Optional Step– For semi-insulating substrates use a bottom contact, otherwise do broad-area backside contact and no photolithography)

8. ______Bottom contact photolithography:

☐ Degrease
☐ Dehydration bake (110 °C for 5 min)
☐ HMDS spin (30 s 4000 rpm)

☐ AZ4330 spread (3 s 500 rpm)

☐ AZ4330 spin (30 s 5000 rpm)

☐ Bake (95 ^{o}C for 90 sec)

☐ Edge bead removal – 1.5 min on Aligner C

☐ Ensure edges are clear/clean

☐ Mask: (Not ordered yet)
☐ Expose: 60 sec (aligner A at 9 mW/cm^2)

☐ Power: ______W; Time: ______s

☐ Develop in AZ 400K (~ 60 s): _____s

9. ______Bottom contact (*n*):

☐ O_2 plasma descum (300W for 2 min)
☐ Dip in 1:10 NH_4OH:DI for 20 s
☐ DI rinse (10 min)
☐ Target: 400 Å Au-Ge / 200 Å Ni / 1500 Å Au
Actual: ____Å Au-Ge / ____Å Ni / _____Å Au

10. ______Metal Liftoff:

☐ Boiling acetone (40 °C) / Squirt gun

11. ______SiO_2 mask removal:

☐ CF_4 RIE for < 4000 Å (~ 15 min) (see color)
☐ Check if the mesas conduct
☐ Continue etching 2 or 3 min increments until mesas conduct
☐ Time: _______min

12. ______Top contact (LOR process. Never use acetone after LOR is applied. Use Remover PG to remove LOR.)

☐ Degrease
☐ Dehydration bake (110 °C for 5 min)
☐ LOR30B spread (4 s 400 rpm)
☐ LOR30B spin (60 s 4000 rpm)
☐ Edge beam removal with Remover PG
☐ Bake (170 °C for 5 min), clean edges
☐ AZ5214 spread (3 s 500 rpm)
☐ AZ5214 spin (30 s 4000 rpm)
☐ Bake (110 °C for 45 s)
☐ Edge bead removal (1min on Aligner C, 1min 327 MIF, optional: swab edges with 327 MIF)
☐ Mask: **Coherent Array - Planarization / Top Metal - BJT** (5/13/16)
☐ Expose: 25 s (aligner A at 9 mW/cm^2)
☐ Power: ______W; Time: ______s
☐ Reversal bake (110 °C for 45 s)
☐ Flood exposure 45 s (aligner A at 9 mW/cm^2)
☐ Develop in AZ 327 MIF (~ 40 s):____s
☐ Bake (125 °C for 1 min)
☐ Develop in AZ 400K 1:4 (~1min):____min
☐ Check pattern: small LOR undercut desired

13. ______Top contact (*p*):

☐ O_2 plasma descum (300W for 2 min)
☐ DI rinse (10 min)
☐ Dip in 1:10 NH_4OH:DI for 20 s
☐ Target: 150 Å Ti / 1600 Å Au
Actual: ______Å Ti / ______Å Au

14. ______Metal Liftoff:

☐ Remover PG soak #1 ~ 30min
☐ Remover PG soak #2 (in another beaker) ~ 5min
☐ IPA soak ~ 1 min
☐ IPA rinse, DI rinse, IPA rinse

15. ______Contact annealing

☐ 410 ^{o}C for > 1 min using oxidation furnace

16. ______Test

☐ Check for lasing and electrical isolation

17. ______Planarization (PI):
(polyimide)

☐ Degrease
☐ Dehydration bake (125 °C for 3 min)
☐ NMP ramp (250 rpm/sec)
☐ NMP spin (60 s 5000 rpm)
☐ HD 4104 ramp (300 rpm/sec)
☐ HD 4104 spin (60 s 2600 rpm)
☐ Edge bead removal with razor blade
☐ Backside clean (PA.401D and PA.400R swab)
!!! Wait for PA.400R on backside to dry before bake!
☐ Bake (90 ^{o}C for 100 sec + 100 ^{o}C for 100 sec more)
☐ Alpha-step edge bead: ________µm
☐ Mask: **Coherent Array - Planarization / Top Metal BJT** (5/13/16)
☐ Expose: 13 sec (Aligner C, I-line 365 nm at 9 W/cm^2)
(Dose of 117 mJ/cm^2)
☐ Wait > 5 min
☐ Develop with PA.401D: _______s (50 s)
☐ Rinse with PA.400R: _______s (30 s) (No DI)
☐ Alpha-step: _____ µm (double required height)
☐ PI cure on Recipe 3 (PI should shrink down by ~ 50%)
(ramp up 10 ^{o}C /min – 150 ^{o}C soak 20 min)
(ramp up 4 ^{o}C /min – 250 ^{o}C soak 30 min)
(ramp up 4 ^{o}C /min – 300 ^{o}C soak 3 hr)
(ramp down 10 ^{o}C /min – 25 ^{o}C soak 3 hr)
☐ Alpha-step: Field _____µm, Mesa crown _____µm,
Via crown _____µm
☐ CF$_4$ RIE: RF 20%, 35mT, 60% O$_2$, 10% CF$_4$
(etch rate of 0.16-0.2 µm/min)
☐ Time: _____min, Rate: _____ µm/min
(etch until openings are clear)
☐ Alpha-step: _____µm

18. ______Fan metal
photolithography:

☐ Degrease
☐ Dehydration bake (125 °C for 3 min)
☐ HMDS spin (30 s 4000 rpm)

☐ AZ9260 spread (3 s 500 rpm)

☐ AZ9260 spin (30 s 5000 rpm)

☐ Bake (110 ^{o}C for 4 min 20 s)

☐ Edge bead removal – 2 min on C, 1 min AZ400K 1:2

☐ Mask: **Coherent Array – Fan Metal – BJT** (08/15/16)
☐ Expose: 3 min (aligner A at 9 mW/cm^2)

☐ Power: ______W; Time: ______s

☐ Develop in AZ 400K 1:2 (~ 60 s): _____s

19. ______Fan metal (*p*):

☐ O_2 plasma descum (300W for 2 min)
☐ DI rinse (10 min)
☐ Target: 150 Å Ti / 10000 Å Au
Actual: ______Å Ti / ______Å Au

20. ______Metal Liftoff:

☐ Boiling acetone (40 ^{o}C) / Squirt gun

21. ______Test